# A Measurement of Single Charged Pion Production in MicroBooNE

**Alesha Devitt**

This thesis is submitted for the degree of *Doctor of Philosophy*

Lancaster University
Physics Department
November, 2022

# Abstract

MicroBooNE is a 170 ton liquid argon time projection chamber (LArTPC) located at the Fermi National Accelerator Laboratory (Fermilab). It operated in the Booster Neutrino Beam (BNB) at a mean neutrino energy of 0.8 GeV, taking data from 2015 to 2021. It is the first large LArTPC to gather high statistics neutrino data, and as such it serves an important role in the further development of this technology, which is planned for use in a number of future experiments. Additionally, MicroBooNE has two main physics goals: resolving the cause of the low energy excess observed by MiniBooNE [1], and measuring neutrino cross sections on argon.

Neutrino interactions with heavy nuclei like argon are significantly affected by nuclear effects and final state interactions (FSI), which we lack a complete understanding of. Measuring additional cross section data is critically important for providing further insights. Next generation experiments aim to answer many open questions in neutrino physics, and will rely on precision measurements to do so. This thesis serves this objective, presenting the first measurement of single charged pion production (CC1$\pi^+$) in MicroBooNE. A detailed discussion of this process is given, including descriptions of the event selection, estimation of systematic uncertainties, and extraction of the cross section result itself. The total, flux-integrated CC1$\pi^+$ cross section on argon per nucleon is measured to be $0.788 \pm 0.079$ (stat.) $\pm 0.261$ (syst.) $\times 10^{-39}$ cm$^2$.

# Declaration

This thesis is my own and the work presented in it is a result of my own original research, except as noted below. This thesis has not been submitted in substantially the same form at this or any other university for the award of a higher degree.

The work presented in this thesis is made possible by a large number of other researchers, the MicroBooNE Collaboration. Work that is not my own is clearly attributed, including references given where possible.

Chapter 1 provides background information for this work, including an overview of neutrino physics and a history of modern pion production measurements. Chapter 2 describes various aspects of the MicroBooNE experiment, including the detector, the neutrino beamline, and event simulation and reconstruction. Both of these chapters are my summaries of the work of others.

Chapter 3 describes service work that I undertook in 2016. Section 3.1 describes work that I did equally in collaboration with Dr. Adam Lister to provide the first benchmarking of MicroBooNE's simulation and reconstruction algorithms and of its detector performance. Section 3.2 describes my contributions toward MicroBooNE's first CC inclusive selections. They were primarily developed by other MicroBooNE collaborators, but I provided input based on the validation work described in the previous section. Additionally, Dr. Adam Lister and I jointly presented the results on behalf of the MicroBooNE collaboration at the Neutrino 2016 conference. We also jointly wrote a paper with these results that was published as part of the conference proceedings.

Chapter 4 provides a brief overview of MicroBooNE's more recent CC inclusive analysis. This analysis is in no part my own work. It is primarily the work of Dr. Marco Del Tutto, which I summarise due to its use as a pre-selection for my CC1$\pi^+$ selection.

The next several chapters provide the core descriptions of my work. Chapter 5 outlines the CC1$\pi^+$ selection. It is my own work, with the exception of the log-likelihood particle ID algorithm described in Section 5.4.4. I use this algorithm as part of my event selection, but the algorithm itself was developed by Dr. Kirsty Duffy and Dr. Adam Lister. I was not involved it its development, and I describe it only for completeness.

Chapter 6 goes over my work estimating systematic uncertainties. Chapter 7 explains the process of extracting the cross section and presents my final results. Chapter 8 provides my thoughts on areas where this analysis could be improved or built upon in the future. Finally, Chapter 9 gives my summary of this work and concluding thoughts.

# Acknowledgements

First, I would like to thank my advisors, Jarek Nowak and Andy Blake, for providing me with this opportunity, and for their much valued insights and support.

I am grateful to Dom Brailsford and the other postdocs of Lancaster for teaching me a plethora of important practical skills.

Being a part of the MicroBooNE collaboration has been wonderful, and I'm sure I could never hope to name every person who helped me along the way. In particular I would like to thank Sam Zeller, Bonnie Fleming, Matt Toups, Anne Schukraft, and Andy Furmanski for their leadership and constant support. I also owe an enormous debt to Marco Del Tutto, Adam Lister, and especially Kirsty Duffy, all of whom worked closely with me and without whom I undoubtedly would not have been able to accomplish this.

Kate Davison, Kate Nordin, Beau, Vona Rustay, Marie Chelberg, and Grandma Joyce are but a few of the many friends and family who have helped more than I could ever say. I love you all very much and I appreciate all that you've done to support me. This degree took somewhat longer than initially anticipated, and at times I didn't think I was going to finish it. I assuredly would not have been able to if it hadn't been for your help and encouragement.

Lastly, a thanks to all of the furry companions who have provided a much needed source of stress relief and unconditional joy: Senshi, Squash, Shiro, Mio, Roxy, and Lily.

# Glossary

**ASIC** Application-Specific Integrated Circuit

**BDT** Boosted Decision Tree

**BNB** Booster Neutrino Beam

**CC** Charged Current

**COH** Coherent Scattering

**CORSIKA** Cosmic Ray Simulations for Kascade, the cosmic ray generator used in this analysis

**CP** Charge Conjugate Parity, a type of symmetry in particle interactions

**CR** Cosmic Ray

**dE/dx** Change in energy over distance

**DIC** Dynamic Induced Charge

**DIS** Deep Inelastic Scattering

**dQ/dx** Change in charge over distance

**Fermilab** Fermi National Accelerator Laboratory

**FSI** Final State Interactions

**FV** Fiducial Volume

**LArTPC** Liquid Argon Time Projection Chamber

**Linac** Linear Accelerator

**MC** Monte-Carlo

**MCS** Multiple Coulomb Scattering

**MEC** Meson Exchange Current

**MIP** Minimum Ionising Particle

**NC** Neutral Current

**NuMI** Neutrinos at the Main Injector

**Pandora** A multi-algorithm pattern recognition framework used for particle reconstruction

**PE** Photo Electron

**PFO** Particle Flow Object, a collection of PFPs in Pandora

**PFP** Particle Flow Particle, a Pandora object corresponding to one reconstructed particle

**PMNS** The Pontecorvo-Maki-Nakagawa-Sakata matrix, which describes neutrino oscillations

**PMT** Photomultiplier Tube

**QE** Quasi-Elastic

**RES** Resonant

**residual range** Distance from a point on a track to the end of the track

**RMS** Root mean square

**RPA** Random Phase Approximation

**SBN** Short Baseline Neutrino Program

**SCE** Space Charge Effect

**SM** Standard Model of particle physics

**TMVA** Toolkit for Multivariate Data Analysis with ROOT

**tune** A given set of models used for event simulation with GENIE

# Contents

**Abstract** i

**Declaration** ii

**Acknowledgements** iv

**Glossary** v

**Contents** vii

**List of Tables** x

**List of Figures** xii

**1 Introduction** 1

1.1 Neutrino Interactions . . . 2

1.1.1 Nuclear Effects and Final State Interactions . . . 4

1.1.2 Neutrino Oscillations . . . 5

1.2 Pion Production Measurements . . . 6

**2 The MicroBooNE Experiment** 11

2.1 The MicroBooNE Detector . . . 11

2.2 The Booster Neutrino Beam . . . 13

2.3 Event Simulation . . . 15

2.3.1 Neutrino Flux Simulation . . . 15

2.3.2 Cosmic Ray Simulation . . . 16

2.3.3 Neutrino Interaction Simulation . . . 16

2.3.4 Detector Simulation . . . 17

2.4 Event Reconstruction . . . 18

2.4.1 Hit Reconstruction . . . 18

2.4.2 Pandora Pattern Recognition . . . 19

2.4.3 Optical Reconstruction . . . 21

**3 Simulation Benchmarking and First CC Inclusive Selections 22**
3.1 Simulation Benchmarking . . . 22
3.2 CC Inclusive Analysis Contributions . . . 24

**4 CC Inclusive Selection 29**
4.1 Flash Matching . . . 29
4.2 Muon Candidate Selection . . . 30
4.3 Track Quality . . . 31
4.4 Fiducial Volume . . . 33
4.5 Selection Performance . . . 34

**5 CC1$\pi^+$ Selection 37**
5.1 Signal Definition and Backgrounds . . . 37
5.2 Track Refitting . . . 39
5.3 Quality Cuts . . . 40
5.3.1 Vertex-track start distance . . . 40
5.3.2 Polar Angle . . . 42
5.4 Boosted Decision Tree . . . 45
5.4.1 Boosting Algorithms . . . 48
5.4.2 Input Sample and Weighting . . . 50
5.4.3 Truncated Mean dE/dx . . . 51
5.4.4 Log-Likelihood Particle ID . . . 51
5.4.5 Number of collection plane hits . . . 53
5.4.6 BDT Output Score . . . 55
5.5 Opening Angle . . . 56
5.6 Containment . . . 61
5.7 Muon-Pion Separation . . . 62
5.8 Results . . . 64

**6 Systematic Uncertainties 68**
6.1 Cross Section Uncertainties . . . 69
6.1.1 Interaction Uncertainties . . . 69
6.1.2 Interaction Uncertainty Unisims . . . 71
6.1.3 QE and MEC Cross Section Uncertainties . . . 71
6.1.4 Reinteraction Uncertainties . . . 73
6.2 Beam Flux Uncertainties . . . 76
6.3 Detector Uncertainties . . . 78
6.4 POT Counting Uncertainty . . . 81
6.5 Simulated Dirt Uncertainty . . . 81
6.6 Simulated Cosmic Uncertainty . . . 81

6.7 Number of Target Nucleons Uncertainty . . . . . 82
6.8 Summary . . . . . 82

**7 Cross Section Analysis** **84**
7.1 Dynamic Induced Charge . . . . . 84
7.2 Results . . . . . 85

**8 Future Work and Improvements** **90**
8.1 Dynamic Induced Charge Simulation . . . . . 90
8.2 Opening Angle Selection Cut . . . . . 91
8.3 Cosmic Ray Simulation . . . . . 92
8.4 Muon-Pion Separation . . . . . 93

**9 Conclusions** **94**

**Bibliography** **95**

# List of Tables

1.1 A summary of modern CC1$\pi^{\pm}$ cross section measurements. . . . . 7

2.1 The two GENIE model sets used in this analysis. . . . . 16

5.1 Passing event counts, efficiency, and purity at each stage of the event selection. Event counts are scaled to the Beam-on Data POT of $1.763 \times 10^{20}$. . . . . 65

6.1 List of physics parameters used to assess interaction-related systematic uncertainties in this analysis, including the default value (where available) and prior estimated standard deviation of each. Information reproduced from Ref. [53] for ease of reference. . . . . 70

6.2 The systematic uncertainty on the total cross section due to each interaction parameter, assessed using a unisim approach. Descriptions of the parameters and variations are given in Table 6.1. For technical reasons, some closely related parameters are combined here. . . . . 72

6.3 The systematic uncertainty on the total cross section due to each flux parameter, as well as the combined total systematic uncertainty. . . . 77

6.4 The systematic uncertainty on the total cross section due to each detector effect, as well as the combined total systematic uncertainty due to all of the detector effects. In the case of up/down variations, only the larger of the two is considered when calculating the total uncertainty. . . . . 78

6.5 The relative systematic uncertainty on the total cross section due to each source of uncertainty, as well as the combined total relative systematic uncertainty due to all sources. . . . . 83

7.1 Number of selected events, used to calculate the total cross section. All values are scaled to the on-beam data POT of $1.763 \times 10^{20}$. Uncertainties are statistical only. . . . . 86

7.2 Parameters used to calculate the total cross section. The flux corresponds to $1.763 \times 10^{20}$ POT. Uncertainties are statistical only. The flux and number of targets are taken to have negligible statistical uncertainties. . . . . 86

# List of Figures

1.1 Feynman diagrams of example neutrino interactions: CC (left) and NC (right). . . . . 2
1.2 Total $\nu_\mu$ CC cross sections (per nucleon and for an isoscalar target) divided by neutrino energy, plotted as a function of energy. Data points are from various experimental measurements made from 1977 through 2011. Also shown are predictions from the NUANCE generator [12] for the different interaction mode cross sections: total (solid line), QE (dashed line), RES (dot-dashed line), and DIS (dotted line). Figure from Ref. [13]. . . . . 3
1.3 Feynman diagrams of example neutrino interactions: CCQE (upper left), CCRES (upper right), CCDIS (lower left), and CCCOH (lower right). $X$ refers to a hadronic shower and $A$ refers to an atomic nucleus. 3
1.4 Examples of different possible types of FSI processes. Figure produced by T. Golan, see also Ref. [14]. . . . . 4
1.5 Comparison between MINERvA and MiniBooNE $d\sigma/dT_\pi$ data, and predictions from GENIE for each experiment. Figure from Ref. [29]. . 8

2.1 Schematic of the MicroBooNE LArTPC, housed inside the cryostat. Figure from Ref. [44]. . . . . 11
2.2 A diagram showing the operating principles of the MicroBooNE LArTPC. Figure from Ref. [44]. . . . . 12
2.3 A schematic of the placement of the PMTs in MicroBooNE. Light guide paddles are also shown, but are not involved in this analysis. Figure from Ref. [45]. . . . . 13
2.4 An overview of the Fermilab Accelerator Complex. Figure from Ref. [46]. . . . . 14
2.5 Aerial view of Fermilab with features of the Accelerator Complex marked: the Linac (cyan), Booster (red), path of the accelerated protons from the Booster to the target (pink), BNB (blue), the Main Injector and Recycler (green), and the location of MicroBooNE within the BNB (yellow cross). . . . . 14

2.6 Prediction from simulation of the absolute neutrino flux through MicroBooNE, averaged over the TPC volume, while in neutrino mode. Fluxes are shown for $\nu_\mu$, $\bar{\nu}_\mu$, $\nu_e$, and $\bar{\nu}_e$. Figure from Ref. [50]. . . . . 15
2.7 A comparison of the measured signal on one of the induction planes (the U plane) from an example candidate neutrino data event in MicroBooNE after noise filtering, 1D deconvolution, and 2D deconvolution. It can be seen that the signal is successively more defined. Figure from Ref. [67]. . . . . 19
2.8 A simulated event in MicroBooNE reconstructed with Pandora, showing an example of the particle hierarchy. Figure from Ref. [72]. . . . . 20

3.1 An example plot showing a comparison of track lengths in (area-normalised) cosmic data and MC. The peak at ∼230-250 cm is due to tracks that travel the whole height or width of the detector. This peak is lower in data due to the space charge effect, which was not modelled in this generation of the MC. The difference at the start of the distribution is also due to SCE. Figure from Ref. [73]. . . . . 23
3.2 An example plot showing a comparison of the cosine of the polar angle $\theta$ between tracks and the beam axis, in (area-normalised) cosmic data and MC. Tracks less than 30 cm long have been cut. Data is higher than MC at $\cos(\theta) \approx \pm 1$ (the beam direction) and $\pm 0.85$ (the angle of the two induction planes). In both cases, the disagreement was attributed to noise that was not modelled in the MC. The dip at $\cos(\theta) \approx 0$ is due to difficulty in reconstructing tracks that are parallel to the collection plane. Figure from Ref. [73]. . . . . 23
3.3 An overview of the two CC inclusive selections. Boxes of the same colour indicate similar types of cuts (although the cut values may differ). Figure from Ref. [74]. . . . . 25
3.4 Kinematic distributions for the track range (left) and track $\cos(\theta)$ (right) from Selection I. For events with multiplicity$\geq$2, the longest track is used. Error bars are statistical only. Figures from Ref. [74]. . 27
3.5 Kinematic distributions for the track length (left) and track $\cos(\theta)$ (right) from Selection II. For events with multiplicity$\geq$2, the longest track is used. Error bars are statistical only. Figures from Ref. [74]. . 27
3.6 A collection plane event display of an example CC event selected with Selection I. The horizontal track is from the selected interaction, while the more vertical tracks are identified as cosmics. Figure from Ref. [74]. . . . . 28

4.1 Flash matching for an example MC event. On the left, a reconstructed muon from a neutrino interaction (red) and the reconstructed flash (green) are shown within the TPC (white border). The right plot shows the PE count on each PMT for the reconstructed flash (blue) and the hypothesis flash (green). In this case, they match well. Figures from Ref. [76]. . . . . 30
4.2 Distributions of the differences between the positions of the hypothesis and measured flashes, in the x-direction (left) and z-direction (right). Figures from Ref. [76]. . . . . 30
4.3 Distribution of track length versus truncated mean dQ/dx for simulated muons (red dots) and protons (blue dots). A Support Vector Machine algorithm is used to find a decision boundary, shown with the light red and blue regions. Only those in the red region may be considered as muon candidates. Figure from Ref. [76]. . . . . 31
4.4 Distribution of the standard deviation of the hit residuals for muon candidates, in units of cm. Figure from Ref. [76]. . . . . 32
4.5 Distribution of the fraction of collection plane hits used in the muon candidate track reconstruction. Figure from Ref. [76]. . . . . 33
4.6 (a) The reconstructed momentum for contained muons, as estimated with the MCS method versus the length-based method. (b) The difference between these two methods. Figures from Ref. [76]. . . . . 34
4.7 The fiducial volume used in the analysis. The solid black line represents the boundaries of the TPC, while the dashed lines show the FV. Figure from Ref. [76]. . . . . 34
4.8 CC inclusive selection efficiency as a function of true neutrino energy, for different GENIE interaction types. CC coherent interactions contribute negligibly and are not shown here. Error bars are statistical only. Figure from Ref. [76]. . . . . 36
4.9 The $\nu_\mu$ CC inclusive cross section on argon per nucleon, as a function of the reconstructed muon momentum (left) and $\cos(\theta)$ (right). Figures from Ref. [76]. . . . . 36

5.1 Examples of background (left) and signal (right) events. A red line represents a muon, a blue line represents a proton, a green triangle represents an electromagnetic shower, and a magenta line represents a charged pion. . . . . 38

5.2 The fraction of muons (red circle), pions (green square), and protons (blue triangle) in events passing the CC inclusive pre-selection that are classified by Pandora as tracks, as a function of true kinetic energy. I expect all of these particles to be classified as tracks, and so choose not to use this classification system. . . . . 40
5.3 The distributions of track length (top) and polar angle $\theta$ between the track and the beam axis (bottom) for the longest track in each event that is a direct daughter of the neutrino candidate, after track refitting. 41
5.4 Distribution of the distance between each track's starting point and the reconstructed neutrino vertex. . . . . 42
5.5 The distributions of track length (top) and polar angle $\theta$ between the track and the beam axis (bottom) for the longest track in each event that is a direct daughter of the neutrino candidate, after the cut on vertex-track start distance is applied. . . . . 43
5.6 Efficiency (red), purity (blue), and efficiency times purity (black) of the selection, as a function of the cut value for vertex-track start distance. . . . . 44
5.7 Event display of a simulated event where a single true muon has been reconstructed as two tracks (one shown in red, the other in purple). Both tracks are reconstructed as direct daughters of the reconstructed neutrino vertex (green star). Note that this is a 2D projection of the event in the x-z plane. . . . . 44
5.8 Angles and coordinate system used in MicroBooNE. $\theta$ is the polar angle between a track and the beam axis; $\phi$ is the track's azimuthal angle. Figure from Ref. [74]. . . . . 46
5.9 Distribution of the polar angle $\theta$ between each direct neutrino daughter track and the beam direction. . . . . 46
5.10 The distributions of track length (top) and polar angle $\theta$ (bottom) for the longest track in each event that is a direct daughter of the neutrino candidate, after the cut on $\theta$ is applied. . . . . 47
5.11 Distribution of background rejection versus signal efficiency for each of the five BDT methods tested: adaptive boost, adaptive boost with Fisher discriminant, adaptive boost with decorrelation, gradient boost, and bagging. . . . . 48
5.12 Overtraining checks for each of the BDT algorithms. . . . . 49
5.13 Distributions of each BDT input variable for training sample particles, split into signal (solid blue) and background (hatched red). The variables are truncated mean dE/dx (left), number of collection plane hits (centre), and log-likelihood particle ID (right). . . . . 50

5.14 Distribution of truncated mean dE/dx values. . . . . 51
5.15 Distributions from theory of dE/dx versus residual range for several particle species. Figure from Ref. [82]. . . . . 52
5.16 Probability maps for several particle species. Each bin of residual range is normalized to 100. A non-Bragging MIP refers to a MIP-like particle that exits the detector before stopping, and thus no Bragg peak is seen. Figures from Ref. [82]. . . . . 53
5.17 Distribution of log-likelihood values for each track. Figure produced by me for this analysis, not by the authors of the PID algorithm. . . . 54
5.18 Distribution of the number of reconstructed hits per track. . . . . 54
5.19 Distribution of BDT output scores for each track. . . . . 55
5.20 Efficiency (red), purity (blue), and efficiency times purity (black) of the selection, as a function of the cut value for BDT score. . . . . 56
5.21 The distributions of track length (top) and polar angle $\theta$ (bottom) for the longest MIP candidate in each event, after the cut on BDT score is applied. . . . . 57
5.22 Distribution of opening angles, i.e. the angle between the two MIP candidates, (a) before and (b) after applying a cut at 2.6 radians. . . 58
5.23 Distribution of angles between simulated MIP candidates that are (a) truly broken and (b) truly not broken. Truly broken tracks, for which the two MIP candidates correspond to the same true particles, are strongly peaked toward $\pi$ radians (back-to-back). Conversely, truly not broken tracks, for which the two MIP candidates correspond to different true particles, are distributed more broadly across the range of angles and peak at a lower angle. . . . . 59
5.24 The distributions of track length (top) and polar angle $\theta$ (bottom) for the longest MIP candidate in each event, after the cut on opening angle is applied. . . . . 60
5.25 $\nu_\mu$ CC1$\pi^\pm$ differential cross section as a function of opening angle. ArgoNeuT measurement is compared with predictions from several generators. Figure from Ref. [34]. . . . . 61
5.26 Distribution of whether at least one MIP candidate is contained in each event. . . . . 62
5.27 The distributions of track length (top) and polar angle $\theta$ (bottom) for the longest MIP candidate in each event, after the containment cut is applied. . . . . 63

5.28 2D distribution of the proportion of selected true signal events with a given true particle species of the muon candidate (x-axis) and of the pion candidate (y-axis). For example, in 86.2% of these events, the muon candidate was truly a muon and the pion candidate was truly a pion. . . . . 64
5.29 CC1$\pi^+$ selection efficiency as a function of true neutrino energy, true muon momentum, and true pion momentum in true CC1$\pi^+$ signal events. The distributions of true signal events before the selection is applied are shown in light grey, while the distributions after the full selection are shown in dark grey. Note that they are not stacked. . . . 66
5.30 Kinematic distributions for muon candidate tracks. . . . . 67
5.31 Kinematic distributions for pion candidate tracks. . . . . 67

6.1 Utilising a multisim approach, 100 universes were generated to assess the interaction-related systematic uncertainties. (a): The distributions of their cross sections (CV in red). Error bar shows the total interaction-related systematic uncertainty. (b): The distribution of event rates as a function of the track length of the leading MIP candidate (CV in black). (c) and (d): Covariance and fractional covariance matrices, respectively. . . . . 71
6.2 Cross sections and kinematic distributions for CCQE and CCMEC interactions in the default and alternative tunes of GENIE. Figures from Ref. [76]. . . . . 74
6.3 Utilising a multisim approach, 1000 universes were generated to assess the choice of model systematic uncertainties. (a): The distributions of their cross sections (CV in red). Error bar shows the total model-related systematic uncertainty. (b): The distribution of event rates as a function of the track length of the leading MIP candidate (CV in black). (c) and (d): Covariance and fractional covariance matrices, respectively. . . . . 75
6.4 Utilising a multisim approach, 100 universes were generated to assess the hadron reinteraction systematic uncertainties. (a): The distributions of their cross sections (CV in red). Error bar shows the total hadron reinteraction-related systematic uncertainty. (b): The distribution of event rates as a function of the track length of the leading MIP candidate (CV in black). (c) and (d): Covariance and fractional covariance matrices, respectively. . . . . 76

6.5 Utilising a multisim approach, 1000 universes were generated to assess the beam flux systematic uncertainties. (a): The distributions of their cross sections (CV in red). Error bar shows the total beam flux-related systematic uncertainty. (b): The distribution of event rates as a function of the track length of the leading MIP candidate (CV in black). (c) and (d): Covariance and fractional covariance matrices, respectively. . . . . 77
6.6 For each of the detector-related uncertainty parameters, the distribution of event rates as a function of the track length of the leading MIP candidate (green), with the CV (black) for comparison. . . . . 79

7.1 The measured total, flux-integrated CC1$\pi^+$ cross section on argon per nucleon (black point), compared with the prediction from GENIE MC (red line). The inner bars show the statistical uncertainty, while the outer bars show the sum of the statistical and systematic uncertainties. 87
7.2 Distribution of opening angles, i.e. the angle between the two MIP candidates, (a) before and (b) after applying a cut at 2.6 radians. The MC sample used here includes simulation of the DIC effect. . . . 89

8.1 An event display showing an example of an overlay event. Cosmic tracks from real off-beam data have been overlaid with a simulated beam event, circled in magenta. Figure from Ref. [88]. . . . . 92

# Chapter 1

# Introduction

The Standard Model (SM) of particle physics is a crowning achievement of science, with an astounding ability to predict most of the phenomena we observe in nature. The SM is a theory that describes all of the known elementary particles and their interactions via three of the fundamental forces. The fermions that make up ordinary matter consist of six quarks and six leptons. Each can be arranged into three generations of particles that (within each group) have the same quantum numbers as one another, but different masses. Forces are mediated by the gauge bosons: the electromagnetic force by the photon ($\gamma$), the weak force by the $W^{\pm}$ and $Z^0$ bosons, and the strong force via eight types of gluon ($g$). Finally, the scalar Higgs boson, discovered experimentally only in 2012 [2, 3], is responsible for giving mass to particles.

One of the very few areas where we have evidence of physics beyond the SM is the field of neutrino physics. Neutrinos are predicted by the SM to have no mass and are therefore not predicted to oscillate. We know that this is not so, as first shown by Super-Kamiokande and SNO [4, 5], but many questions remain. By what mechanism do neutrinos gain mass? What is the hierarchy and absolute scale of their masses? Are there more than three flavours of neutrino?

Further investigation of these and other neutrino properties will require high precision experiments. Liquid argon time projection chambers (LArTPCs) are a relatively new and promising detector technology that have become an active area of research and development in recent years. ArgoNeuT [6] and MicroBooNE [7] have already shown the high resolution capabilities of LArTPCs, allowing for the precise measurement of neutrino cross sections. MicroBooNE will be followed by ICARUS [8] and SBND [9] as part of the Short Baseline Neutrino Program (SBN). Oscillation measurements will also benefit from the ability of LArTPCs to scale well. ProtoDUNE [10] has demonstrated this ability, with the eventual DUNE far detector [11] planned to be many kilotons. It is an exciting time for the field, where LArTPCs will help to shed new light on the true properties of neutrinos.

## 1.1 Neutrino Interactions

In the SM, neutrinos can interact in a number of different ways. Broadly, these are classified as either charged current (CC) or neutral current (NC) interactions, depending on whether there is an exchanged $W$ or $Z$ boson, respectively. Example Feynman diagrams of these processes are shown in Figure 1.1.

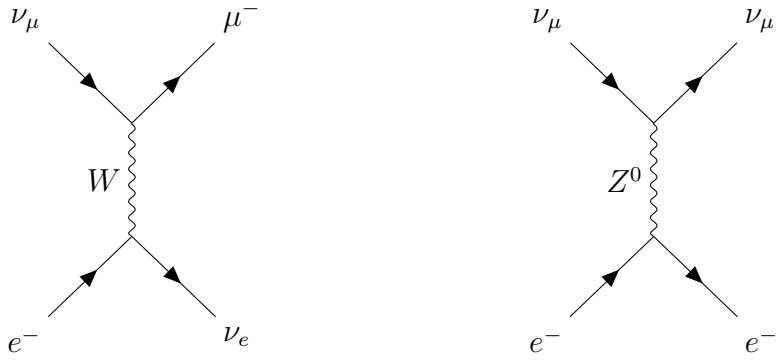


Figure 1.1: Feynman diagrams of example neutrino interactions: CC (left) and NC (right).

CC interactions are further categorised into three types that are dominant at different energy regimes: quasi-elastic (QE), resonant (RES), and deep inelastic scattering (DIS). Figure 1.2 shows the CC $\nu_\mu$ cross section as a function of neutrino energy, both in total and for each of these types, highlighting this energy dependence. For MicroBooNE, with a mean neutrino energy of about 0.8 GeV, there are significant amounts of both CCQE and CCRES interactions.

In CCQE interactions, the incident neutrino elastically scatters off of a nucleon, changing the flavor of one of the constituent quarks, and often knocking the nucleon (and possibly others) out of the nuclear target. The "quasi-" prefix refers to the fact that the neutrino in the initial state corresponds to a lepton of the same flavour in the final state, and thus it is not a truly elastic scatter.

In CCRES interactions, the incident neutrino instead excites a nucleon into a resonant state, which then decays to some final state. Most commonly, this is a nucleon and a pion. This process is the main source of the CC1$\pi^+$ events in MicroBooNE that are the primary topic of this thesis.

In CCDIS interactions, the neutrino imparts enough energy that the quarks in the target nucleon are broken up. This results in a shower of hadronic particles.

Additionally, neutrinos can undergo coherent scattering (COH), wherein an atomic nucleus acts as a single particle that is scattered off of, with negligible energy transfer. This also results in charged pion production. In MicroBooNE, only on the order of a percent of the total CC1$\pi^+$ interactions are from this process.

Figure 1.3 shows example Feynman diagrams of each of these interaction types.

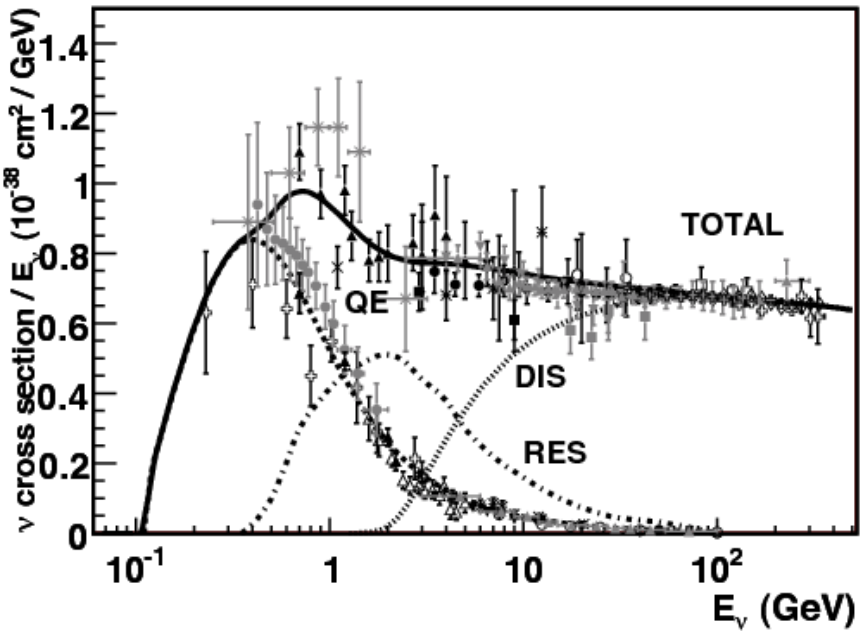


Figure 1.2: Total $\nu_\mu$ CC cross sections (per nucleon and for an isoscalar target) divided by neutrino energy, plotted as a function of energy. Data points are from various experimental measurements made from 1977 through 2011. Also shown are predictions from the NUANCE generator [12] for the different interaction mode cross sections: total (solid line), QE (dashed line), RES (dot-dashed line), and DIS (dotted line). Figure from Ref. [13].

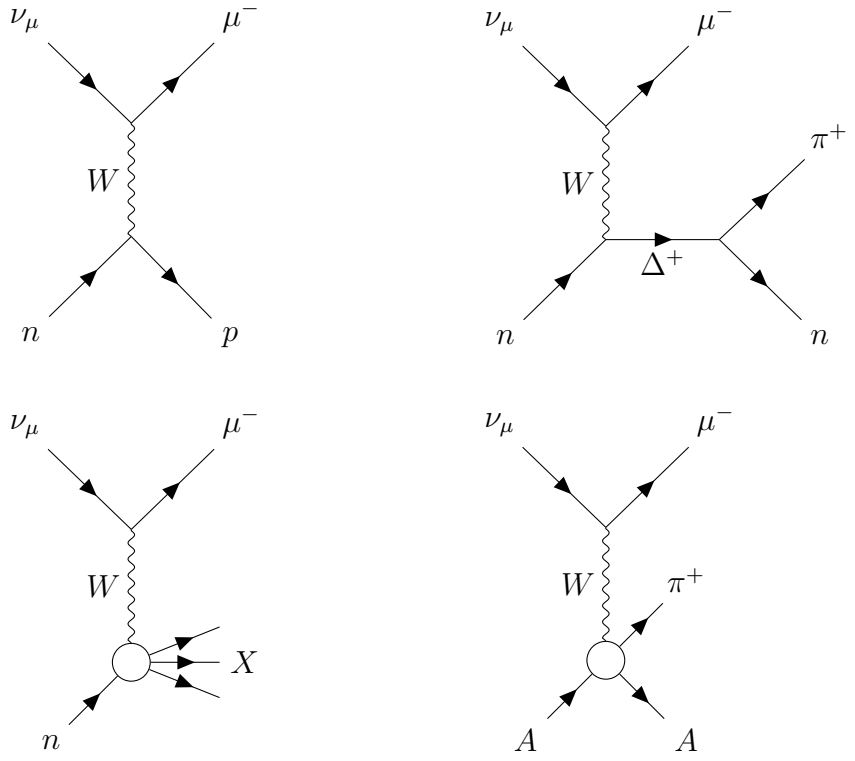


Figure 1.3: Feynman diagrams of example neutrino interactions: CCQE (upper left), CCRES (upper right), CCDIS (lower left), and CCCOH (lower right). $X$ refers to a hadronic shower and $A$ refers to an atomic nucleus.

### 1.1.1 Nuclear Effects and Final State Interactions

The types of interactions described in the previous section are a useful model when considering free nucleons. However, when neutrinos interact with heavy atomic nuclei (such as the argon used by MicroBooNE), additional effects must be taken into account. Nuclear effects refer to the need to account for the initial state of the bound nucleons, while final state interactions (FSI) refer to the fact that the particles produced in the initial interaction have to pass through the nuclear medium to exit, which can result in additional interactions or changes in kinematics. Figure 1.4 illustrates several different possible types of FSI.

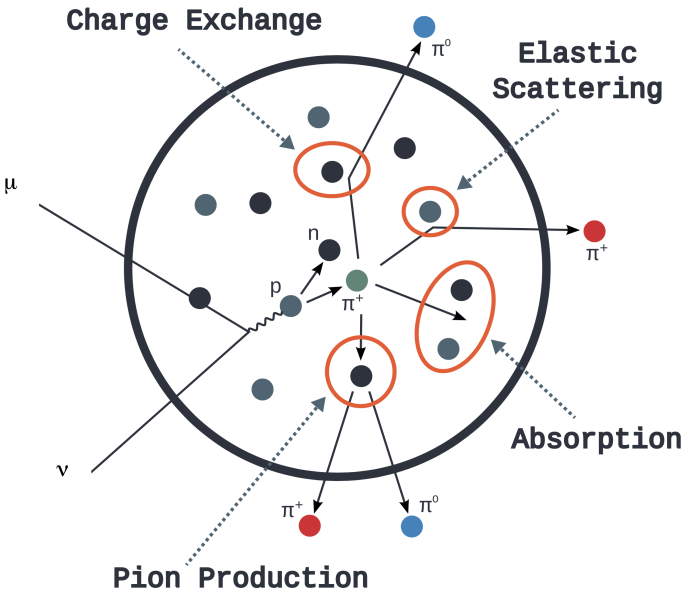


Figure 1.4: Examples of different possible types of FSI processes. Figure produced by T. Golan, see also Ref. [14].

Properly accounting for these effects is critical to accurately measuring cross sections. Significant efforts have been put toward developing models, though it continues to be an area of active research. A summary of the models used in MicroBooNE is given in Section 2.3.3.

These effects have also changed the way in which cross section signals are defined. Previously, results would be reported for, e.g., CCRES interactions. We now instead speak of, e.g., the CC1$\pi^+$ cross section. The difference is that the latter is based on only the particles that appear in the final state, regardless of the interactions that produced them. This both reduces model dependence and makes the measurement easier to compare to others.

### 1.1.2 Neutrino Oscillations

Another way in which neutrinos interact, which is not predicted by the SM, is through oscillations. This occurs because the neutrino flavour eigenstates $|\nu_\alpha\rangle$ and mass eigenstates $|\nu_j\rangle$ do not simply correspond. Rather, the flavour eignenstates are linear superpositions of the mass eigenstates, and vice-versa:

$$|\nu_\alpha\rangle = \sum_j U^*_{\alpha j}|\nu_j\rangle, \qquad |\nu_j\rangle = \sum_\alpha U_{\alpha j}|\nu_\alpha\rangle \tag{1.1}$$

where $U$ is a unitary mixing matrix. In the typical case of three flavour eigenstates and three mass eigenstates, this is known as the Pontecorvo-Maki-Nakagawa-Sakata (PMNS) matrix:

$$U = \begin{pmatrix} U_{e1} & U_{e2} & U_{e3} \\ U_{\mu 1} & U_{\mu 2} & U_{\mu 3} \\ U_{\tau 1} & U_{\tau 2} & U_{\tau 3} \end{pmatrix}. \tag{1.2}$$

This can also be parameterised in terms of three mixing angles $\theta_{12}$, $\theta_{13}$, and $\theta_{23}$, and a phase $\delta_{\mathrm{CP}}$:

$$U = \begin{pmatrix} 1 & 0 & 0 \\ 0 & c_{23} & s_{23} \\ 0 & -s_{23} & c_{23} \end{pmatrix} \begin{pmatrix} c_{13} & 0 & s_{13}e^{-i\delta_{\mathrm{CP}}} \\ 0 & 1 & 0 \\ -s_{13}e^{i\delta_{\mathrm{CP}}} & 0 & c_{13} \end{pmatrix} \begin{pmatrix} c_{12} & s_{12} & 0 \\ -s_{12} & c_{12} & 0 \\ 0 & 0 & 1 \end{pmatrix} \tag{1.3}$$

where $s_{ij} = \sin(\theta_{ij})$, $c_{ij} = \cos(\theta_{ij})$. This decomposition is easier to interpret, as each matrix contains only one of the mixing angles.

The phase $\delta_{\mathrm{CP}}$ corresponds to the extent to which there is violation of charge conjugation parity (CP) symmetry in the neutrino sector. If this value is non-zero, then the oscillation probabilities for neutrinos and antineutrinos would not be the same. Consequently, this could explain why we observe that the universe is made mostly of matter, rather than equal amounts of matter and antimatter as we would otherwise expect. CP violation has already been observed in the quark sector, but the effect is too small to fully account for the matter-antimatter imbalance we see [15]. A non-zero value of $\delta_{\mathrm{CP}}$ is favoured by the current global best fit [16], primarily driven by data from T2K [17] and NOνA [18].

This is not the only possible source of CP violation in the neutrino sector. Another arises if neutrinos are Majorana fermions (that is, are their own antiparticles), rather than Dirac fermions, as all other SM fermions are. Many past, current, and planned experiments investigate this by looking for neutrinoless double beta decay, which can only occur if neutrinos are Majorana particles. These include GERDA [19], EXO [20], MAJORANA [21], CUORE [22], and SNO+ [23], to name just a few. To date, no observation of this type of interaction has been made.

A third possibility is the existence of additional, "sterile" neutrino flavours. These neutrinos would not participate in the weak interaction, but would still oscillate with those that do. In 2007, MiniBooNE reported an excess of low energy electron-like events [24] (reanalysed in 2018 with a larger data set [1]), one explanation for which is the existence of sterile neutrinos. However, recent results from MicroBooNE disfavour this explanation [25].

Going back to the standard PMNS matrix, the evolution of the flavour eigenstates over time can be found using the Schrödinger equation. With significant effort, one can then derive that the probability of oscillation in a vacuum from an observed flavour $\nu_\alpha$ to an observed flavour $\nu_\beta$ after a time $t$ is given by:

$$P_{\nu_\alpha \to \nu_\beta}(t) = \left| \sum_j U^*_{\beta j} U_{\alpha j} \exp\left( \frac{-i\Delta m^2_{j1} L}{2E} \right) \right|^2 \tag{1.4}$$

where $\Delta m^2_{j1} = m^2_j - m^2_1$, L is the length travelled, E is the energy of the neutrino, and it has been assumed that the neutrino is travelling relativistically, such that $L \approx t$ and $E_j \approx \mathbf{p} + m^2_j/2E$ (where $\mathbf{p}$ is the momentum). In an oscillation experiment, the factors that can be controlled are $L$ and $E$.

It is also interesting to note that the probability does not depend on the absolute masses themselves, but rather their mass-squared differences. Furthermore, it does not depend on the sign of the mass-squared differences. However, this probability is altered for neutrinos travelling through matter, such that it *does* depend on the sign. Some measurements of mass splittings have been made, but two possible orderings remain: the normal ordering, in which $m^2_3 \gg m^2_2 > m^2_1$, and the inverted ordering, in which $m^2_2 > m^2_1 \gg m^2_3$. Future experiments such as DUNE will be able to resolve which is the case.

## 1.2 Pion Production Measurements

In recent years, a significant number of CC1$\pi^\pm$ cross section measurements have been made by various experiments. A summary of these is given in Table 1.1. They use a variety of different targets, beam fluxes, geometries, detector technologies, and signal definitions, which has both benefits and drawbacks. One drawback in particular is that it can make it very difficult to compare their results. Each result can, however, be compared to generator predictions, which allows for the evaluation of the various models used.

In 2011, MiniBooNE published a collection of many cross section measurements that were largely the first of their kind [28]. The first measurements of pion production come primarily from the ANL and BNL bubble chamber experiments of the

| Experiment | Target | Beam | Topology | Measurements | Ref. |
|---|---|---|---|---|---|
| K2K | CH | $\nu_\mu$ | CC1$\pi^+$ | $\frac{\sigma_{\mathrm{CC1}\pi^+}}{\sigma_{\mathrm{CCQE}}}(E_\nu)$ | [26] |
| MiniBooNE | $CH_2$ | $\nu_\mu$ | CC1$\pi^+$ | $\frac{\sigma_{\mathrm{CC1}\pi^+}}{\sigma_{\mathrm{CCQE}}}(E_\nu)$ | [27] |
| | | | | $\sigma(E_\nu)$ | [28] |
| | | | | $\frac{d\sigma}{dX} : X = T_\mu, T_\pi, Q^2$ | |
| | | | | $\frac{d\sigma}{dX}(E_\nu) : X = T_\mu, T_\pi, Q^2$ | |
| | | | | $\frac{d^2\sigma}{dXdY} : \{X, Y\} = \{T_\mu, \theta_\mu\}, \{T_\pi, \theta_\pi\}$ | |
| MINERνA | CH | $\nu_\mu$ | CC1$\pi^\pm$ | $\frac{d\sigma}{dX} : X = \theta_\pi, T_\pi$ | [29] |
| | | $\nu_\mu, \bar{\nu}_\mu$ | CC1$\pi^\pm$ | $\sigma(E_\nu)$ | [30] |
| | | | | $\frac{d\sigma}{dX} : X = p_\mu, \theta_\mu, Q^2$ | |
| | | $\bar{\nu}_\mu$ | CC1$\pi^-$ | $\sigma(E_\nu)$ | [31] |
| | | | | $\frac{d\sigma}{dX} : X = p_\mu, \theta_\mu, \theta_\pi, T_\pi, Q^2$ | |
| T2K | $H_2O$ | $\nu_\mu$ | CC1$\pi^+$ | $\sigma(E_\nu)$ | [32] |
| | | | | $\frac{d\sigma}{dX} : X = p_\mu, \cos(\theta_\mu), p_\pi, \cos(\theta_\pi), \cos(\theta_{\mu\pi})$ | |
| | CH | $\nu_\mu$ | CC1$\pi^+$ | $\frac{d\sigma}{dX} : X = p_\pi, \theta_\pi, \theta_{\mu\pi}, Q^2, \cos(\theta_{\mathrm{Adler}}), \phi_{\mathrm{Adler}}$ | [33] |
| | | | | $\frac{d^2\sigma}{dp_\mu d\cos(\theta_\mu)}$ | |
| ArgoNeuT | Ar | $\nu_\mu, \bar{\nu}_\mu$ | CC1$\pi^\pm$ | $\sigma$ | [34] |
| | | | | $\frac{d\sigma}{dX} : X = p_\mu, \theta_\mu, \theta_\pi, \theta_{\mu\pi}$ | |
| MicroBooNE | Ar | $\nu_\mu$ | CC1$\pi^+$ | $\sigma$ | – |

Table 1.1: A summary of modern CC1$\pi^\pm$ cross section measurements.

1980s [35, 36], which used light nuclear targets (hydrogen and deuterium) and were of low statistics. Nonetheless, this data has been used as the basis for pion production by many generators, including NUANCE, which was employed by MiniBooNE. They found that their data was on average 23% higher than prediction. Since MiniBooNE used a heavy nuclear target, nuclear effects and FSI were now a concern, where they had not been in the earlier experiments. Since these measurements were the first of their kind, it was not clear to what extent these effects were the cause of the discrepancy, but more study was clearly needed.

In 2015, MINERνA published cross sections in terms of the angle and kinetic energy of the pion [29]. Their signal definition differed somewhat from MiniBooNE's. MiniBooNE allowed only $\pi^+$ (not $\pi^-$), did not allow $\pi^0$ or other additional mesons, and did not include any kinematic cuts. By contrast, MINERνA allowed either $\pi^\pm$,

did allow $\pi^0$ and other additional mesons, and included kinematic cuts on both the neutrino energy and the invariant hadronic mass. The cuts were intended to make their measurement more comparable to MiniBooNE's, accounting for MINERvA's higher neutrino energy.

Figure 1.5 shows a comparison between MINERvA and MiniBooNE $d\sigma/dT_\pi$ data, and predictions from GENIE for each experiment. Above ~100 MeV, the shapes of the two sets of data are in agreement, which MINERvA interpreted to indicate consistency in pion absorption FSI processes. However, there is shape disagreement at low values of $T_\pi$, which was unexplained by existing models. In terms of normalisation, MINERvA's higher neutrino energy should normally lead to higher cross section values for this process, so the agreement in normalisation at higher $T_\pi$ is also unexpected. Concerning GENIE, it predicts MINERvA's shape but not normalisation, while it predicts MiniBooNE's normalisation but not shape. Overall, there is significant disagreement, which further highlighted the need for improved understanding of nuclear effects.

In 2016, MINERvA published additional cross sections for muon kinematics and

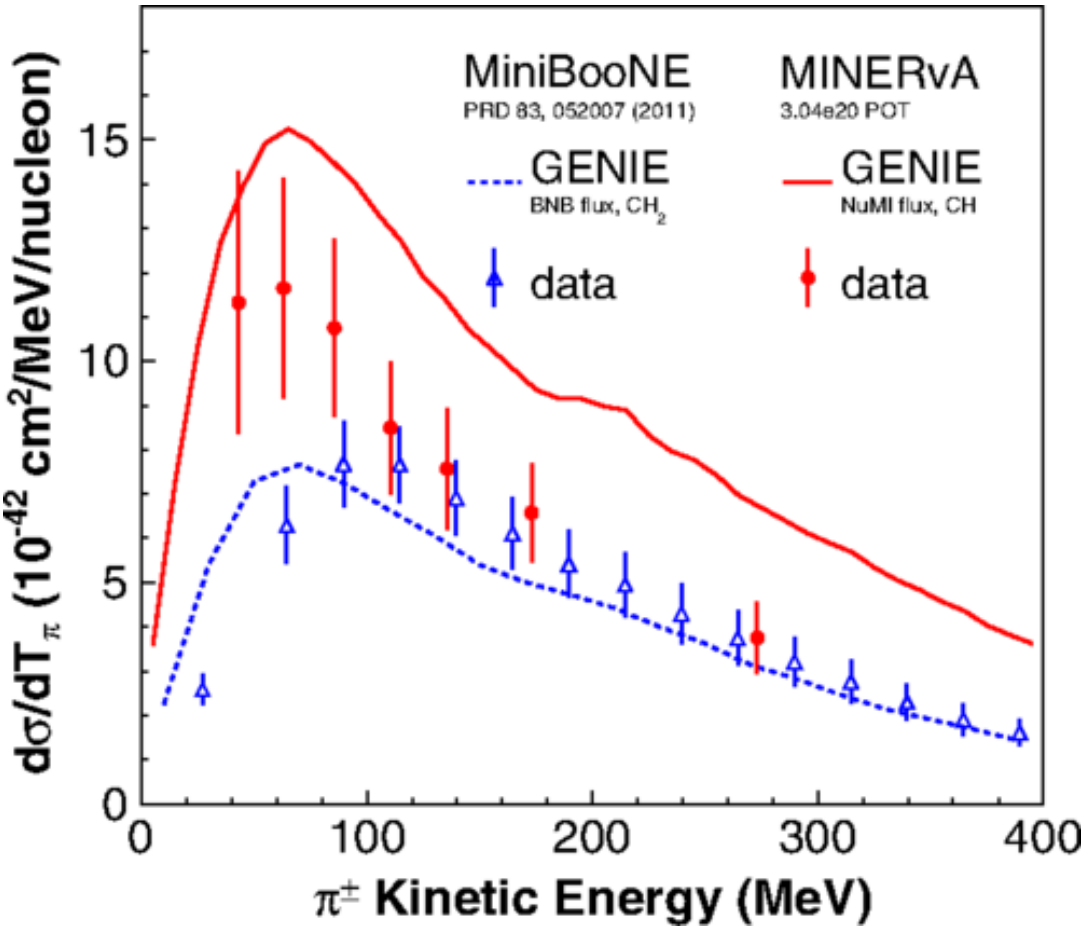


Figure 1.5: Comparison between MINERvA and MiniBooNE $d\sigma/dT_\pi$ data, and predictions from GENIE for each experiment. Figure from Ref. [29].

for four-momentum transfer $Q^2$ [30]. This analysis differed form the previous result in two important ways. First, significant improvements were made to the flux estimate [37]. And second, the signal definition was changed to cut on the invariant hadronic mass *after* the effects of FSI ($W_{exp}$), rather than before ($W_{true}$). The previously measured cross sections were also reanalysed with these updates, with the results made available as a public data release [38]. The normalisation agreement with MiniBooNE improved slightly, but both normalisation and shape discrepancies were still present [39].

In 2017, T2K published various cross sections on water in terms of muon and pion kinematics [32]. The data were found to be in good agreement with the NEUT generator [40]. GENIE agreed well in shape, but over-predicted the normalisation.

In 2018, ArgoNeuT published the first pion production cross sections on argon [34]. This is of particular interest since it is also the target used by MicroBooNE, and is planned to be used by the two other short-baseline neutrino program experiments (SBND and ICARUS) and the DUNE experiment. For all measurements, the GiBUU generator [41] was found to be in good agreement. NuWro [42] and NEUT predictions were similar to each other and over-predicted the normalisation. The GENIE prediction was higher still, likely stemming from too high of a non-resonant background prediction.

In 2020, T2K published a new set of cross sections on hydrocarbon, including the first modern measurement of the Adler angles [33]. This is the same target that MINERνA used, but comparisons are still limited by the various differences mentioned at the beginning of this section (beam flux, signal definition, etc.). That said, in the small region of overlapping phase space (events with $1 < p_\mu < 2$ GeV/c and $0.9 < \cos\theta_\mu < 1.0$), the two results are found to be consistent [43]. There are many interesting details in the comparisons to generator predictions, which are detailed in Ref. [43] but are largely outside the scope of this work. Broadly speaking, they found that all generators considered (NuWro, NEUT, and three versions of GENIE) provided good descriptions for muon kinematic variables and for the muon-pion opening angle. Agreement for pion kinematic variables and derived quantities ($Q^2$ and the Adler angles) was generally worse and predictions were more varied among the generators.

Overall, recent years have seen significant progress in the measurement and simulation of CC1$\pi^\pm$ interactions. Direct comparison between experiments remains difficult or impossible, but generators allow for useful indirect comparisons and evaluations of models to be made. There continues to exist tension between recent cross section results and generator predictions, especially for pion kinematics. It is clear that an important factor in these discrepancies is our incomplete understanding of nuclear effects and FSI. Generators have improved in their implementation of

theories of these effects and have benefited from the wealth of recent data necessary to tune their predictions. Increased cooperation between experimentalists, theorists, and generator experts has been and will remain of critical importance to advances in this field.

This thesis presents the first measurement of CC1$\pi^+$ interactions in MicroBooNE.

# Chapter 2

# The MicroBooNE Experiment

This chapter describes the details of how the MicroBooNE experiment functions. Section 2.1 describes the detector itself, Section 2.2 describes the source of neutrinos, Section 2.3 describes how various aspects of the experiment are simulated, and Section 2.4 shows how raw data is processed into a full reconstruction of the interactions.

## 2.1 The MicroBooNE Detector

MicroBooNE is a 170 ton liquid argon time projection chamber (LArTPC) located in the Booster Neutrino Beam (BNB) at the Fermi National Accelerator Laboratory (Fermilab). The TPC is a rectangular cuboid measuring approximately 256 x 233 x 1037 cm. It is housed in a cylindrical cryostat, as shown in Figure 2.1.

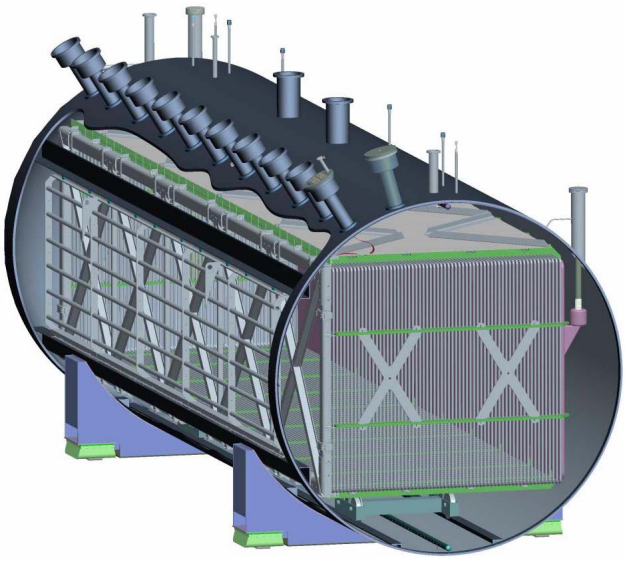

Figure 2.1: Schematic of the MicroBooNE LArTPC, housed inside the cryostat. Figure from Ref. [44].

Figure 2.2 illustrates the basic principles of operation of the LArTPC. When charged particles travel through the detector, they ionise the liquid argon. An electric field of 273 V/cm is applied that causes the ionisation electrons to drift toward one side of the detector (the anode), which is instrumented with three planes of sense wires. Bias voltages are applied to the wires such that the electrons induce a signal on the first two planes and are then collected on the third. The collection plane is vertical, while the induction planes are angled at ±60 degrees to the vertical. The distance between adjacent wires on each plane is 3 mm, which enables high resolution imaging.

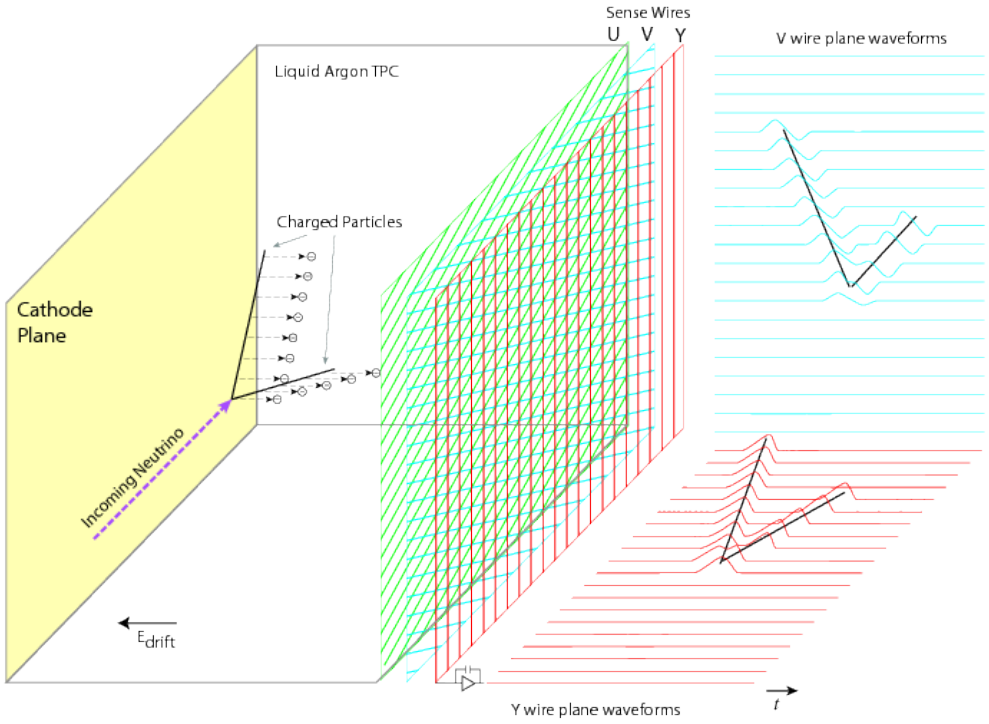


Figure 2.2: A diagram showing the operating principles of the MicroBooNE LArTPC. Figure from Ref. [44].

Additionally, a system of 32 photomultiplier tubes (PMTs) is located behind the wire planes, as shown in Figure 2.3. They collect scintillation light, used in part to help provide timing information for the tracks. There are also 4 light guide paddles used for the purposes of R&D, but they are not typically involved in MicroBooNE analyses, including this one. Together, the wire planes and PMTs allow for the full 3D reconstruction of events.

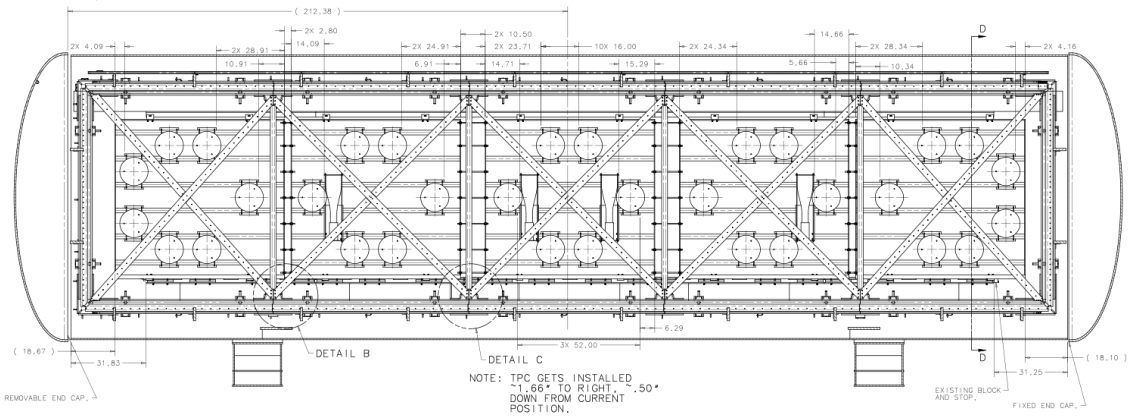


Figure 2.3: A schematic of the placement of the PMTs in MicroBooNE. Light guide paddles are also shown, but are not involved in this analysis. Figure from Ref. [45].

## 2.2 The Booster Neutrino Beam

The primary source of neutrinos for the MicroBooNE experiment is the Booster Neutrino Beam (BNB), part of Fermilab's Accelerator Complex. An overview of the Complex is shown in Figure 2.4, including the four main components: the Linear Accelerator (Linac), Booster, Recycler Ring, and Main Injector. Figure 2.5 gives an overhead view of Fermilab showing what this looks like in actuality.

The Booster is a synchrotron that is 474 meters in circumferences and operates at a frequency of 15 Hz. It receives a primary beam of protons from the Linac. The Booster accelerates these protons from an initial energy of 400 MeV up to 8 GeV. The Recycler and Main Injector can be used to further accelerate the protons, but MicroBooNE is a lower energy experiment that does not use these as part of its BNB beamline. However, the Neutrinos at the Main Injector (NuMI) beamline is in use by the MINERνA and NOνA experiments, and MicroBooNE does receive a flux of highly off-axis neutrinos from this secondary source.

After being accelerated, the protons are impinged upon a beryllium target, creating muons, pions, and other secondary particles. A focusing horn is used to separate secondaries with positive and negative charges. In order to produce a beam composed primarily of neutrinos, positively charged particles are focused and negatively charged particles are defocused. The horn is also capable of doing the opposite to create a beam of primarily anti-neutrinos. The focused secondaries decay in a decay pipe, and a beam dump at the end is used to stop the non-neutrino particles that this produces. The neutrinos continue through several hundred meters of dirt before finally reaching MicroBooNE.

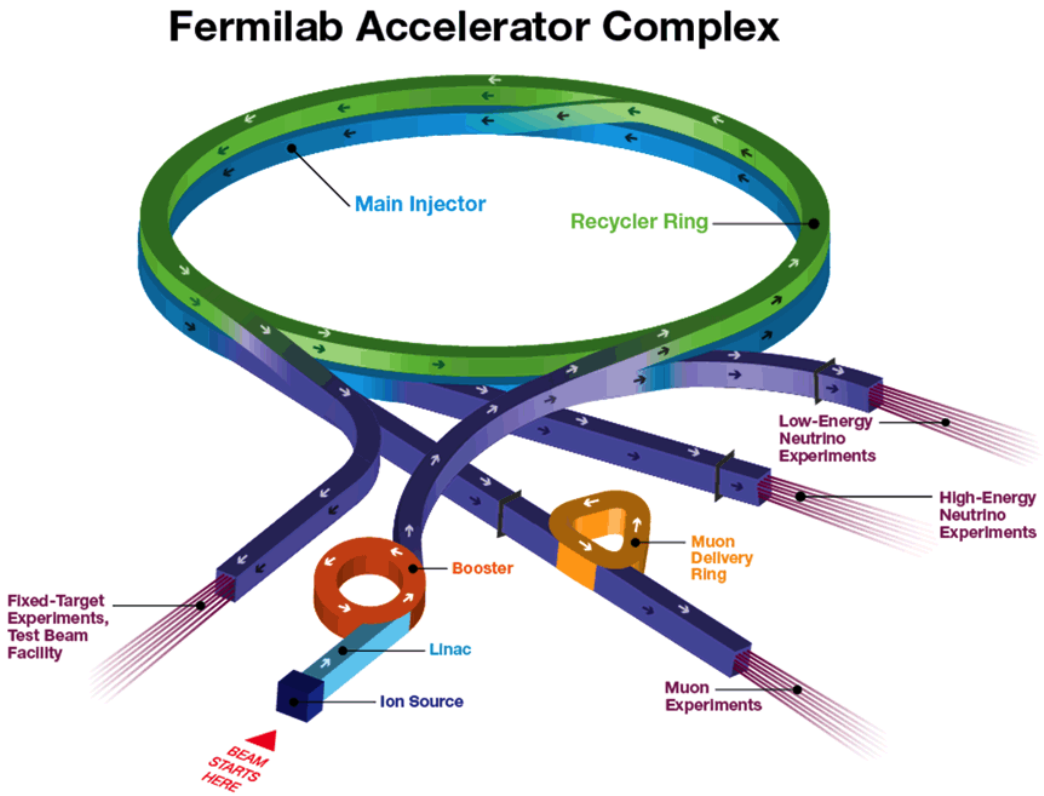


Figure 2.4: An overview of the Fermilab Accelerator Complex. Figure from Ref. [46].

Figure 2.5: Aerial view of Fermilab with features of the Accelerator Complex marked: the Linac (cyan), Booster (red), path of the accelerated protons from the Booster to the target (pink), BNB (blue), the Main Injector and Recycler (green), and the location of MicroBooNE within the BNB (yellow cross).

## 2.3 Event Simulation

This section describes how various aspects of MicroBooNE are simulated. The simulations used here are based on the Monte-Carlo (MC) method. Simulations are used for the tuning of analyses, for estimation of background event rates, and for comparisons to data.

### 2.3.1 Neutrino Flux Simulation

The first step in simulating events is to predict how many neutrinos come from the BNB per proton-on-target per unit area, as a function of energy. This includes both the $\nu_\mu$ that compose most of the beam and that we are primarily interested in, as well as the fluxes of $\bar{\nu}_\mu$, $\nu_e$, and $\bar{\nu}_e$. MicroBooNE uses a framework that is based on the MiniBooNE flux simulation [47]. GEANT4 is used to simulate the flux generation, starting from the interaction of primary protons with the beryllium target, and continuing through production and decay of mesons and muons, resulting in a beam of neutrinos [48]. Updates have been made from MiniBooNE's framework to include $K^+$ production data and HARP data in the fit [49]. The resulting prediction of the flux received at MicroBooNE is shown in Figure 2.6. Note that MicroBooNE took data only in neutrino mode, so the flux prediction for the antineutrino mode is not shown here.

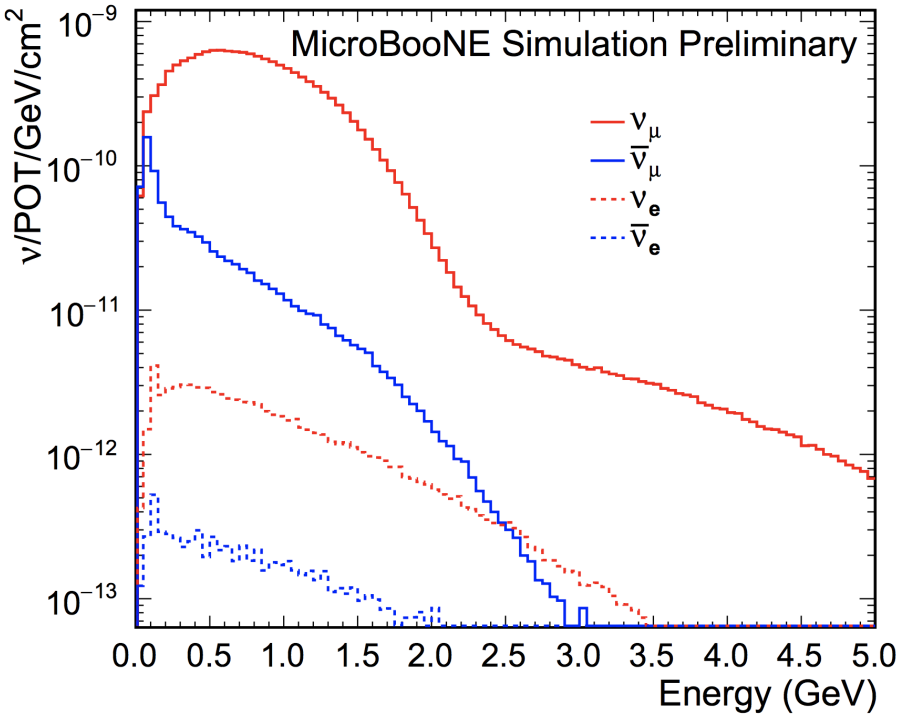


Figure 2.6: Prediction from simulation of the absolute neutrino flux through MicroBooNE, averaged over the TPC volume, while in neutrino mode. Fluxes are shown for $\nu_\mu$, $\bar{\nu}_\mu$, $\nu_e$, and $\bar{\nu}_e$. Figure from Ref. [50].

### 2.3.2 Cosmic Ray Simulation

MicroBooNE is a near-surface-level detector with no overburden. This means that the rate at which particles from cosmic rays (CRs) enter the detector is quite high. Each recorded "event" is 4.8 ms of TPC readout, which is predicted to contain 25 CR muons on average. Although data recorded with the beam off (and therefore containing only CRs) can be used to account for this background, events where both neutrinos and CRs are present must also be considered, as it is possible to select a CR interaction instead of the neutrino interaction. For this analysis, all such selected interactions that contain CR particles are considered background. The Cosmic Ray Simulations for Kascade (CORSIKA) generator [51] is used to simulate these CRs that occur "in-time" with the beam.

One issue with this simulation-based approach is that there are not associated systematic uncertainties. Future analyses plan to overcome this using "overlays," where simulated neutrino interactions and beam-off CR data are combined (see Section 8.3 for further discussion). This approach was not ready to been used in this analysis.

### 2.3.3 Neutrino Interaction Simulation

Beam neutrinos are passed to the GENIE generator, which handles simulating neutrino interactions within the detector [52, 53]. This analysis uses two different GENIE model sets, or "tunes," a default tune and an alternative tune that is used to evaluate systematic uncertainties. The models used in each of these tunes are listed in Table 2.1. The models of the alternative tune were chosen to be more theory-driven and relevant for MicroBooNE's energy scale. Section 6.1.3 describes the use of the alternative tune for evaluating systematic uncertainties.

| Model Element | Default GENIE Tune | Alternative GENIE Tune |
|---|---|---|
| Nuclear Model | Bodek-Ritchie Fermi Gas [54] | Local Fermi Gas [55, 56] |
| FSI | hA [53] | hA2014 [53] |
| Quasi-Elastic | Llewellyn-Smith [57] | Nieves [55, 56] |
| Meson-Exchange Currents | Empirical [58] | Nieves [55, 56] |
| Resonant | Rein-Sehgal [59] | Berger-Sehgal [60–63] |
| Coherent | Rein-Sehgal [59] | Berger-Sehgal [60–63] |

Table 2.1: The two GENIE model sets used in this analysis.

Both nuclear models used in this analysis are based on treating the nucleus as a Fermi gas, wherein the nucleons are in a constant potential well and the only interactions between them are due to Pauli blocking. This relatively simple model can be modified in a number of ways. The alternative tune instead uses a local Fermi gas model [55], where the potential is no longer constant, but rather is based

on the radial position of the nucleons within the nucleus. This is further built upon in the Bodek-Ritchie model [54] used by the default tune by also considering two nucleon correlations, leading to a higher tail in the distribution of nucleon momenta.

Final State Interaction (FSI) simulations are based on an Intra-Nuclear Cascade model [64], where hadrons produced within the nucleus undergo a series of individual interactions with the nucleons, leading to a hadronic cascade (see Figure 1.4). The hA model [53] used in the default tune differs by using the total cross section for each FSI process, based on empirical data, rather than simulating the individual hadronic interactions. The hA2014 model [53] used in the alternative tune is an updated version, based on much more data. It also includes Coulomb corrections, which account for the fact that the lepton produced in the initial interaction is affected by the electric field of the nucleus.

The remaining model elements provide cross sections for specific interaction processes. Calculating these from the first principles of quantum field theory is unfortunately not feasible. Instead, they are approximated using "form factors" that encapsulate the structure of the nucleons.

For quasi-elastic (QE) interactions, the form factors of Llewellyn-Smith [57] are used in the default tune and those of Nieves [55, 56] are used in the alternate tune. An important difference between them is that only the latter includes Random Phase Approximation (RPA) corrections, which consider interactions between the nucleons, rather than treating them as free.

Meson-Exchange Current (MEC) refers to interactions that are similar to QE, but involve two initial and two final nucleons. The default tune uses an empirical model [58], which unfortunately does not have associated uncertainties (see Section 6.1.3). For the alternate tune, the Nieves model that is used for QE also includes a more theory-driven model of MEC.

Resonant (RES) and coherent (COH) interactions are handled together. In the default tune, the Rein-Sehgal model [59] is used, which again uses specific form factors to approximate the cross section. The alternate tune instead uses the Berger-Sehgal model [60–63], which is an updated version that includes improvements based on additional pion production cross section data.

### 2.3.4 Detector Simulation

Once Genie has simulated the interactions, the resulting particles are passed to GEANT4, which propagates them through the liquid argon. It also handles the simulation of ionisation electrons drifting to the wire planes and of scintillation light travelling to the PMTs.

One detector effect of particular note is known as the space charge effect (SCE).

SCE refers to a build-up of slow-moving, positively charged ions in the detector (caused in MicroBooNE by ionisation from CRs), leading to a distortion of the electric field within the detector. MicroBooNE has undertaken a study of SCE and how it affects this experiment [65, 66]. This effect is both included in the detector simulation and is corrected for in this analysis.

There is one known significant detector effect that is not simulated in this analysis. When ionisation electrons pass by the wire planes, it is assumed that they induce a charge on only the wire that they are closest to. In reality, a significant amount of charge is induced on a number of wires to either side: $\pm 10$ on the first induction plane and $\pm 2$ on the second induction plane and on the collection plane [67]. This effect is referred to as dynamic induced charge (DIC). The main result of this effect is to broaden dE/dx distributions. A preliminary version of a DIC simulation is used in this analysis (discussed further in Section 7.1), but a final and fully integrated DIC simulation is an area of future work (see Section 8.1).

## 2.4 Event Reconstruction

This section describes how raw data recorded in MicroBooNE is processed and turned into reconstructed events that can be further analysed.

### 2.4.1 Hit Reconstruction

One of the main sets of data MicroBooNE records is the charge detected by the sense wires over time. Processing these signals is complex, with many more details than can fit within the scope of this thesis. An overview is given here, but detailed descriptions of the techniques used in MicroBooNE are available in Refs. [67] and [68].

The signal that is measured is the combination of both the "original signal" from the ionisation electrons, as well the wire field response and noise generated by the electronics. The goal is to recover the original signal, which in MicroBooNE is done via a process known as deconvolution [69]. This has also been used successfully in the past by ArgoNeuT [70]. If this process accounts only for changes in the charge near each wire over time, it is referred to as one-dimensional (1D) deconvolution. In practice, due to the DIC effect described in the previous section, the measured signal depends also on the charge present in other nearby wire regions. This can also be accounted for, by means of 2D deconvolution. Figure 2.7 shows a comparison of the noise filtering only, 1D deconvolution, and 2D deconvolution for an example event in MicroBooNE. Currently, MicroBooNE uses only the 1D technique, but this could be updated for future analyses.

Once the signal is deconvolved, an algorithm is used to find peaks in the waveforms, and these identified regions are fit with a Gaussian shape. Objects called "hits" are reconstructed from this data, which includes the width of the signal and the time of the peak. Hits serve as the base unit that further reconstruction steps build upon.

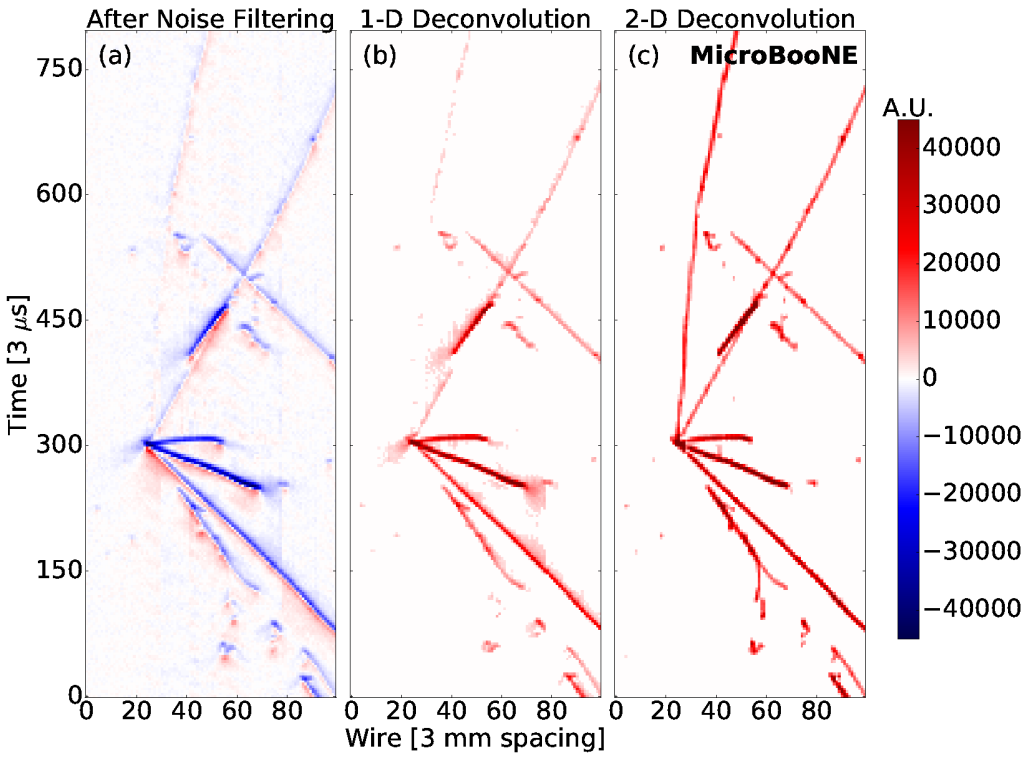


Figure 2.7: A comparison of the measured signal on one of the induction planes (the U plane) from an example candidate neutrino data event in MicroBooNE after noise filtering, 1D deconvolution, and 2D deconvolution. It can be seen that the signal is successively more defined. Figure from Ref. [67].

### 2.4.2 Pandora Pattern Recognition

Reconstructed hits are turned into higher level objects that are classified as tracks and showers using the Pandora Software Development Kit, a multi-algorithm pattern recognition framework [71, 72]. Pandora takes as input reconstructed hits and returns Particle Flow Objects (PFOs), which each represent a single interaction. PFOs are composed of Particle Flow Particles (PFPs), which each represent a single reconstructed object (e.g. a track or shower). PFOs also structure the PFPs in a hierarchical "particle flow" relationship. Each PFP may be a parent or daughter of another, with parents being closer to the start of the interaction and daughters further away.

The first step Pandora takes is to group hits together into "clusters" on a per-plane basis, giving 2D reconstructions. Pandora compares the information from the different planes and identifies any areas where ambiguities exist. For instance, one plane may have two clusters that correspond to only one cluster on another plane. Clusters are merged or split to resolve this, and this process is repeated until all ambiguities are resolved. The result is a single 3D reconstruction. Each cluster is identified as being either "track-like" or "shower-like," and the corresponding object is reconstructed accordingly.

Pandora performs this process in two passes: one to identify CR interactions and one to identify neutrino interactions. The CR pass assumes that particles are most likely to be track-like and downward-going, while the neutrino pass assumes they're most likely to be forward-going. In the neutrino pass, a final step is to group PFPs into PFOs and identify their hierarchy. Candidate interaction vertices are identified, and a neutrino PFP is created at the chosen vertex as the foremost parent in the interaction. The PFPs that are daughters of this are identified, further PFPs are identified as daughters of those particles, and so on until every non-neutrino PFP has a parent. An example of a simulated event reconstructed using Pandora, with labeled PFPs and hierarchy, is given in Figure 2.8.

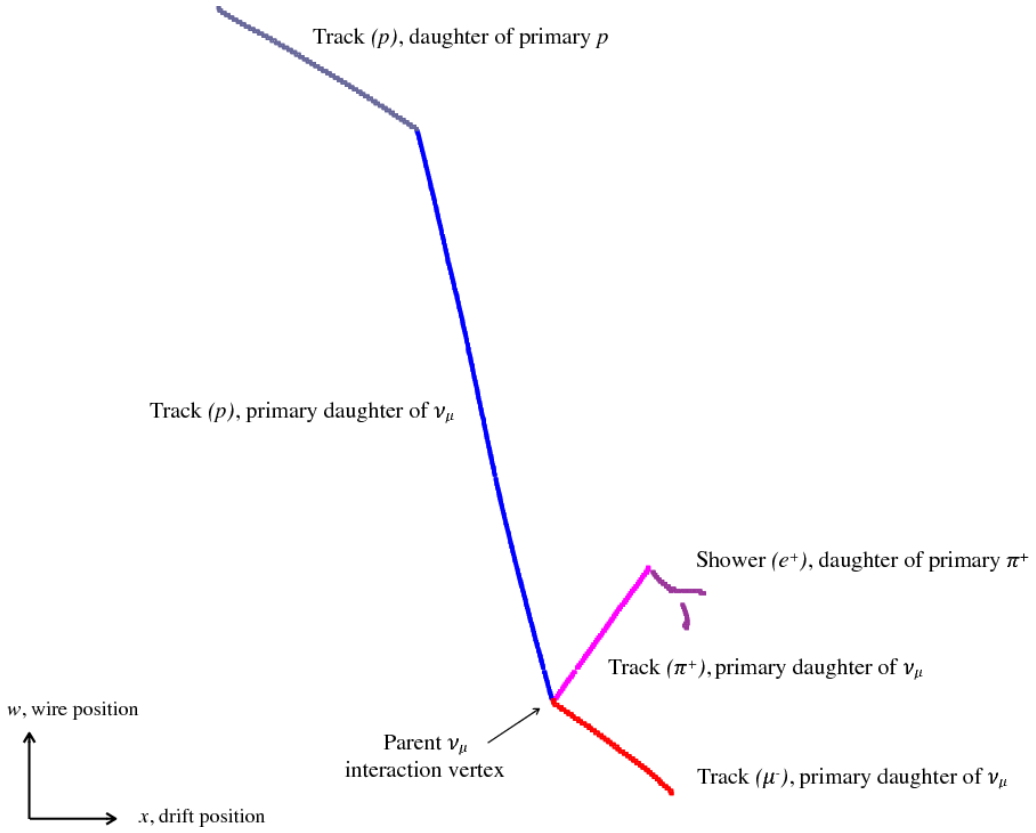


Figure 2.8: A simulated event in MicroBooNE reconstructed with Pandora, showing an example of the particle hierarchy. Figure from Ref. [72].

### 2.4.3 Optical Reconstruction

Optical information from the PMTs situated behind the wire planes is also reconstructed into higher level objects. The PMT signals are split into a high-gain channel and a low-gain channel. The high-gain channel is used by default to create a gain-corrected waveform. The low-gain channel serves as a backup in cases where the high-gain channel is saturated. As with the TPC reconstruction, the aim is to reconstruct hits from these waveforms. A baseline of activity is established and an algorithm is used to find peaks, providing information such as the width and the peak height, which is stored as hit objects.

The next step is to reconstruct "flashes" that group hits together. Flashes correspond to the light produced from a single interaction. They therefore consist of the in-time hits from a collection of PMTs. In order to account for late light pulses, there is an $8\mu$s dead time after each flash during which the reconstruction of other flashes in the same area is not allowed. Flashes are used to aid in identifying neutrino interactions, the process of which is described in Section 4.1.

# Chapter 3

# Simulation Benchmarking and First CC Inclusive Selections

In addition to the main CC1$\pi^+$ cross section analysis described in this work, I undertook a number of service tasks. Section 3.1 describes work that I did to benchmark the MicroBooNE MC simulation that was used in the first physics articles. Section 3.2 describes contributions I made to MicroBooNE's first steps toward a CC inclusive cross section analysis.

## 3.1 Simulation Benchmarking

MicroBooNE first started taking data in October 2015. Soon thereafter, an important step in validating MicroBooNE's MC simulation and reconstruction, as well as its detector performance, was to make comparisons to data. Dr. Adam Lister and I worked together to produce a detailed analysis of areas of agreement and disagreement across many different variables, using off-beam data and CORSIKA MC events. This provided the first real benchmark of MicroBooNE's reconstruction algorithms for hits, tracks, vertices, flashes, and calorimetry. We wrote both an internal technical note and a public note that detailed our findings [73].

Broad agreement was seen, but a number of specific problematic areas were identified. Most discrepancies were caused by a couple of known effects that were not yet simulated: wire noise and the space charge effect (see Section 2.3.4). This analysis showed the extent of these effects and reinforced the need for their inclusion in the simulation. Two example plots showing this are given in Figures 3.1 and 3.2. Some discrepancies, however, were unexpected. In particular, the angular distribution of cosmic tracks seemed to be slightly mis-modelled.

Flagging up issues such as these is important to all MicroBooNE analyses. These first comparisons laid the groundwork for the development of a continuous integra-

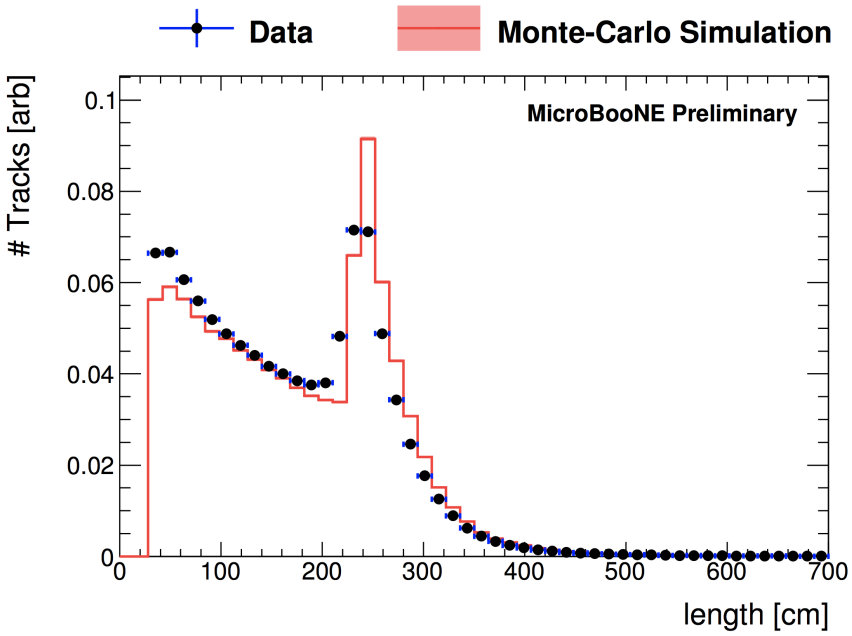


Figure 3.1: An example plot showing a comparison of track lengths in (area-normalised) cosmic data and MC. The peak at ∼230-250 cm is due to tracks that travel the whole height or width of the detector. This peak is lower in data due to the space charge effect, which was not modelled in this generation of the MC. The difference at the start of the distribution is also due to SCE. Figure from Ref. [73].

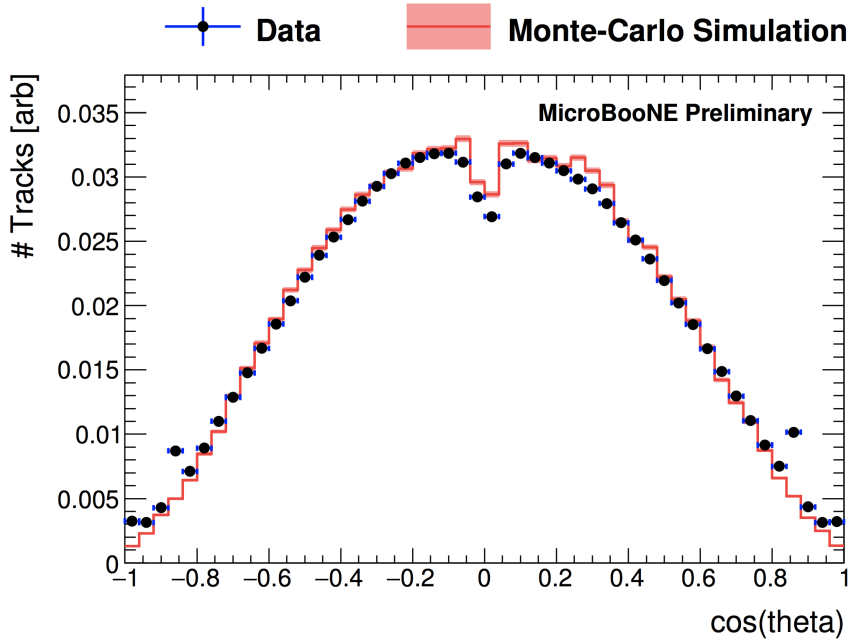


Figure 3.2: An example plot showing a comparison of the cosine of the polar angle $\theta$ between tracks and the beam axis, in (area-normalised) cosmic data and MC. Tracks less than 30 cm long have been cut. Data is higher than MC at $\cos(\theta) \approx \pm 1$ (the beam direction) and $\pm 0.85$ (the angle of the two induction planes). In both cases, the disagreement was attributed to noise that was not modelled in the MC. The dip at $\cos(\theta) \approx 0$ is due to difficulty in reconstructing tracks that are parallel to the collection plane. Figure from Ref. [73].

tion system that became standard in MicroBooNE. I was not personally involved in this work, but I describe it here briefly for completeness. Every time a new simulation release was tagged, plots similar to those that we initially made were automatically generated. MicroBooNE shifters monitored these plots, comparing them to corresponding plots from recent releases, as well as to a baseline release. This allowed for incremental validation of the simulation, wherein bugs or other issues could be found much more quickly.

## 3.2 CC Inclusive Analysis Contributions

One of the first challenges for MicroBooNE analyses was to distinguish between neutrino interactions and cosmic background. Accordingly, a charged current (CC) inclusive analysis was developed, whose main goal is doing just that. Many MicroBooNE collaborators worked together to create two different selections (Selection I and Selection II) in parallel. The simulation work described in the previous section was largely undertaken in support of this.

The two selections used different strategies and reconstruction algorithms. A diagram giving an overview of both selections is shown in Figure 3.3. Selection I focused on identifying the muon coming from the $\nu_\mu$ CC interactions. Selection II took a more complex approach, with different treatments for events with different multiplicities. In both cases, first a flash with at least 50 PE must occur during the beam window, in order to identify neutrino interactions. The next several cuts on flash and vertex position ensure good reconstruction quality.

Selection I, however, selects the most forward-going interaction, in an attempt to further reduce cosmic backgrounds. It does this by constructing a momentum-like variable that is the average direction of all tracks coming from the neutrino vertex, weighted by their length. This selection finishes by requiring that the longest track (likely the muon) is contained and has a minimum length of 75 cm.

After the quality cuts, Selection II splits into different paths for different multiplicity events. Events with multiplicity 1 are treated similarly to Selection I, although there is an additional cut that makes use of dE/dx information. One of the main backgrounds for events with multiplicity 2 is cosmic muons decaying to Michel electrons, which is reduced by evaluating multiple criteria. First, the dE/dx values at either end of the longer track are compared. If the vertex is at the end with larger dE/dx, it is a sign that the longer track may be a cosmic muon, with the vertex marking the Michel decay. Second, if the longer track exits the fiducial volume in the vertical direction, this is a sign that it may be an entering cosmic muon. If either of these two criteria are true *and* the shorter track is less than 30 cm long, it is identified as a Michel decay and removed from the selection. The other main background

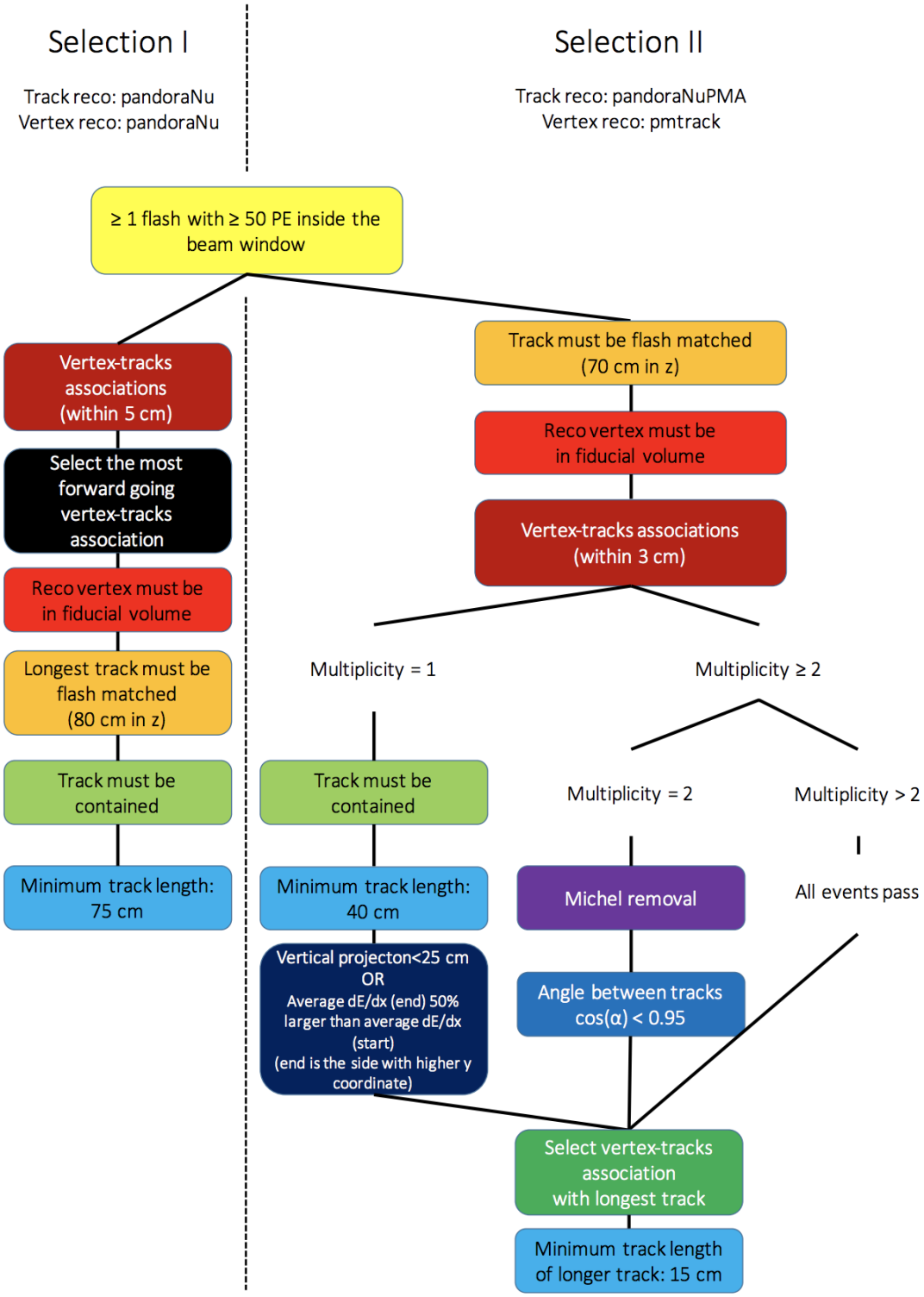


Figure 3.3: An overview of the two CC inclusive selections. Boxes of the same colour indicate similar types of cuts (although the cut values may differ). Figure from Ref. [74].

for multiplicity 2 events is tracks that are incorrectly broken by the reconstruction. In this case, a cut is made on the opening angle between them, as broken tracks are expected to be close to back-to-back. All events with multiplicity greater than 2 pass to the final part of the selection, as the cosmic background here is already low. This final part of the selection, for events of all multiplicities, involves two cuts. First, if there are multiple candidate neutrino interactions remaining ($\sim$ 3% of events), the interaction with the longest track is selected. And finally, the longest track (which is the muon candidate) must be at least 15 cm.

The two selections have different strengths and weaknesses. Selection I has significant bias toward forward going tracks, and its requirement of containment for the muon candidate considerably limits phase space and acceptance. However, it does not have any multiplicity bias. Selection II makes use of dE/dx information, but the calorimetric calibration was still an area of ongoing effort, which weakens the extent to which it can be relied upon. Selection II's differing treatment for different multiplicities necessarily introduces some bias, but allows for significantly better acceptance by not requiring containment for events with multiplicity greater than 1.

The results of these selections were detailed in a public note [74], which showed that the automated selected of neutrino interactions in a LArTPC on the surface was indeed possible. Figure 3.4 shows the distributions of track range and track $\cos(\theta)$ for Selection I, while Figure 3.5 shows these distributions for Selection II. Figure 3.6 shows an example event display of a selected CC event. On behalf of the MicroBooNE collaboration, Dr. Lister and I presented the results of these studies in a poster session at the XXVII International Conference on Neutrino Physics and Astrophysics (Neutrino 2016). A paper with those results was published as part of the conference proceedings [75].

This work served as a starting basis for the eventual CC inclusive cross section analysis, which is described in the next chapter.

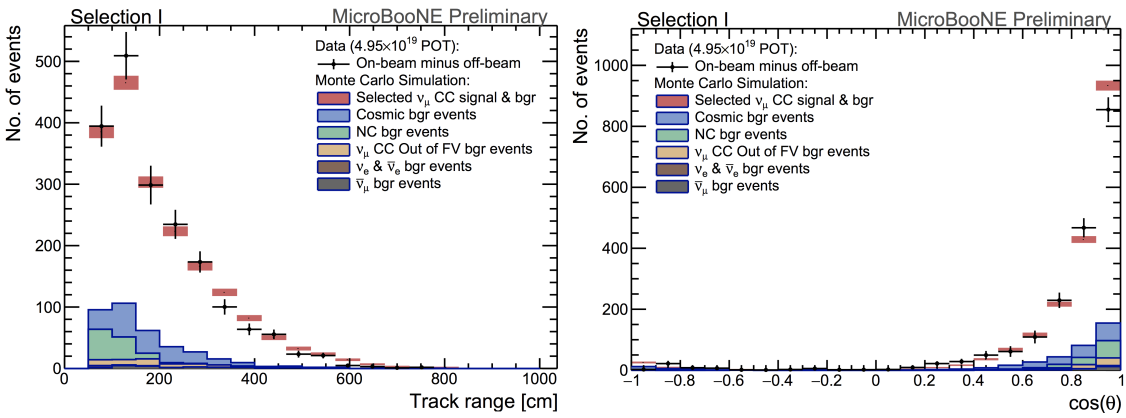


Figure 3.4: Kinematic distributions for the track range (left) and track cos($\theta$) (right) from Selection I. For events with multiplicity$\geq$2, the longest track is used. Error bars are statistical only. Figures from Ref. [74].

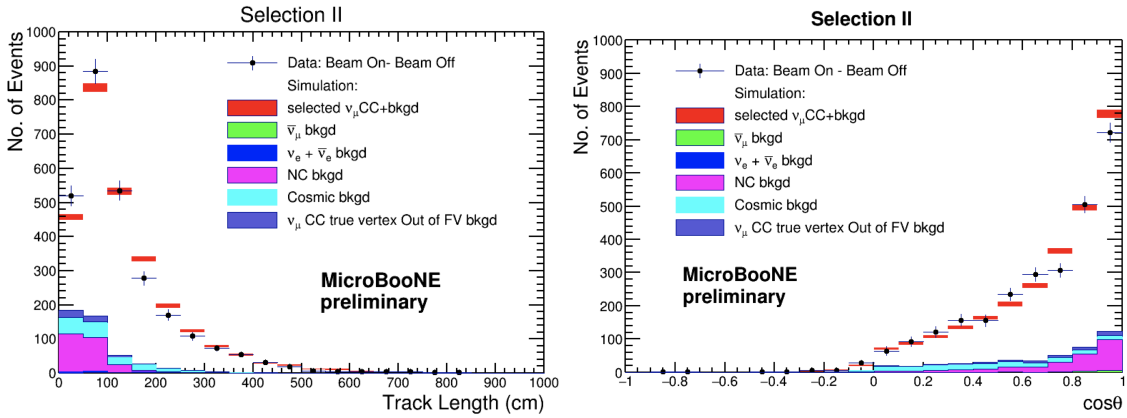


Figure 3.5: Kinematic distributions for the track length (left) and track cos($\theta$) (right) from Selection II. For events with multiplicity$\geq$2, the longest track is used. Error bars are statistical only. Figures from Ref. [74].

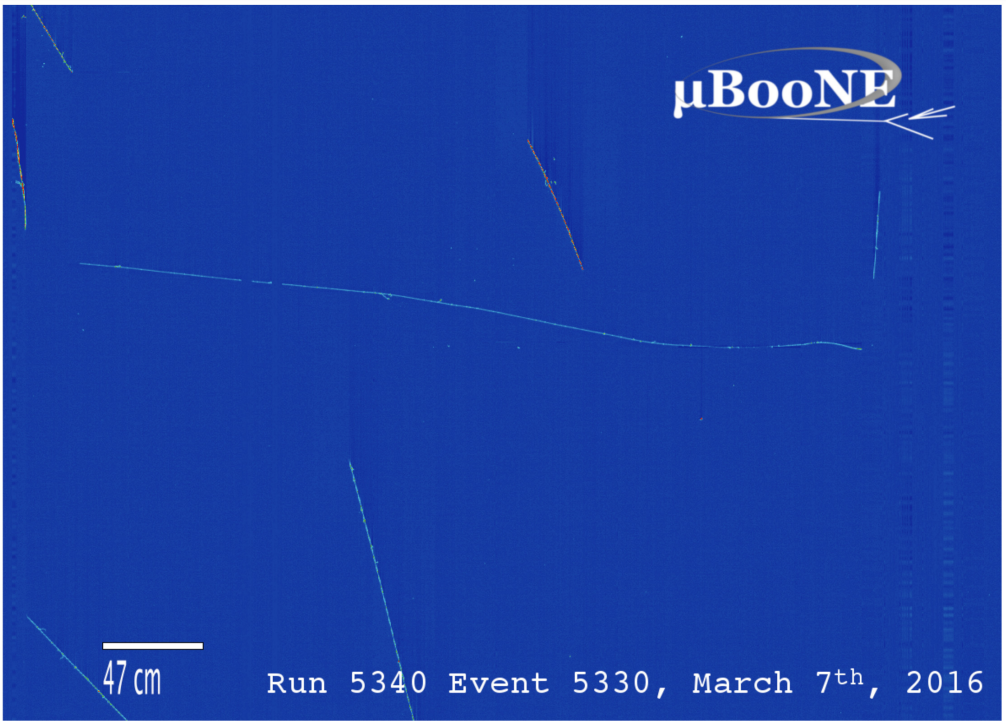


Figure 3.6: A collection plane event display of an example CC event selected with Selection I. The horizontal track is from the selected interaction, while the more vertical tracks are identified as cosmics. Figure from Ref. [74].

# Chapter 4

# CC Inclusive Selection

This chapter outlines the inclusive selection of $\nu_\mu$ CC events. This is not my own work, but rather is primarily the work of Dr. Marco Del Tutto, as well as various other MicroBooNE collaborators. This selection is used as a first step for the CC1$\pi^+$ analysis described in the following chapters, and as such I summarise it here for completeness.

Section 4.1 describes cuts related to matching flashes to other reconstructed objects. Section 4.2 explains how muon candidates are selected. Section 4.3 discusses several cuts aimed at ensuring reconstructed track quality. Section 4.4 describes a fiducial volume cut. Finally, an overview of the performance of the selection is given in Section 4.5.

## 4.1 Flash Matching

The first step of the selection is to identify events where a neutrino interaction has occurred. To do this, it is required that an event has a reconstructed flash with at least 50 PE during a neutrino beam spill. A spill is 1.6$\mu$s long, but due to small per-event timing variations, the window used for this cut is extended by 0.1$\mu$s on either side, for a total 1.8$\mu$s window.

In the reconstruction stage (see Section 2.4), each flash will have been matched to zero or one Pandora reconstructed neutrino candidates. It is possible but unlikely that two or more neutrino interactions truly occur during the same event, so it is reasonable to neglect this case. The flash matching is done by first simulating the flash response for each neutrino candidate interaction. The hypothesis flash is compared to the measured flash, in terms of the PE count on each PMT. Figure 4.1 illustrates this for an example MC event. The candidate neutrino whose hypothesis flash best matches the measured flash is selected for further downstream analysis.

Two additional selection cuts are applied to the flash matching. In both cases, the positions of the hypothesis and measured flashes are compared, to ensure that

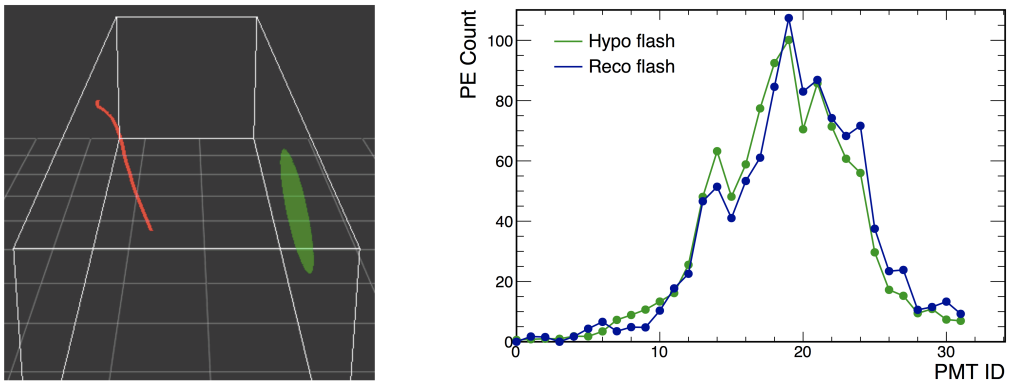


Figure 4.1: Flash matching for an example MC event. On the left, a reconstructed muon from a neutrino interaction (red) and the reconstructed flash (green) are shown within the TPC (white border). The right plot shows the PE count on each PMT for the reconstructed flash (blue) and the hypothesis flash (green). In this case, they match well. Figures from Ref. [76].

they are close. Specifically, it is required that the difference in x position satisfies $-100 \leq x_{\text{hypo}} - x_{\text{meas}} \leq 50$ cm and the difference in z position satisfies $-75 \leq z_{\text{hypo}} - z_{\text{meas}} \leq 75$ cm, where $x_{\text{hypo}}$ and $z_{\text{hypo}}$ are the hypothesis flash x and z positions, respectively, and $x_{\text{meas}}$ and $z_{\text{meas}}$ are the measured flash x and z positions, respectively. Figure 4.2 shows the distributions of these differences for both MC and data.

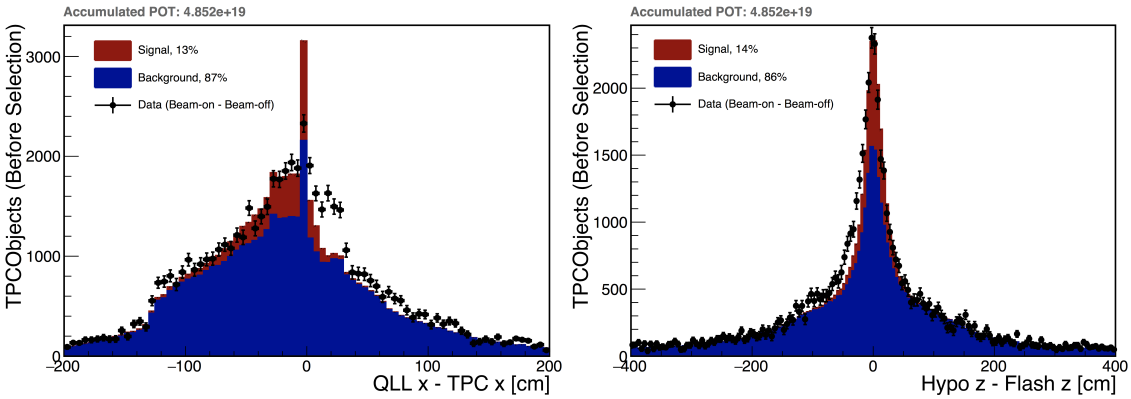


Figure 4.2: Distributions of the differences between the positions of the hypothesis and measured flashes, in the x-direction (left) and z-direction (right). Figures from Ref. [76].

## 4.2 Muon Candidate Selection

Having now selected neutrino-induced interactions, it remains to select specifically CC interactions. Different types of CC interactions will result in different numbers and types of final state particles, but all are characterised by the presence of a muon. In most cases, the muon track will be the longest. Muons can also be well

separated from protons using the tracks' dQ/dx information. Figure 4.3 shows the distribution of track length versus truncated mean dQ/dx for simulated muons and protons. A machine learning algorithm called a Support Vector Machine is used to find a decision boundary between the two particle types. The longest track that is also classified here as muon-like is selected as the muon candidate.

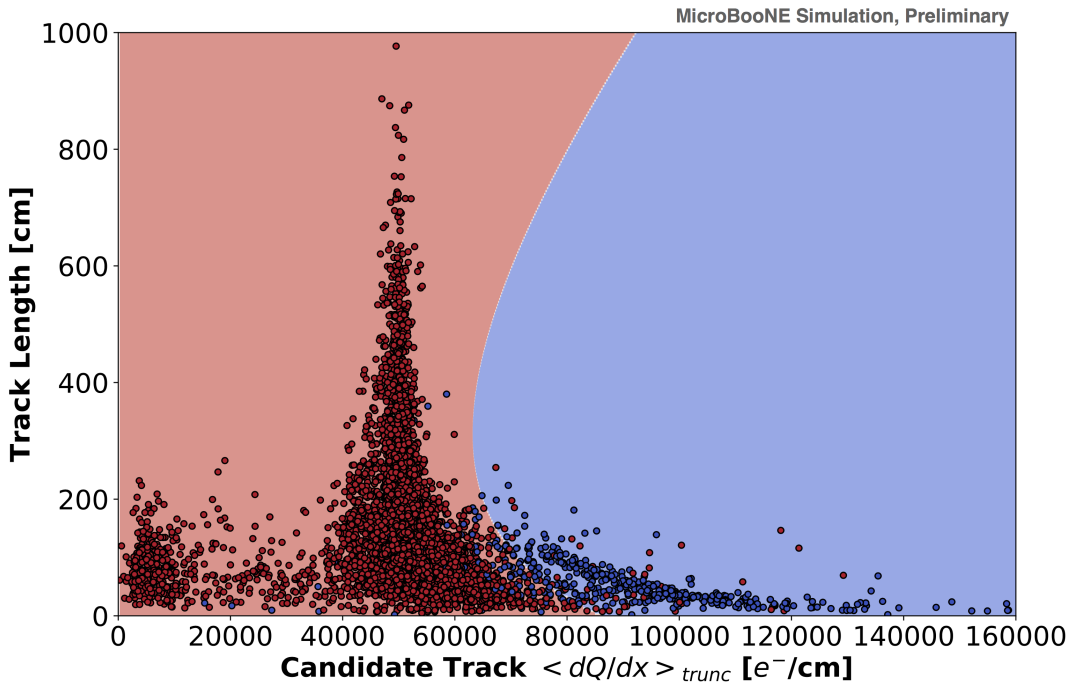


Figure 4.3: Distribution of track length versus truncated mean dQ/dx for simulated muons (red dots) and protons (blue dots). A Support Vector Machine algorithm is used to find a decision boundary, shown with the light red and blue regions. Only those in the red region may be considered as muon candidates. Figure from Ref. [76].

## 4.3 Track Quality

The next step is to make sure that the neutrino vertex and muon candidate have been well reconstructed. Incorrect vertex position or track length can affect the muon angle or momentum estimations. This is of particular concern for differential cross section measurements in these variables. Another possible issue is electromagnetic showers that are incorrectly reconstructed as tracks. Several successive cuts on variables related to track quality aim to address these issues.

The first cut considers the distance between the hits and the reconstructed track trajectory of the muon candidates. The trajectory is projected onto the collection plane, and the distance from each collection plane hit to closest point on the trajectory is calculated, which is denoted as its residual $r_i$. For each event, the standard

deviation of the residuals $\sigma_{r_i}$ is then calculated. Misreconstructed showering events will have a greater dispersion of hits around the track, and consequently a greater value of $\sigma_{r_i}$, as shown in the distribution in Figure 4.4. A cut is applied such that selected events must have $\sigma_{r_i} < 2.5$ cm.

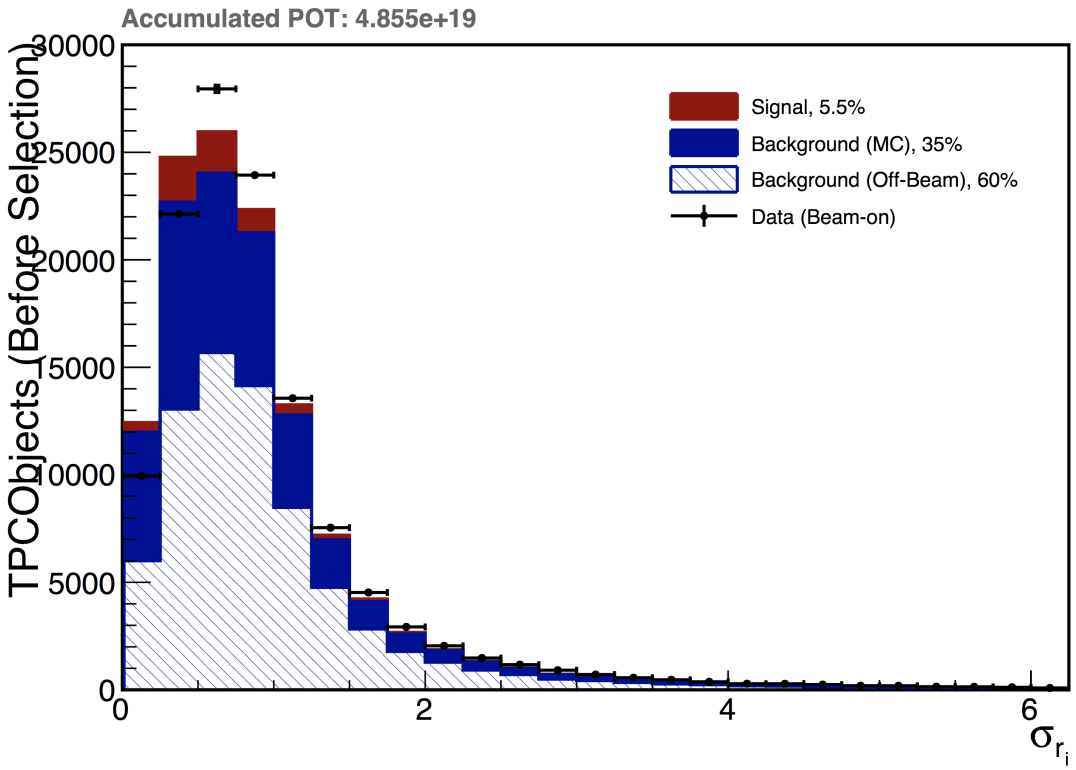


Figure 4.4: Distribution of the standard deviation of the hit residuals for muon candidates, in units of cm. Figure from Ref. [76].

In order to reconstruct a three dimensional track from two dimensional hits, Pandora first constructs intermediate three dimensional objects called space-points by matching hits across the three wire planes. Not every hit will necessarily correspond to a space-point. However, tracks that are better reconstructed will have a higher fraction of used hits. Figure 4.5 shows the distribution of the fraction $f_s$ of collection plane hits that are associated with space-points used in the track fitting. A cut is applied such that selected events must have $f_s > 0.7$.

A final measure of reconstruction quality that is considered involves different ways of measuring momentum. One way is to simply use the track's length. The relationship between range and kinetic energy for muons in liquid argon is known from data from the Particle Data Group [77]. The momentum $p$ is then calculated as $p = \sqrt{K^2 + 2mK}$, where $K$ is the kinetic energy and $m$ is the muon mass. However, this requires that the muon is fully contained in the detector, which is often not the case in MicroBooNE. For this reason, a second technique is used that does not require containment. This method is based on multiple coulomb scattering (MCS), which is a phenomenon wherein charged particles electromagnetically scatter off

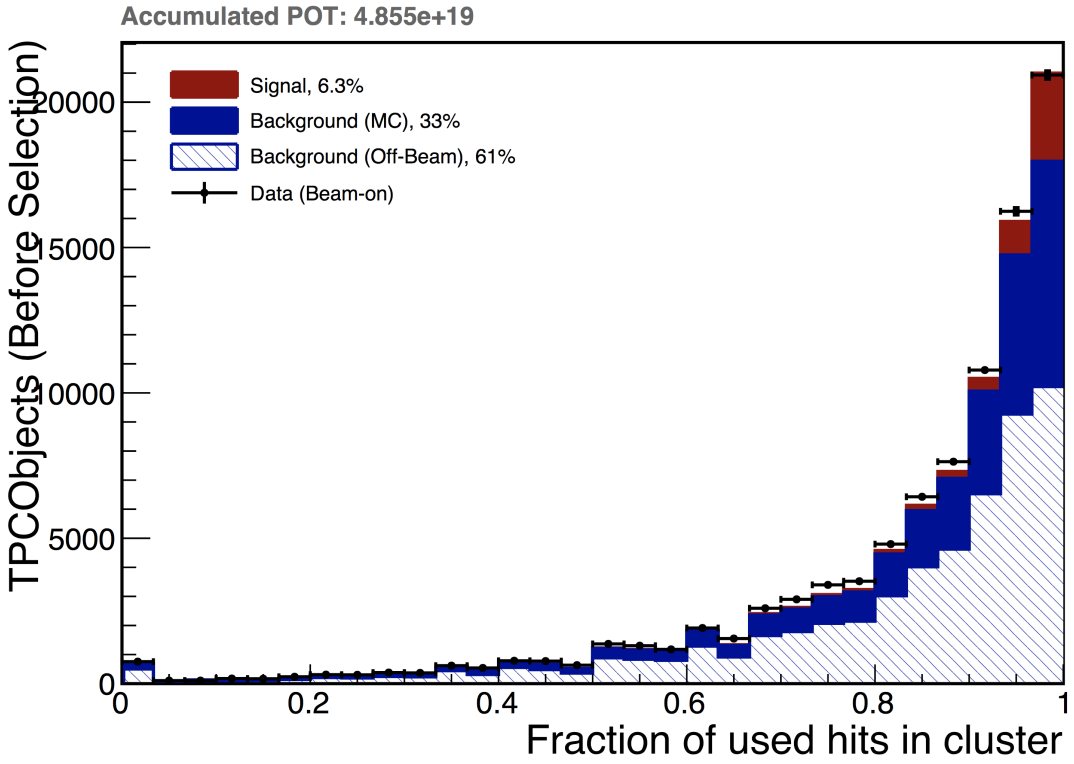


Figure 4.5: Distribution of the fraction of collection plane hits used in the muon candidate track reconstruction. Figure from Ref. [76].

of nuclei in the medium they're travelling through. In the usual model of MCS, the RMS of the scattering angle is dependent on the particle's momentum [78, 79]. MicroBooNE uses a variation of this model that is specifically tuned for LAr [80].

Figure 4.6a shows a comparison of these two methods for contained tracks. For most particles, the two methods closely agree. However, there are a number of off-diagonal points. These correspond to cases where the full length of the track is not reconstructed, leading the length-based method to under-estimate the muon momentum, while the MCS method is still able to estimate it well. Figure 4.6b shows the distribution of the differences between these two methods. In order to eliminate these poorly reconstructed tracks, a cut is applied such that the two methods must agree within 0.2 GeV for selected events.

## 4.4 Fiducial Volume

A final selection cut defines a fiducial volume (FV), pictured in Figure 4.7, in order to mitigate issues in certain areas of the MicroBooNE detector. In the drift direction (x-axis), 12 cm are removed from either side of the TPC faces. In the vertical direction (y-axis), a 35 cm gap from the TPC faces is excluded in order to account for CR background interactions with misplaced start or end points, which can be caused either by reconstruction issues or by the space charge effect (SCE). In the

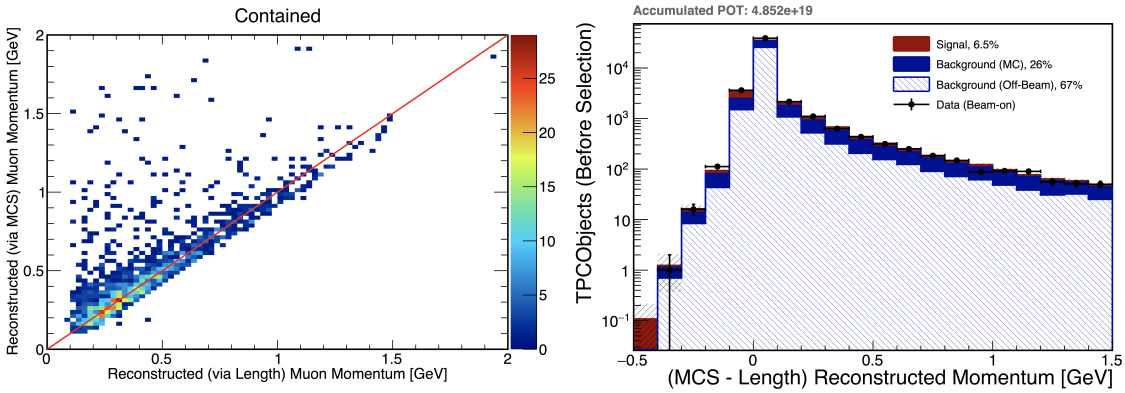


(a) (b)

Figure 4.6: (a) The reconstructed momentum for contained muons, as estimated with the MCS method versus the length-based method. (b) The difference between these two methods. Figures from Ref. [76].

beam direction (z-axis), the FV is 25 cm from the front TPC face and 85 cm from the back face, in order to exclude muons that interact in the very end of the detector and do not leave a substantial enough track before exiting. An additional 100 cm region is removed due to a large number of dead collection plane wires there. A cut is applied such that the reconstructed neutrino vertex position of selected events must be within this FV.

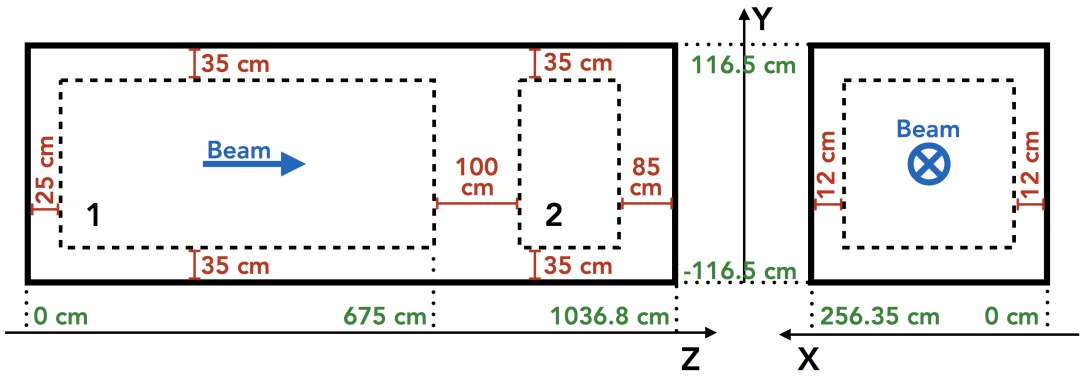


Figure 4.7: The fiducial volume used in the analysis. The solid black line represents the boundaries of the TPC, while the dashed lines show the FV. Figure from Ref. [76].

## 4.5 Selection Performance

The performance of the event selection can be evaluated by looking at its efficiency

$$\epsilon = \frac{\text{Selected CC signal events}}{\text{Generated CC signal events}} \tag{4.1}$$

and purity

$$\rho = \frac{\text{Selected CC signal events}}{\text{All selected events}}. \tag{4.2}$$

Overall, the efficiency of the selection is 57.2% and the purity is 50.4%. The main backgrounds are from CR only events, from events where a neutrino interaction is present but a CR in the event is selected instead, and from neutrino interactions outside of the FV.

It is also important to consider the efficiency as a function of various kinematic variables, to ensure that the phase space has not been inadvertently shaped. Plots and detailed discussion are available in Ref. [76], but I summarise here briefly. The efficiency in most variables is found to be mostly flat, with the main exception being the true muon azimuthal angle $\phi$ (around the beam axis). The cosmic removal stage of the event reconstruction causes there to be lower efficiency near $\phi \approx \pm\pi/2$ rad, corresponding to tracks travelling vertically upward or downward.

Figure 4.8 shows the efficiency as a function of true neutrino energy, for different GENIE interaction types. The distributions are very similar, showing that the selection really is inclusive. They are also flat across most of the range, falling off only at low neutrino energy. Distributions of event rates in true kinematic variables before and after the selection and split by interaction type also show minimal shaping. All of these facts make this selection well suited to serve as a starting basis for further exclusive selections, as no significant bias has been introduced.

Although not directly relevant to the use of this selection as a pre-selection for the CC1$\pi^+$ analysis, the cross section results stemming from this selection are worthy of note. The details of uncertainty estimation and cross section extraction are beyond the scope of this work, but the resulting differential cross sections in muon momentum and in the cosine of the polar angle $\theta$ between the muon and beam axis are shown in Figure 4.9. A double differential result in these variables has also been published [81].

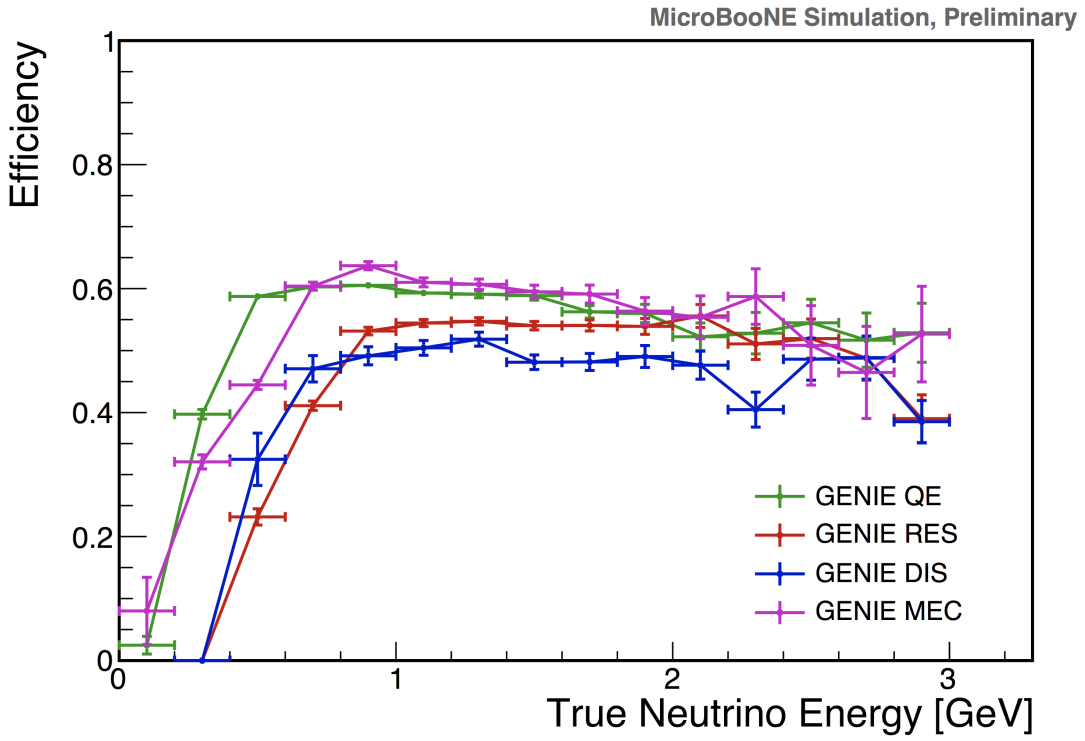


Figure 4.8: CC inclusive selection efficiency as a function of true neutrino energy, for different GENIE interaction types. CC coherent interactions contribute negligibly and are not shown here. Error bars are statistical only. Figure from Ref. [76].

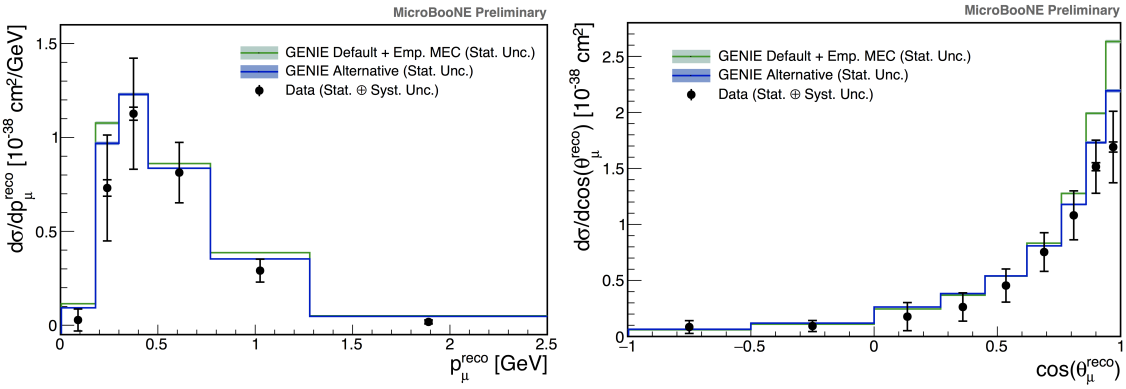


Figure 4.9: The $\nu_\mu$ CC inclusive cross section on argon per nucleon, as a function of the reconstructed muon momentum (left) and $\cos(\theta)$ (right). Figures from Ref. [76].

# Chapter 5

# CC1$\pi^+$ Selection

This chapter outlines the selection of CC1$\pi^+$ events. The CC inclusive selection described in the previous chapter is used as a pre-filter for this selection. The remainder of the selection, as described in this chapter, is my own original work, with one exception. The log-likelihood particle ID algorithm described in Section 5.4.4 is the work of Dr. Kirsty Duffy and Dr. Adam Lister.

A precise signal definition and description of backgrounds is given in Section 5.1. Section 5.2 describes the process of modifying Pandora's functionality in order to give a more suitable starting sample. Similarly, Section 5.3 describes two pre-selection cuts aimed at addressing reconstruction issues, in order to improve the sample quality.

Section 5.4 describes the boosted decision tree (BDT) that is the principal part of the selection. Different boosting algorithms are explored in Section 5.4.1, a description of the training sample is given in Section 5.4.2, and explanations of each of the input variables are given in Sections 5.4.3 - 5.4.5. The results from the BDT are presented in Section 5.4.6.

Sections 5.5 and 5.6 describe two further selection cuts on the MIP candidates identified by the BDT, one on opening angle and one on containment. Section 5.7 discusses initial results of muon-pion separation, labelling the two MIP candidates as a muon candidate and a pion candidate. Finally, overall results of the event selection are shown in Section 5.8.

## 5.1 Signal Definition and Backgrounds

I define the CC1$\pi^+$ signal as an interaction containing the final state particles:

- exactly one muon
- exactly one pion

- no other mesons
- any number of nucleons or nuclei
- Due to a reconstruction issue, I also require that direct daughters of the neutrino (so the muon, pion, and possibly some nucleons or nuclei) do not have a polar angle $\theta$ of $\pi/2 \pm 0.2$ rad. This is discussed in detail in Section 5.3.2.

Note that the fiducial volume I use in this analysis is the same as that used in the preceding CC inclusive selection (see Section 4.4). Figure 5.1 illustrates this signal definition with a number of example interactions, labeled with whether they would be counted as signal or background events in this analysis.

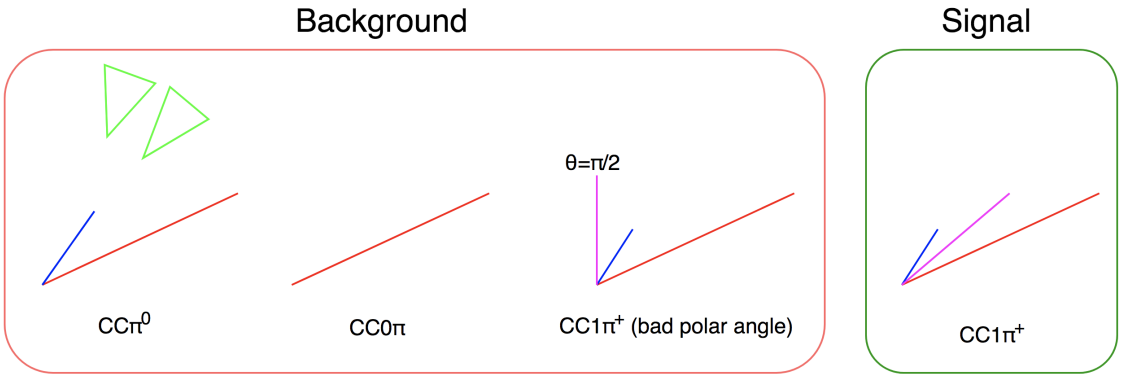


Figure 5.1: Examples of background (left) and signal (right) events. A red line represents a muon, a blue line represents a proton, a green triangle represents an electromagnetic shower, and a magenta line represents a charged pion.

Some figures in this chapter contain stacked histograms of the various topologies that were selected. Brief descriptions of each background category are given below.

**Beam-off** Events where no neutrino interaction is present, but a cosmic interaction occurs during the event window and is selected. The rate of this background is measured from data taken while the neutrino beam is turned off.

**Cosmic** Events where a neutrino interaction is present, but a cosmic interaction is selected instead.

**Mixed** Events where both a neutrino and cosmic interaction are present, and are incorrectly reconstructed as a single interaction that is then selected.

**Dirt** Events with interactions that occur outside of the cryostat. These are simulated in a separate "dirt" sample.

**Out of FV** Events with a true neutrino vertex outside of the fiducial volume, but a reconstructed vertex inside it. These occur primarily due to the space charge effect.

**Multi-$\nu$** In the vast majority of cases, no more than a single neutrino interaction is present in an event. However, rarely, it is possible for there to be multiple

neutrino interactions. It is estimated that 1 in 600 events in MicroBooNE will contain a neutrino interaction, meaning the chance of an event with two neutrino interactions is roughly 1 in $600^2 = 720000$, corresponding to a very low number of expected occurrences in the dataset used in this analysis. Therefore, rather than expend effort to apply special handling for this case, any such multi-neutrino event is simply classified entirely as background.

**$\nu_\mu$ CC0$\pi$** Events with no charged or neutral pions. These constitute the largest background for this analysis.

**$\nu_\mu$ CC1$\pi^+$Bad Angle** Events that would otherwise be signal, but where one or more of the direct daughters of the neutrino have a polar angle $\theta$ of $\pi/2 \pm 0.2$ rad, which causes a reconstruction issue. See Section 5.3.2 for further details.

**$\nu_\mu$ CC1$\pi^-$** Wrong sign single pion production events, caused by a small flux of $\overline{\nu}_\mu$ in the neutrino beam. Note that unlike many experiments, MicroBooNE does not have a magnetic field with which to identify the sign of charged particles, so this background cannot be cleanly rejected.

**$\nu_\mu$ CC1$\pi^0$** Single neutral pion production.

**$\nu_\mu$ CC >1$\pi$** Events with more than one final state pion of any charge.

**$\nu_\mu$ CC Other** All other $\nu_\mu$ charged current events.

**$\nu_e$ CC** All $\nu_e$ and $\overline{\nu}_e$ charged current events, caused by small fluxes of each present in the neutrino beam.

**NC** All neutral current events.

## 5.2 Track Refitting

Pandora classifies each non-neutrino PFP as either track-like or shower-like, and constructs a corresponding object based on this. I expect CC1$\pi^+$ events to have at least two tracks: the muon and the pion. However, as shown in Figure 5.2, the fraction of muons, pions, and also protons that are classified as tracks is found to be lower than ideal. Specifically, overall, 7.7% of muons, 30.3% of pions, and 20.5% of protons were classified as showers in events that pass the CC inclusive pre-selection.

In order to overcome this issue, I added functionality to Pandora to optionally reconstruct all non-neutrino PFPs as tracks, regardless of Pandora's classification. I do this in such a way that it does not modify the CC inclusive pre-selection; it is effectively applied afterwards. This gives me a workable starting basis for this analysis, with the ability to cut out true showers with later selection cuts.

Figure 5.3 shows the distributions of track length and polar angle $\theta$ between the track and the beam axis for the longest track in each event that is a direct daughter of the neutrino candidate. Corresponding plots are shown for each stage of the selection, as an aid in showing the effect of each cut.

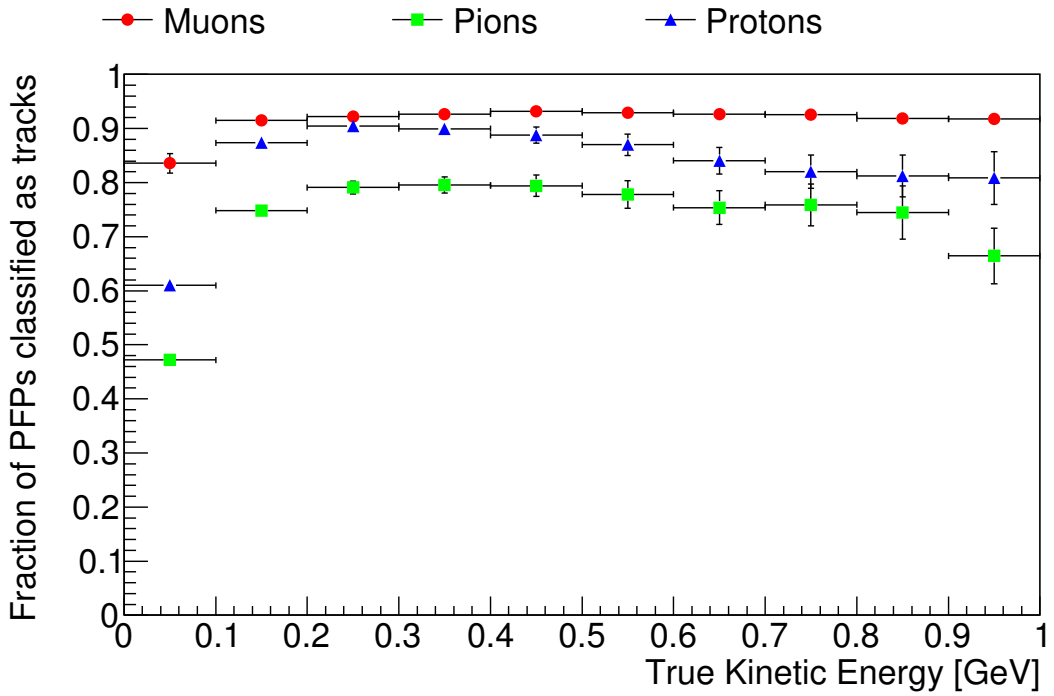


Figure 5.2: The fraction of muons (red circle), pions (green square), and protons (blue triangle) in events passing the CC inclusive pre-selection that are classified by Pandora as tracks, as a function of true kinetic energy. I expect all of these particles to be classified as tracks, and so choose not to use this classification system.

## 5.3 Quality Cuts

Before applying selection cuts to specifically identify signal events, quality cuts need to be applied. These are designed primarily to remove events that are poorly reconstructed. Section 5.3.1 describes a cut on the distance between track starting points and the neutrino vertex, while Section 5.3.2 describes a cut on the polar angle of tracks.

### 5.3.1 Vertex-track start distance

I expect that direct daughters of the neutrino in CC1$\pi^+$ events will start near the reconstructed neutrino vertex. The distribution of these distances is shown in Figure 5.4. PFPs that start farther away are more likely to be true showers or to be poorly reconstructed. I therefore require that all direct daughter PFPs start within 5 cm of the reconstructed neutrino vertex. Figure 5.5 shows the distributions of track length and polar angle $\theta$ between the track and the beam axis for the longest track in each event that is a direct daughter of the neutrino candidate, after this cut is applied.

This distance may seem high, given that the wire pitch in MicroBooNE is 3 mm. Figure 5.6 shows the efficiency, purity, and efficiency times purity of the selection

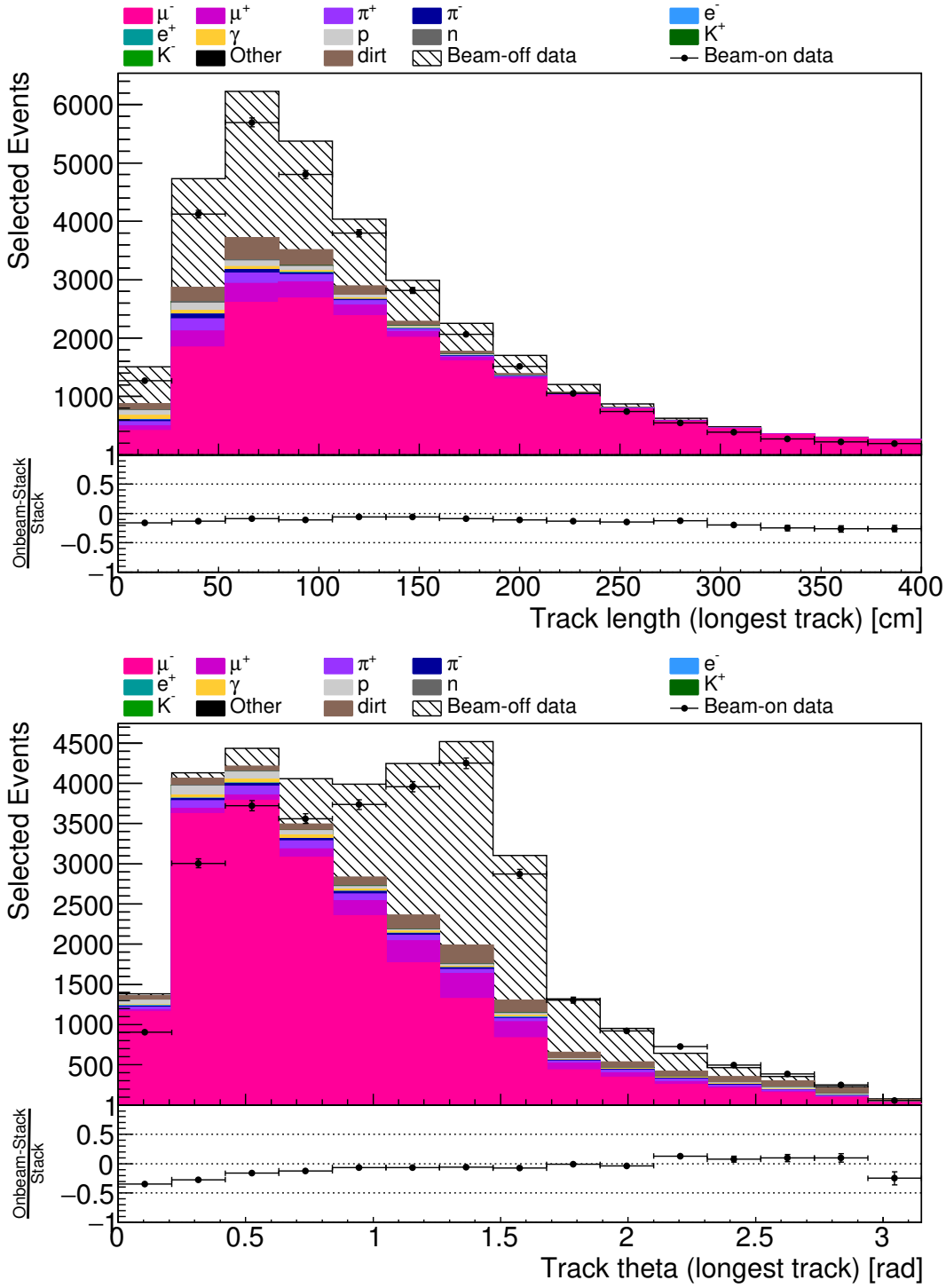


Figure 5.3: The distributions of track length (top) and polar angle $\theta$ between the track and the beam axis (bottom) for the longest track in each event that is a direct daughter of the neutrino candidate, after track refitting.

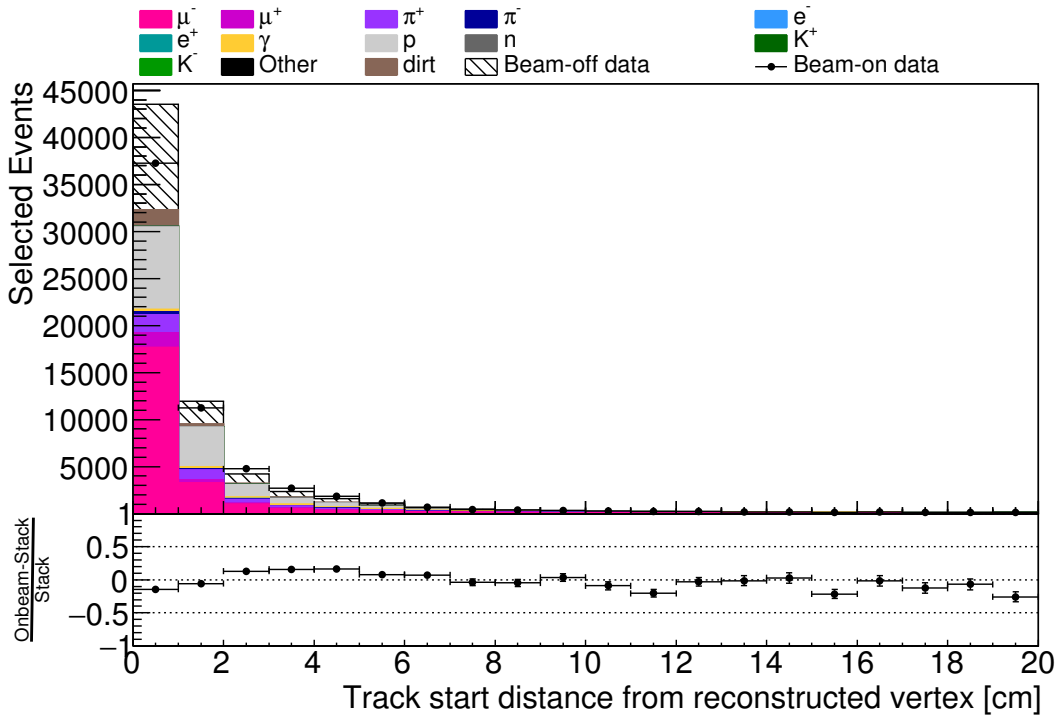


Figure 5.4: Distribution of the distance between each track's starting point and the reconstructed neutrino vertex.

as a function of the cut value for the vertex-track start distance. Maximising for efficiency times purity would actually increase the cut distance to about 10 cm. This cut cannot be made tighter with current reconstruction performance without further reducing efficiency.

One particular failure mode I identified involves a single true muon reconstructed as two separate tracks, with the reconstructed neutrino vertex placed in the wrong position. An event display showing a 2D projection of an example simulated event is shown in Figure 5.7. Despite this misreconstruction, both tracks are still considered to be direct daughters of the neutrino by Pandora. Pandora is a complicated, multi-algorithm pattern recognition framework (see Section 2.4.2 for description), so it is not straightforward to assess why these misreconstructions occur and further study is necessary. Nonetheless, since one of these tracks will start far away from the reconstructed neutrino vertex, placing a cut on this distance also eliminates these poorly reconstructed events, which is sufficient for this analysis.

### 5.3.2 Polar Angle

In order to convert the measured change in charge per unit length along a track dQ/dx into its energy loss per unit length dE/dx, one needs to calibrate and correct for various issues with the wire planes. At the time of this analysis, only the calibration for the collection plane is found to be reliable, and so for these purposes

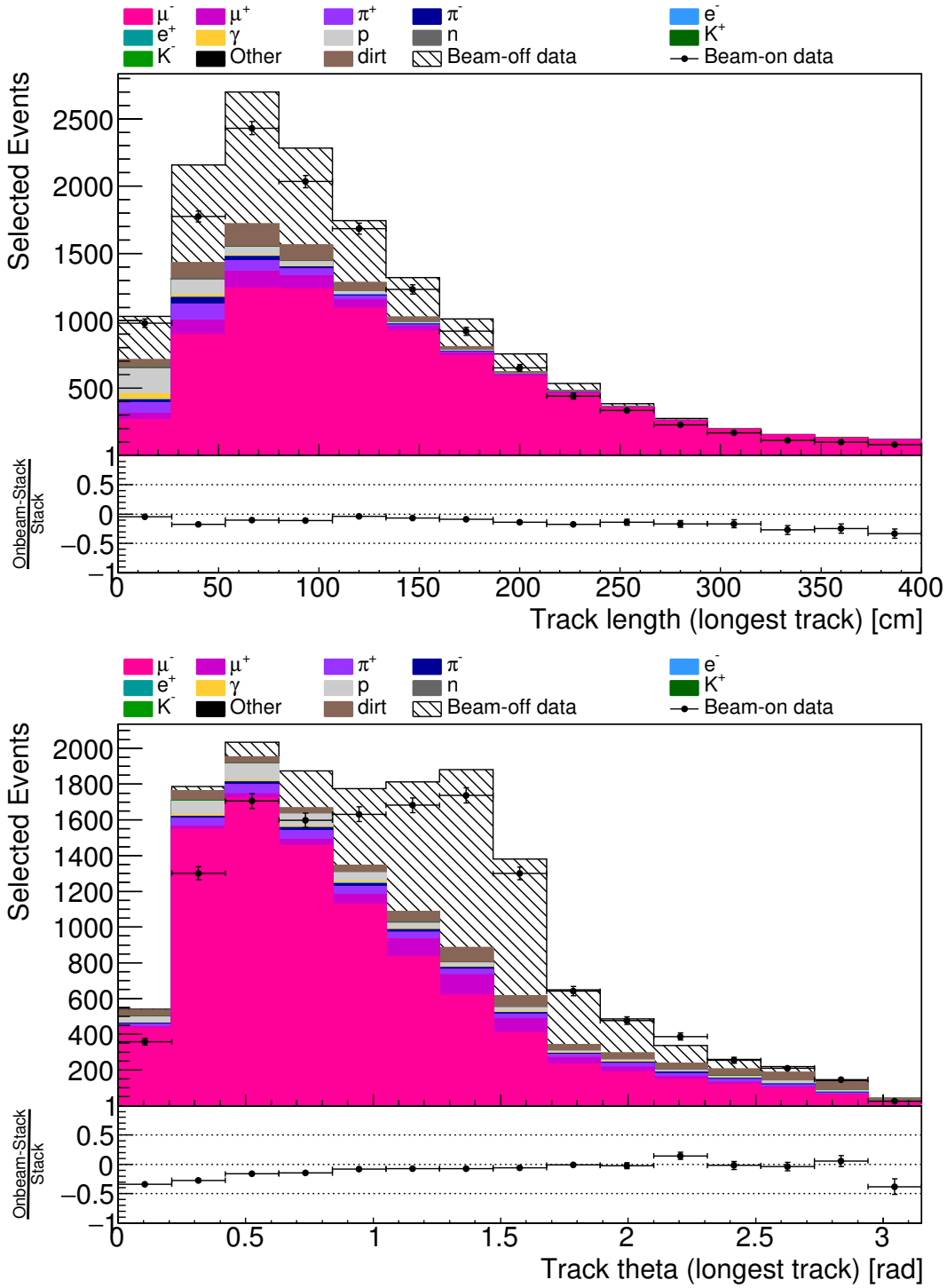


Figure 5.5: The distributions of track length (top) and polar angle $\theta$ between the track and the beam axis (bottom) for the longest track in each event that is a direct daughter of the neutrino candidate, after the cut on vertex-track start distance is applied.

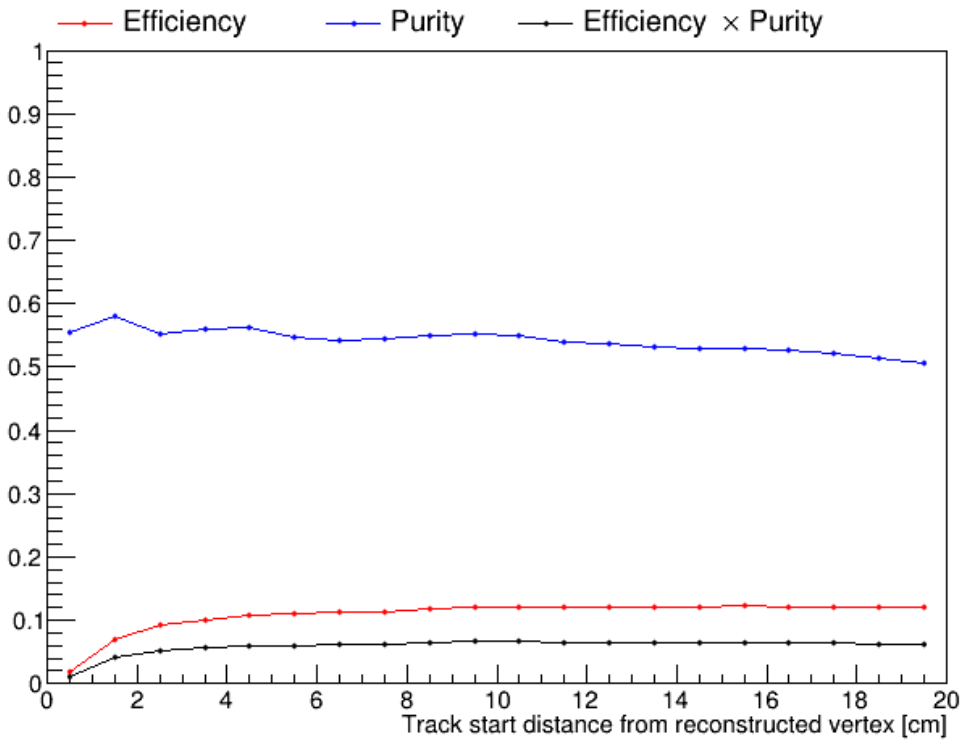


Figure 5.6: Efficiency (red), purity (blue), and efficiency times purity (black) of the selection, as a function of the cut value for vertex-track start distance.

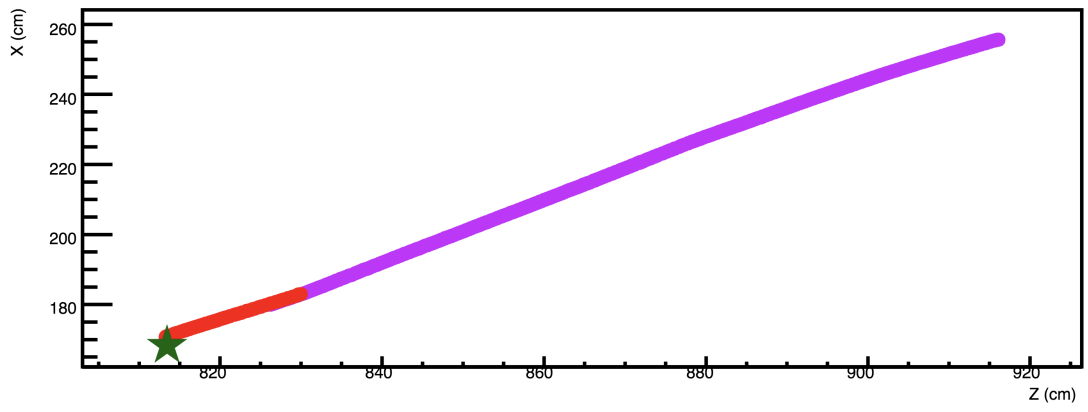


Figure 5.7: Event display of a simulated event where a single true muon has been reconstructed as two tracks (one shown in red, the other in purple). Both tracks are reconstructed as direct daughters of the reconstructed neutrino vertex (green star). Note that this is a 2D projection of the event in the x-z plane.

I do not use the induction planes.

The angles and coordinate system used in MicroBooNE are shown in Figure 5.8. The wire planes sit at the anode, with the collection plane wires in the vertical direction (polar angle $\theta = \pi/2$). The distribution of $\theta$ for tracks that are direct neutrino daughters is shown in Figure 5.9. Since I am only able to use the collection plane, an angular complication arises for tracks that are parallel to the collection plane. All of the charge from these tracks will essentially arrive on one wire, making it very difficult to properly measure the dQ/dx values. In order to account for this, I must apply a selection cut to remove these poorly measured tracks. Specifically, I require that direct daughters of the neutrino must not have values of $\theta$ between $\pi/2 \pm 0.2$ rad. Figure 5.10 shows the distributions of track length and $\theta$ for the longest track in each event that is a direct daughter of the neutrino candidate, after this cut is applied.

Since the selection will have zero efficiency in this area of phase space, I need to adjust my signal definition. Any resulting cross section measurement will necessarily be biased by this exclusion if I claim to have tried to measure these events. I therefore remove these events from my signal definition: events in which the true muon or pion have values of $\theta$ between $\pi/2 \pm 0.2$ rad are excluded from my signal.

## 5.4 Boosted Decision Tree

Decision trees are a simple type of classifier. They take as input a sample of labelled signal and background objects, called the training sample, and a set of variables that one wishes to use for classification. At each node, the sample is split into two parts by finding the classification variable (and cut value for that variable) that best separates the signal and background. This is done successively until each final node is made up mostly or entirely (as configured) of only signal or background events. The phase space of the selection variables is thus split into regions that are classified as signal-like or background-like, which can then be applied to real data.

Unfortunately, individual decision trees are often strongly impacted by fluctuations in the training sample. In order to overcome this, the concept of a single tree can be extended to a "forest" of multiple trees, which combine to form a boosted decision tree (BDT). Events from the training sample are reweighted, and each new set of events produces a decision tree via the same process outlined previously. A final BDT classifier is then created by taking the weighted average of all of the decision trees. This enhances both resiliency to training sample fluctuations and overall performance.

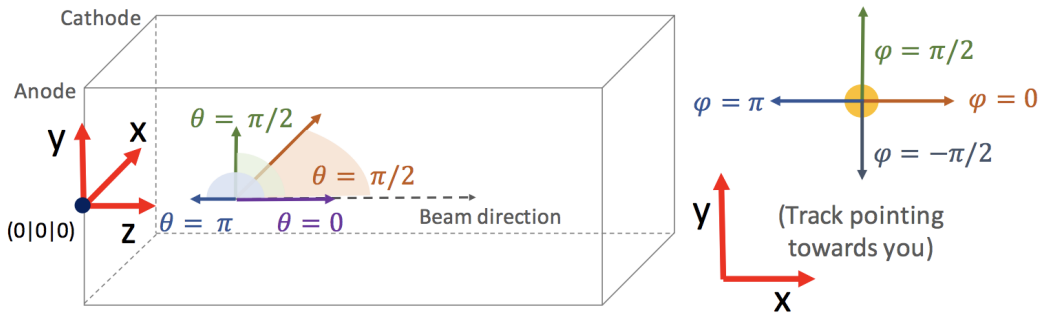


Figure 5.8: Angles and coordinate system used in MicroBooNE. $\theta$ is the polar angle between a track and the beam axis; $\phi$ is the track's azimuthal angle. Figure from Ref. [74].

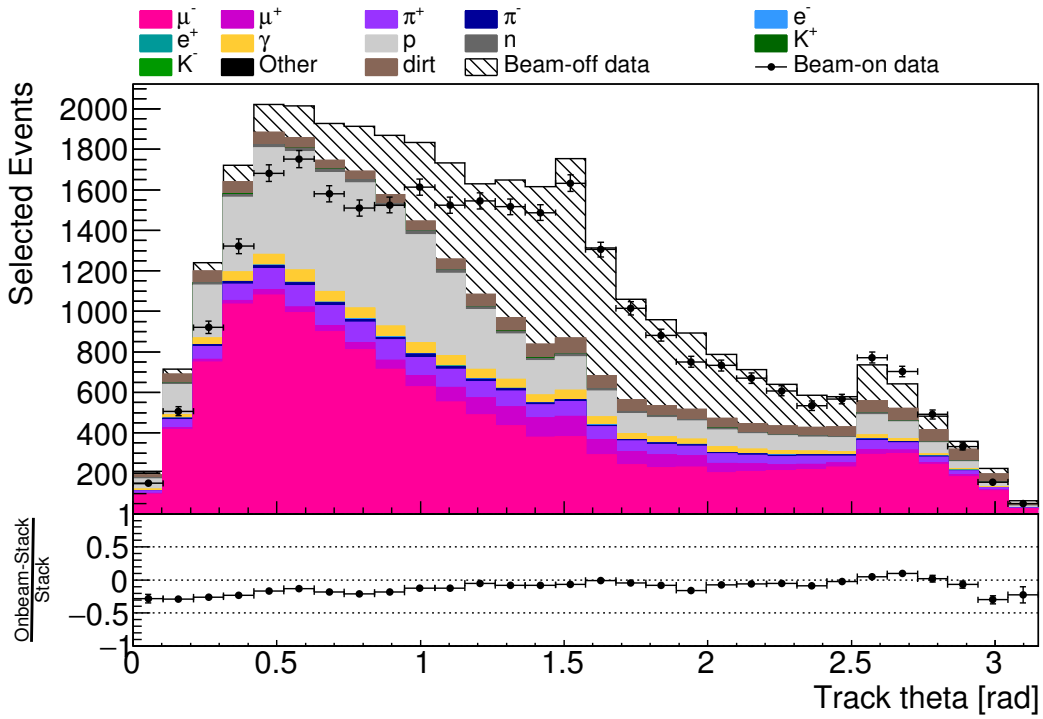


Figure 5.9: Distribution of the polar angle $\theta$ between each direct neutrino daughter track and the beam direction.

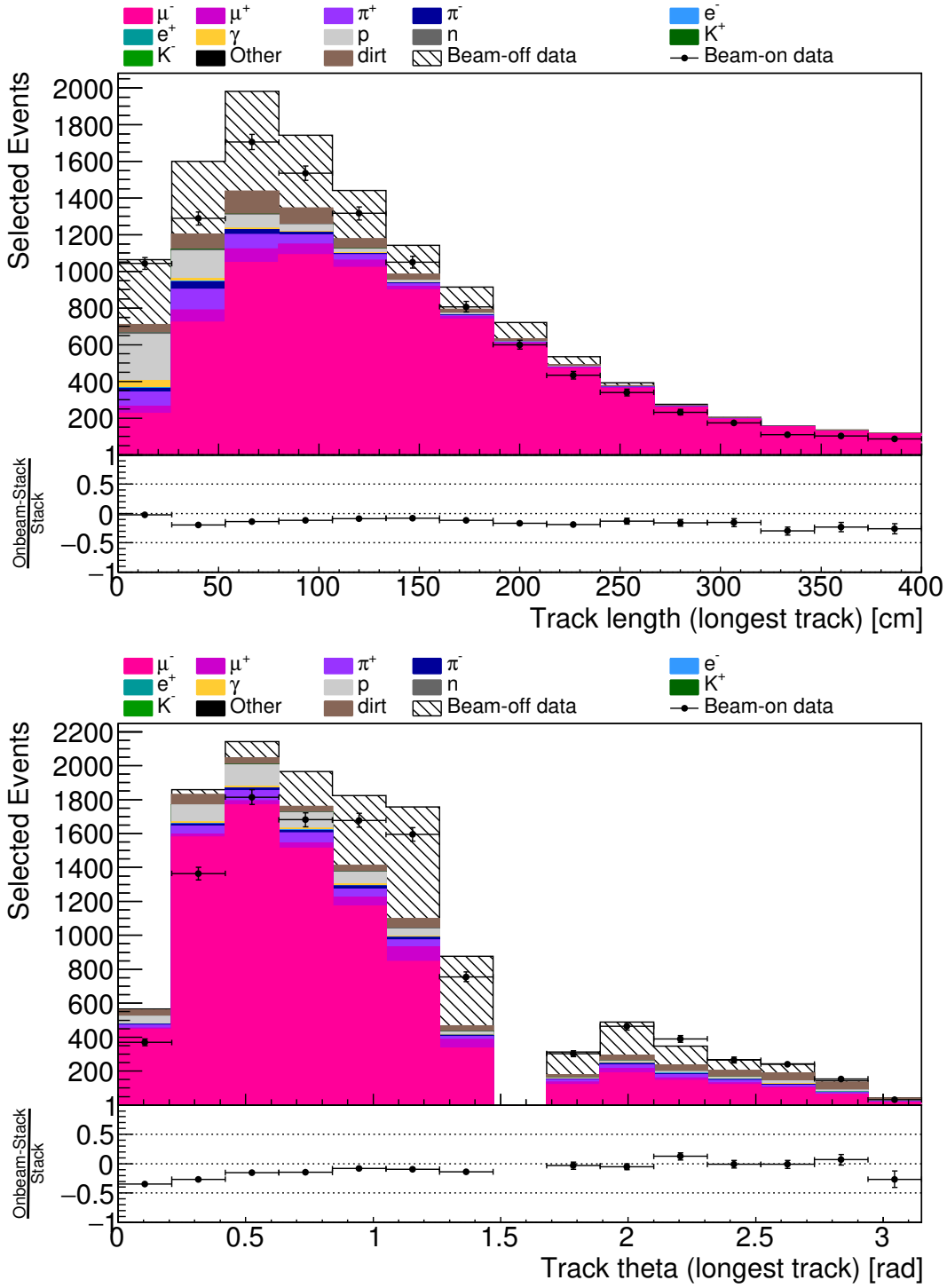


Figure 5.10: The distributions of track length (top) and polar angle $\theta$ (bottom) for the longest track in each event that is a direct daughter of the neutrino candidate, after the cut on $\theta$ is applied.

### 5.4.1 Boosting Algorithms

I produced BDTs using the Toolkit for Multivariate Data Analysis with ROOT (TMVA). A number of different boosting algorithms have been developed, several of which were explored in this analysis. The most commonly used boosting algorithm is known as Adaptive Boosting, or AdaBoost. TMVA also offers Gradient Boosting and Bagging. In addition to these three main boosting algorithms, two additional options were individually tried with AdaBoost: Fisher discriminant classification and preprocessing input variable decorrelation.

A plot of the background rejection versus signal efficiency for each of these BDTs is shown in Figure 5.11. Bagging clearly gives the worse performance, with all other algorithms performing very similarly to one another.

Figure 5.12 shows overtraining checks for each algorithm. The BDT response for the training sample is compared to that of a test sample, for both the signal and background events. Each plot shows these four distributions, as well as the results of TMVA's implementation of the Kolmogorov-Smirnov goodness-of-fit test. Ideally this value should be 0.5; values too far from this may indicate overtraining.

Since all of the non-bagging algorithms give similar performance, from this perspective, any would be a reasonable choice to use. I therefore also look at the shape

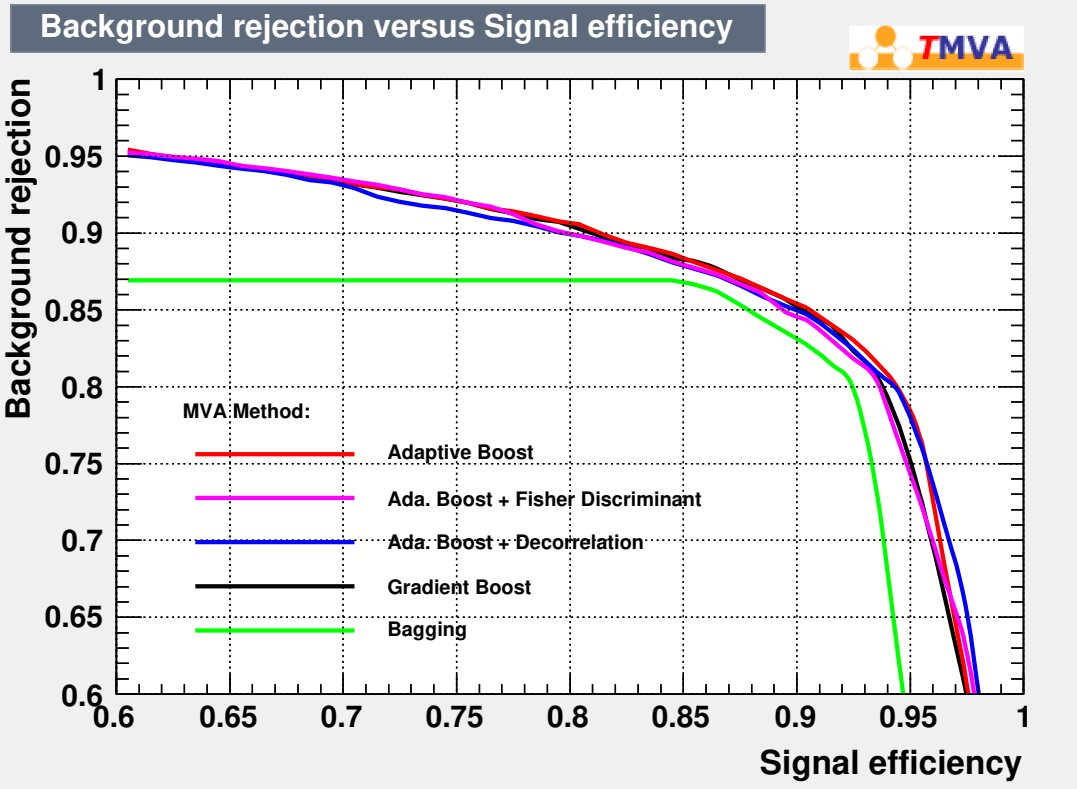


Figure 5.11: Distribution of background rejection versus signal efficiency for each of the five BDT methods tested: adaptive boost, adaptive boost with Fisher discriminant, adaptive boost with decorrelation, gradient boost, and bagging.

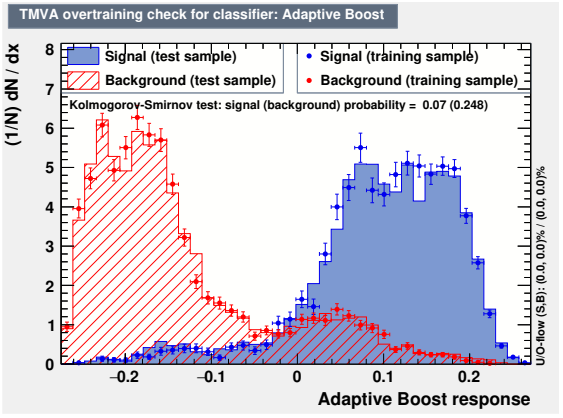


(a) Adaptive Boost

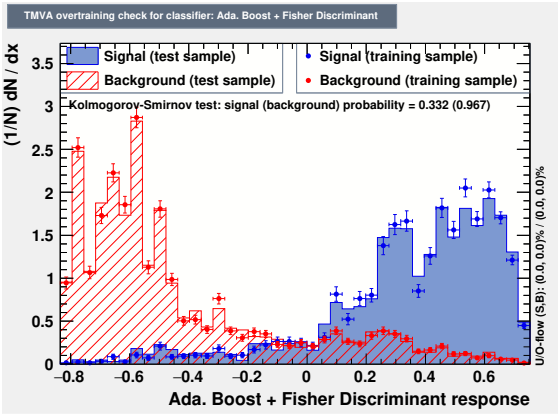


(b) Ada. + Fischer Discr.

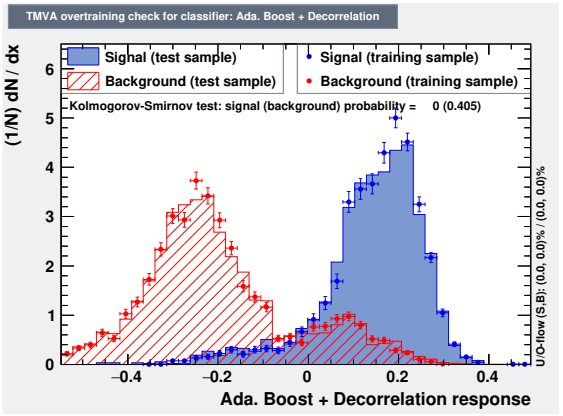


(c) Ada. + Decorrelation

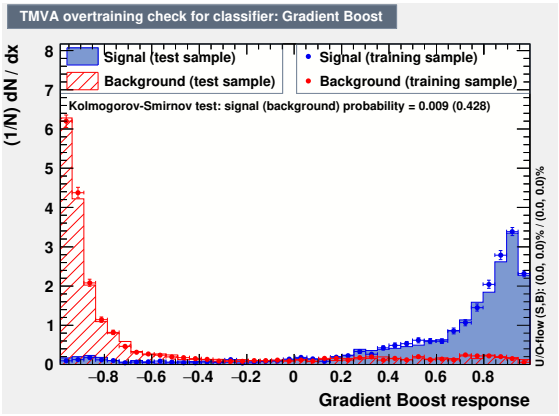


(d) Gradient Boost

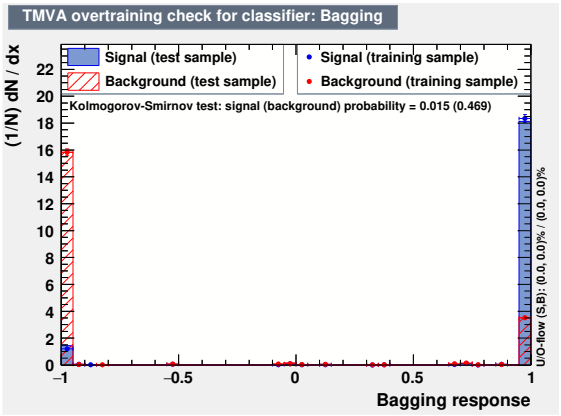


(e) Bagging

Figure 5.12: Overtraining checks for each of the BDT algorithms.

of the BDT response functions. Gradient Boost has the smoothest function and the peaks of the signal and background responses are very separated. I therefore choose Gradient Boost as the algorithm for this analysis moving forward.

### 5.4.2 Input Sample and Weighting

The purpose of the BDT is to separate MIP-like tracks from non-MIP-like tracks, where MIP refers to a minimum ionising particle. In my case, this means that muons and pions are my MIP-like signal sample, and all other tracks are my non-MIP-like background sample. Furthermore, I wish to consider only muons and pions that come from true neutrino interactions to be signal. Cosmic muons, for example, may inhabit a different phase space, and I do not wish to select these tracks.

Unfortunately, this starting point does not produce the desired results. Since there are many types of neutrino interactions that include a muon, and comparatively few that include a pion, the BDT winds up biasing toward identifying muons. Its performance for correctly identifying pions is significantly worse, and thus its overall performance for the CC1$\pi^+$ selection is worse. In order to fix this issue, I split the signal into a muon sample and a pion sample, which are then reweighted in order to effectively train on the same number of muon and pion tracks. This leads to much better overall CC1$\pi^+$ selection performance.

Figure 5.13 shows the distributions of each of the BDT input variables for training sample particles, split into signal and background. Detailed discussions of each of these variables is found in the following sections.

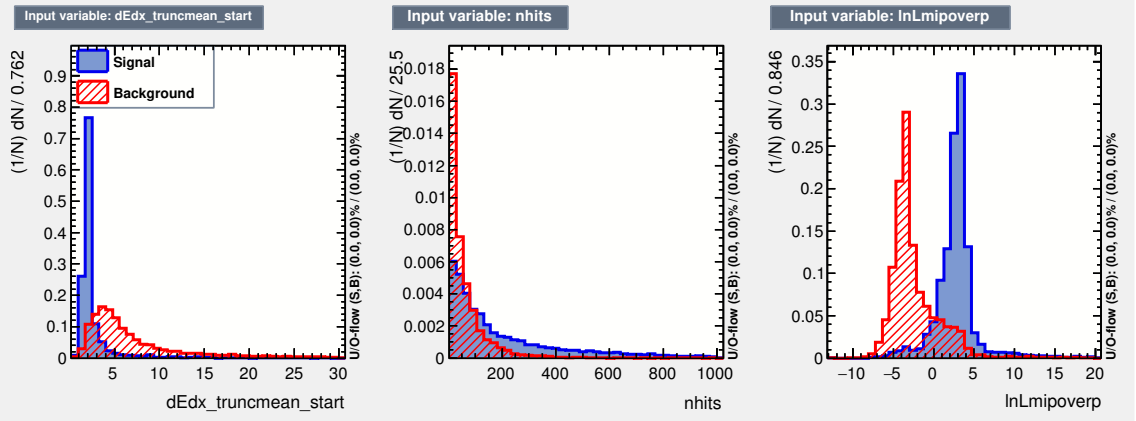


Figure 5.13: Distributions of each BDT input variable for training sample particles, split into signal (solid blue) and background (hatched red). The variables are truncated mean dE/dx (left), number of collection plane hits (centre), and log-likelihood particle ID (right).

### 5.4.3 Truncated Mean dE/dx

The dE/dx profile of a track is one of the main handles I have to determine whether a track is MIP-like or not. This variable looks at the start of the track. The very start of the track often does not have reliable dE/dx measurements due to the presence of other particles at the vertex, and so I skip the first three hits and look at the next third of the hits in the track. I calculate the median and root mean square (RMS) of the hits' dE/dx. I then remove all hits which have a dE/dx value that is not within one standard deviation (as calculated using the RMS) of the median. Finally, I calculate the truncated mean dE/dx by taking the mean of the remaining hits.

Figure 5.14 shows the distribution of these values for all tracks. It can be seen that the peak is broader in data than in MC. This can be attributed primarily to the DIC effect (see Section 2.3.4), which is not included in the version of the simulation used here. Unfortunately, this difference likely does impact the selection. This is discussed further in Sections 7.1 and 8.1.

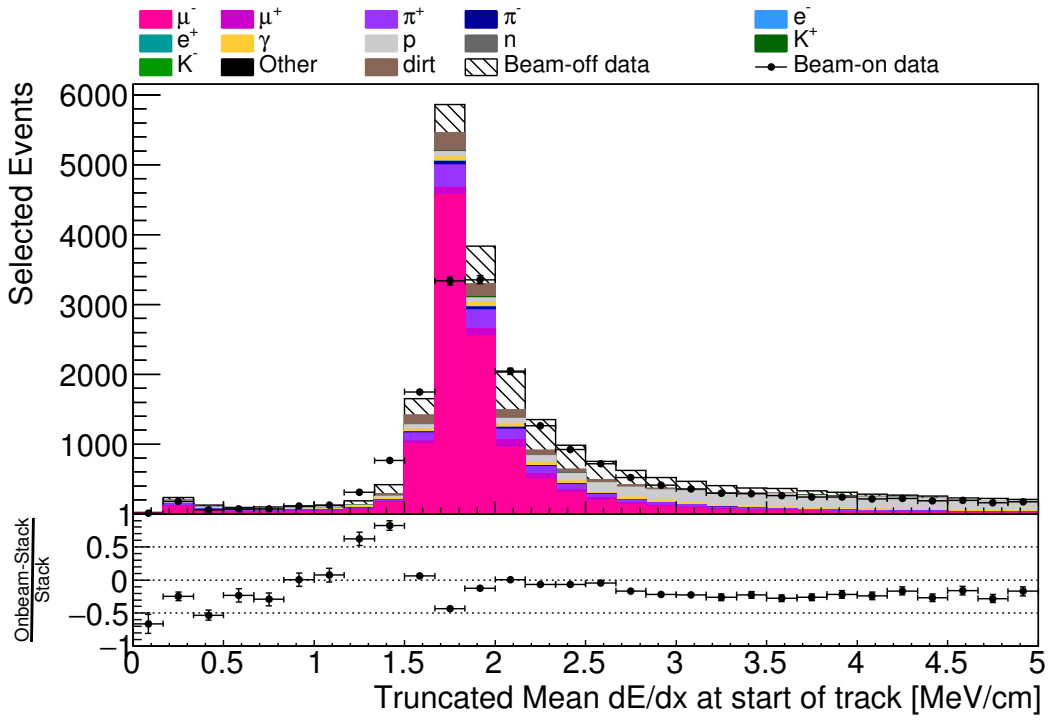


Figure 5.14: Distribution of truncated mean dE/dx values.

### 5.4.4 Log-Likelihood Particle ID

In addition to looking at the dE/dx at the start of a track, it is also useful to consider the dE/dx at the end of a track. Dr. Kirsty Duffy and Dr. Adam Lister developed a Particle ID algorithm based on this information [82]. I was not involved in the

development; the algorithm is not my work, but I describe it below for completeness.

Simulated and real data do not have identical dE/dx distributions, so first a calibration must be performed so that they can be compared. The dE/dx distributions for hits with residual range (that is, distance from the end of the track) of 100-150 cm were examined for each of the wire planes and (for simulation) different particle species. These distributions were found to be well modelled by the combination of a Landau function, corresponding to the ideal energy loss function, and a Gaussian, which combines all unsimulated and poorly simulated detector effects. Once widths are determined for these functions, the mean is determined by looking at the theoretical distribution of dE/dx versus residual range, shown in Figure 5.15. The high energy loss seen at low residual range (that is, near the very end of the track) is a well known phenomenon referred to as a Bragg peak.

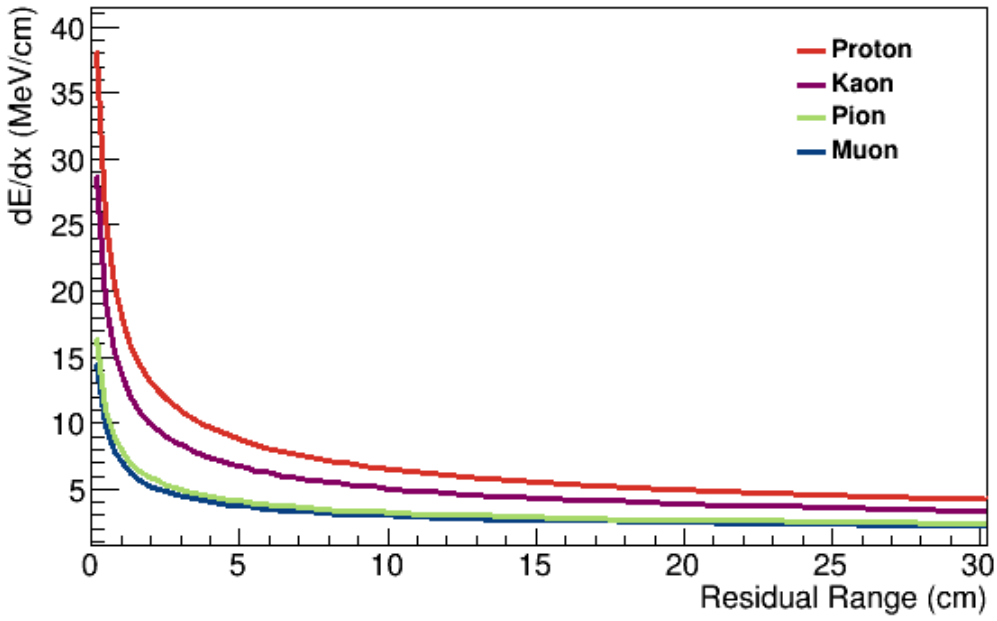


Figure 5.15: Distributions from theory of dE/dx versus residual range for several particle species. Figure from Ref. [82].

This information can be used to build probability maps for the dE/dx at each residual range, as shown in Figure 5.16. From this, a likelihood can then be calculated under a given particle species hypothesis:

$$L^s_{Total} = \frac{\sum_{i=1}^{N} L^s_i}{N} \tag{5.1}$$

where the sum is over the hits in the track that have residual range 0-30 cm (excluding the first and final hits) and $L^s_i$ is the likelihood for a particular species $s$ at the hit's dE/dx and residual range, as evaluated using the maps. The first hit is excluded because there can be a significant amount of contamination from other

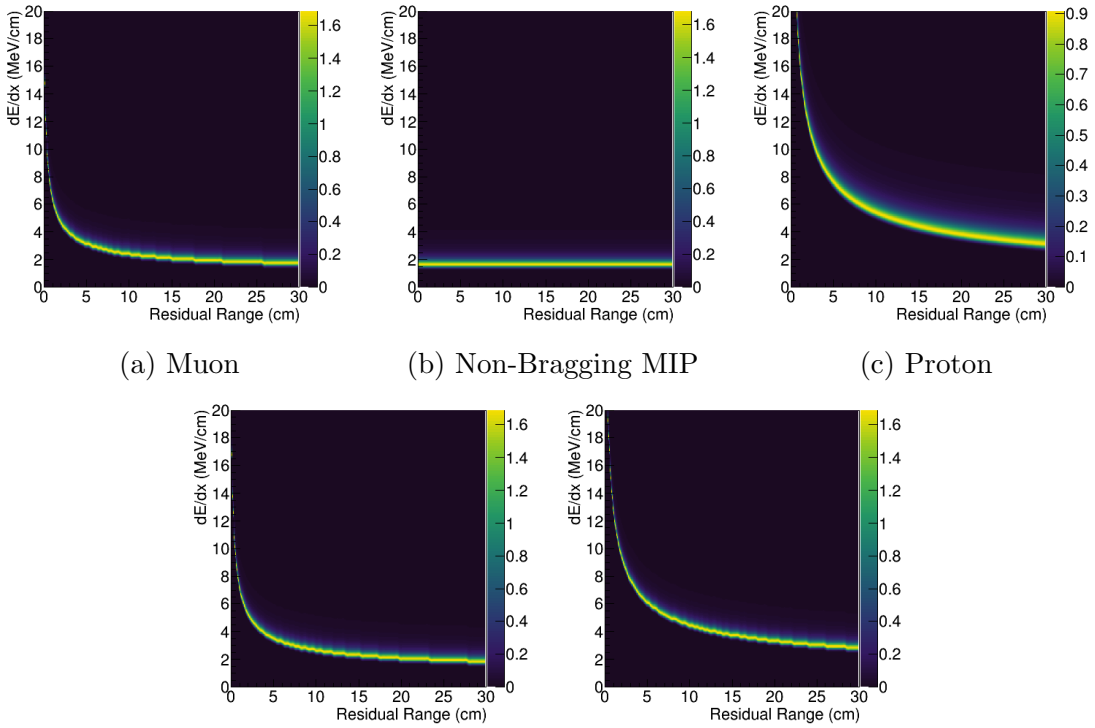


(a) Muon (b) Non-Bragging MIP (c) Proton

(d) Pion (e) Kaon

Figure 5.16: Probability maps for several particle species. Each bin of residual range is normalized to 100. A non-Bragging MIP refers to a MIP-like particle that exits the detector before stopping, and thus no Bragg peak is seen. Figures from Ref. [82].

particles coming from the same vertex, while the last hit is excluded because dE/dx measurements are found to sometimes be unreliable for it, for instance if the track ended between two wires.

Since the goal is to distinguish MIP-like particles from non-MIP-like particles, the selection variable $L_{MIP}/L_p$ is constructed, the ratio of the likelihood of a track being a MIP to the likelihood of it being a proton. Tracks that are more likely to be a MIP will have values greater than 1, while tracks that are more likely to be a proton will have values between 0 and 1. In order to allow for more equal binning between these two regions of the variable, the natural logarithm of the ratio is used instead. The distribution of this final variable, $\ln(L_{MIP}/L_p)$, for events selected at this stage of the CC1$\pi^+$ analysis, is shown in Figure 5.17.

### 5.4.5 Number of collection plane hits

The final input variable to the BDT is the number of collection plane hits in a track. Figure 5.18 shows the distribution of this variable. I expect proton tracks to be shorter (and therefore contain fewer hits) on average than MIPs, especially muons. The number of hits in pion tracks is more broadly distributed because pions

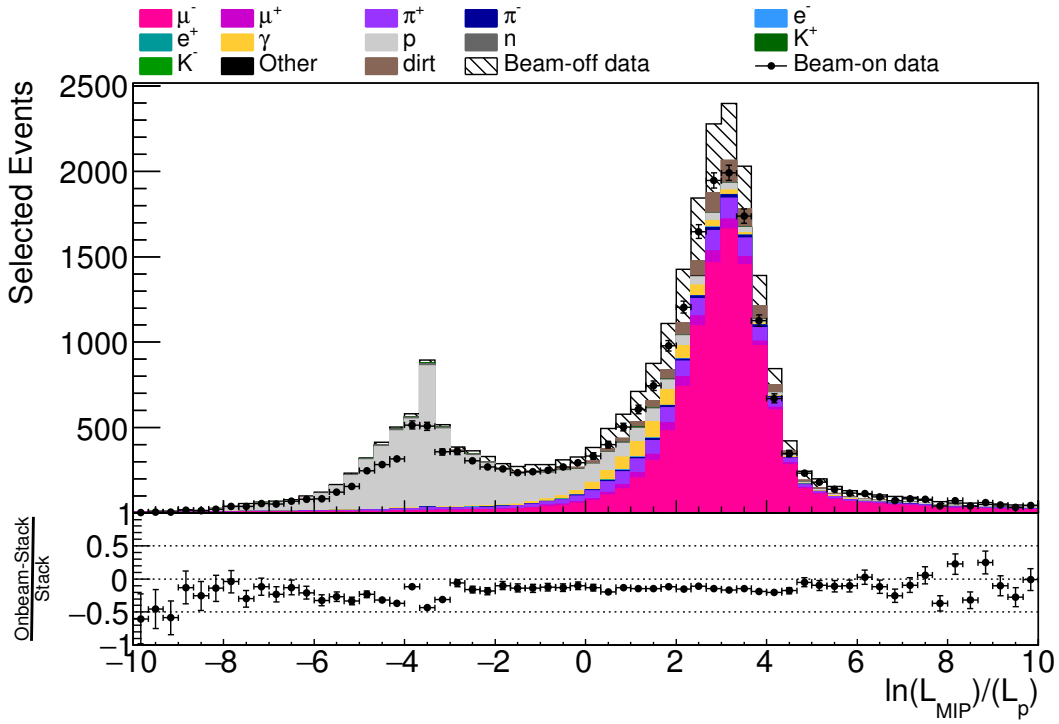


Figure 5.17: Distribution of log-likelihood values for each track. Figure produced by me for this analysis, not by the authors of the PID algorithm.

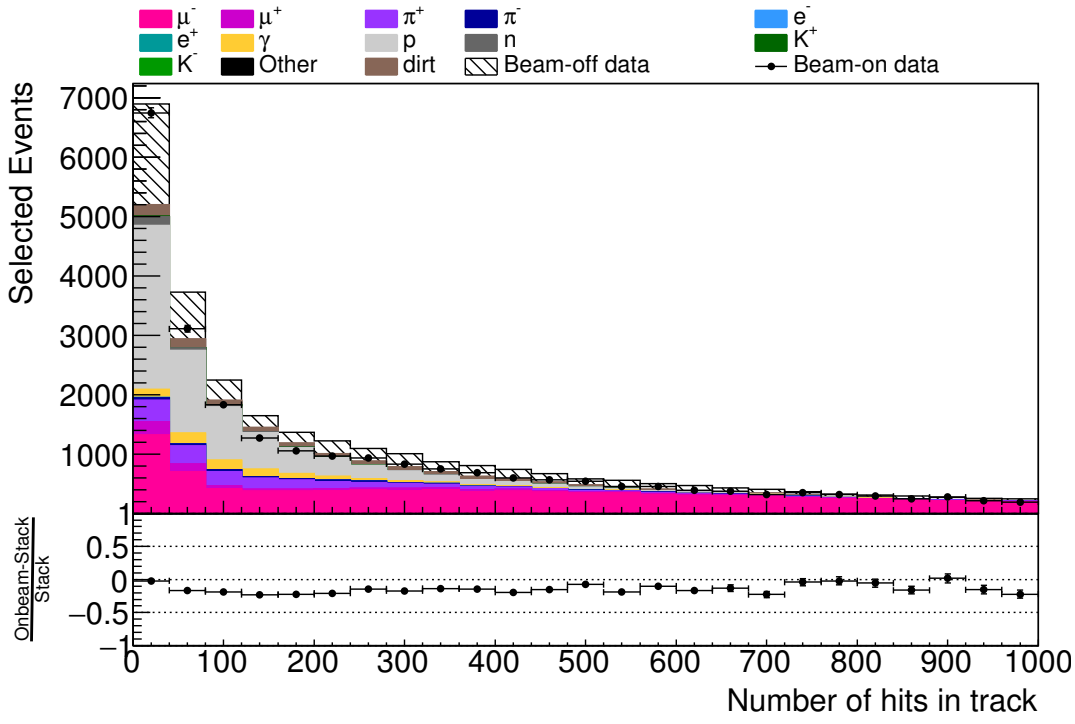


Figure 5.18: Distribution of the number of reconstructed hits per track.

sometimes interact hadronically, limiting the number of hits that can clearly be associated to them. Since the distributions for MIPs and non-MIPs have significant overlap, I am better able to analyse this situation with a BDT than I would with a single box cut.

### 5.4.6 BDT Output Score

Figure 5.19 shows the distribution of overall BDT scores for each track. There are two well-separated peaks, one of protons at -1 and one of muons and pions at +1, as desired. Data-MC agreement is good throughout most of the distribution. However, there are notably fewer data events in the first and last couple bins, compared to MC. This is attributable primarily to the lack of simulated DIC (see Section 2.3.4).

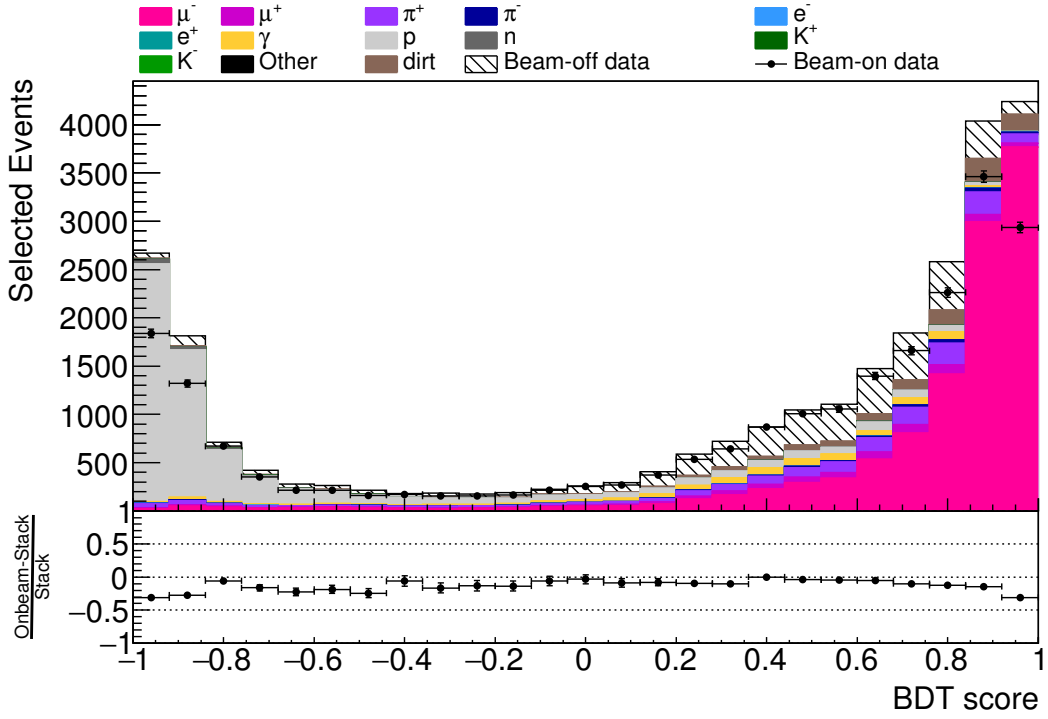


Figure 5.19: Distribution of BDT output scores for each track.

Figure 5.20 shows the efficiency, purity, and efficiency times purity as a function of the cut value for BDT score. The last of these is flat across most of the range of values, and so there is not a clear single best cut value. I decided to prioritise maintaining higher purity at the cost of efficiency, leading me to choose a value of 0.55. Specifically, as I am looking for events with two MIP-like tracks, I require that exactly two tracks in an event have BDT scores of at least 0.55. These two tracks become the MIP candidates. Figure 5.21 shows the distributions of track length and $\theta$ for the longest MIP candidate in each event, after this cut is applied.

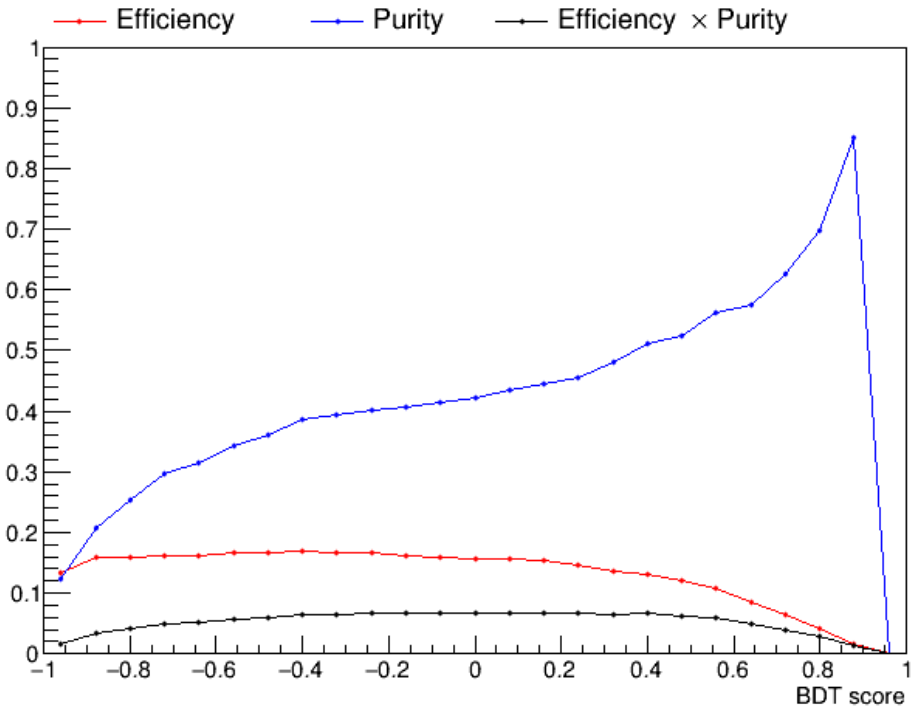


Figure 5.20: Efficiency (red), purity (blue), and efficiency times purity (black) of the selection, as a function of the cut value for BDT score.

## 5.5 Opening Angle

Figure 5.22a shows the distribution of angles between the two MIP candidates, which I refer to as the opening angle. There are a significant number of selected events where these tracks are close to back-to-back. These events are mostly not true signal events, and instead primarily occur due to reconstruction failures. Typically, a single true muon is split into two reconstructed tracks, with the neutrino vertex placed in the middle.

Figure 5.23 shows the results of a truth study where simulated pairs of MIP candidates are classified by whether or not they correspond to the same true particle. If they do, then they are a truly broken track; if not, they are truly not broken tracks. For truly broken tracks, the distribution of opening angles peaks strongly at $\pi$ radians (back-to-back), as one would expect. Conversely, the distribution for truly not broken tracks is much broader and peaks at a lower value. This shows that the high incidence of large opening angle tracks is indeed due to track breaking.

In order to eliminate these poorly reconstructed events, I require the opening angle to be less than 2.6 radians ($\approx$ 149 degrees). Figure 5.22b shows the distribution of opening angles after this cut is applied. It can be seen that the remaining events have a significantly higher signal purity. Figure 5.24 shows the distributions of track length and $\theta$ for the longest MIP candidate in each event, after this cut is applied.

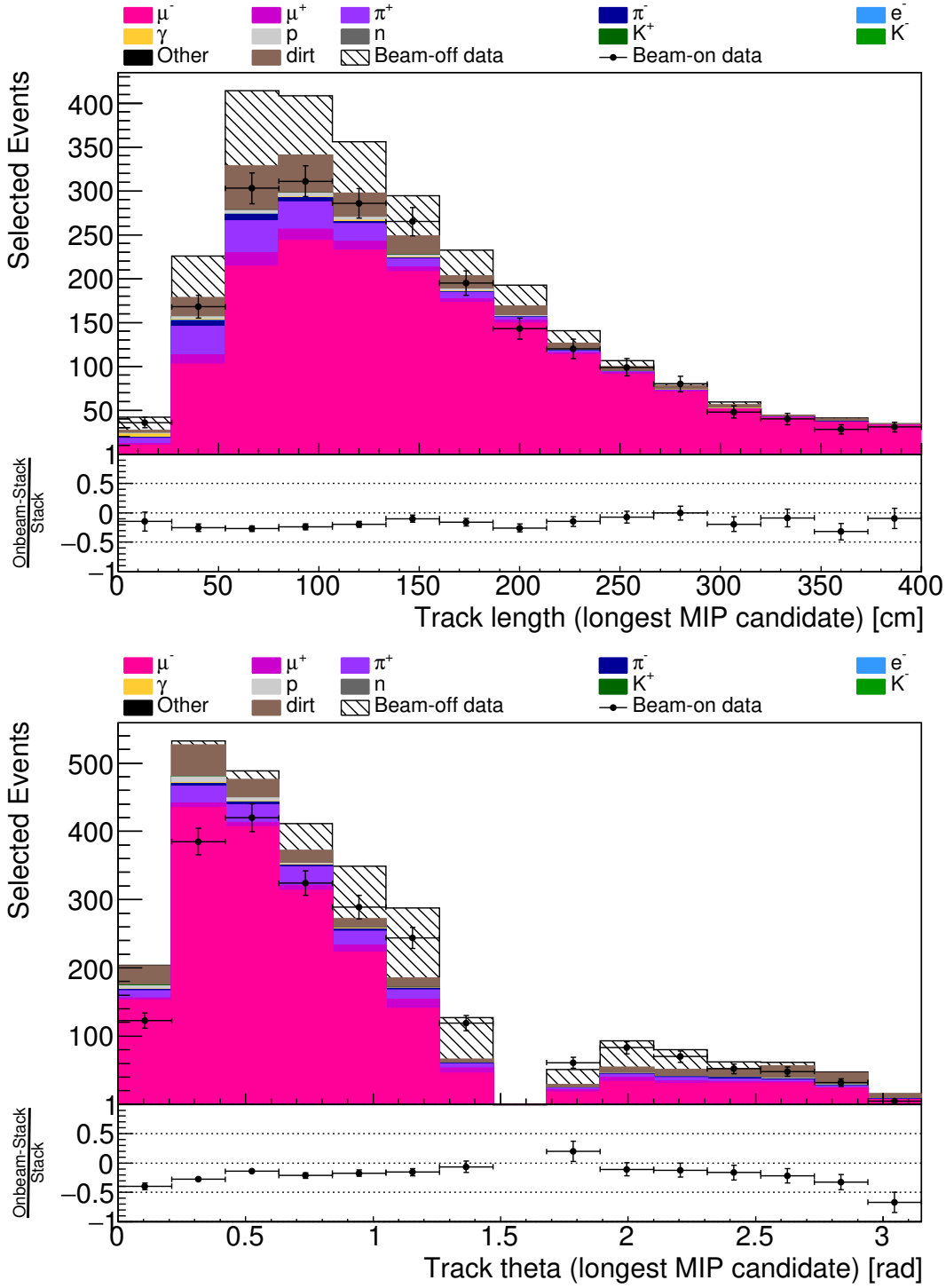


Figure 5.21: The distributions of track length (top) and polar angle $\theta$ (bottom) for the longest MIP candidate in each event, after the cut on BDT score is applied.

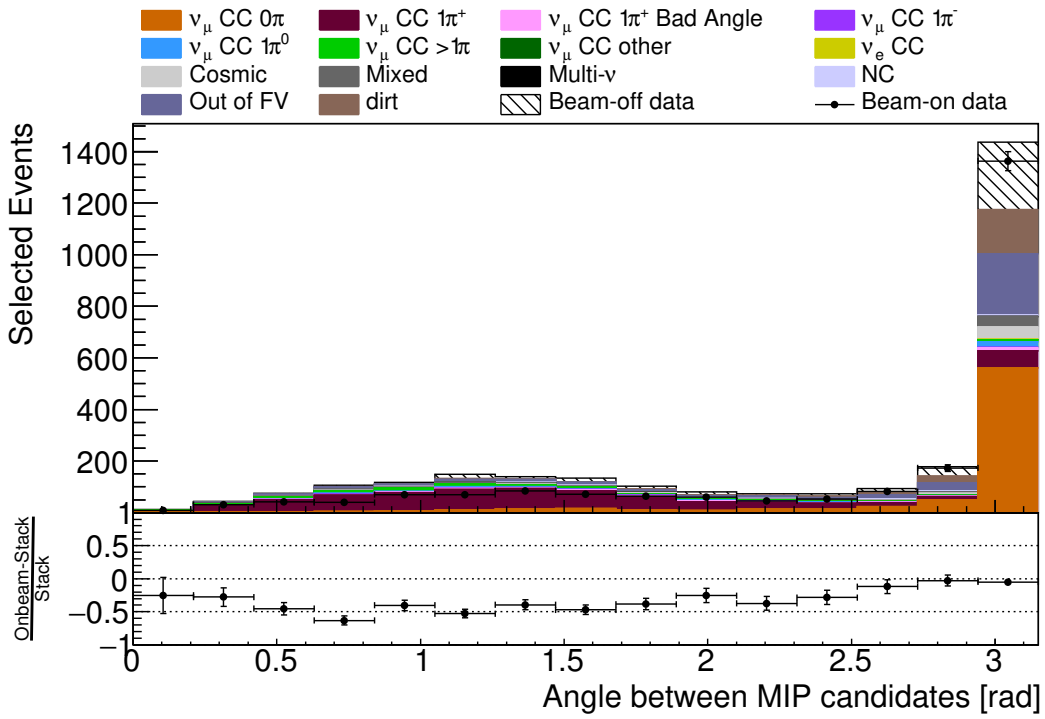


(a) Before cut

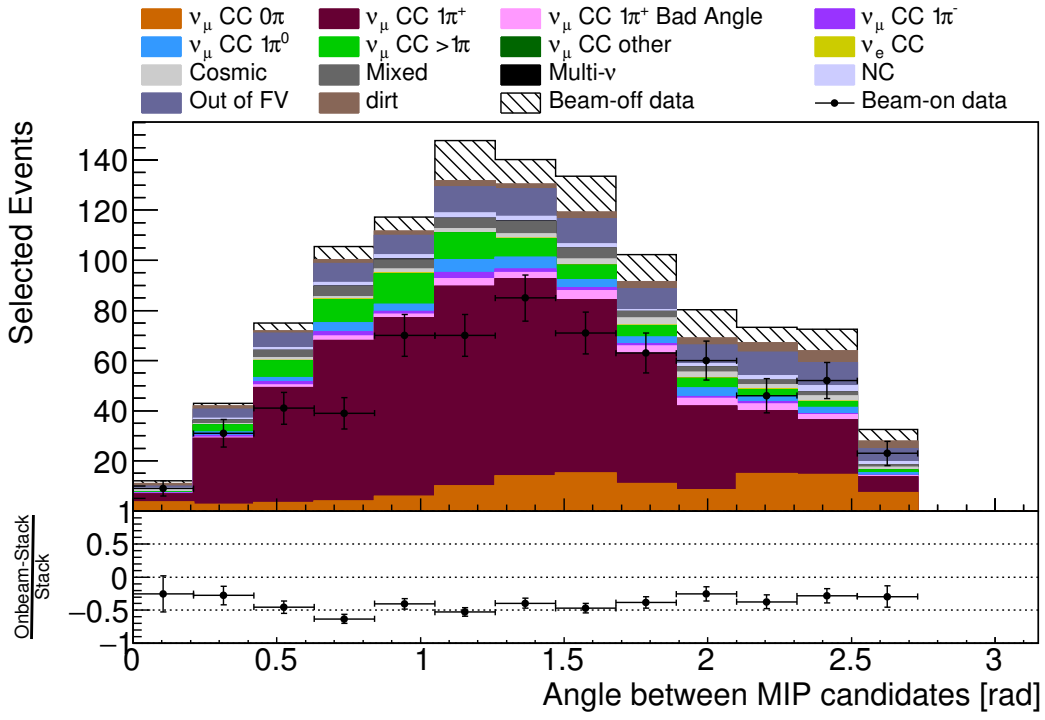


(b) After cut

Figure 5.22: Distribution of opening angles, i.e. the angle between the two MIP candidates, (a) before and (b) after applying a cut at 2.6 radians.

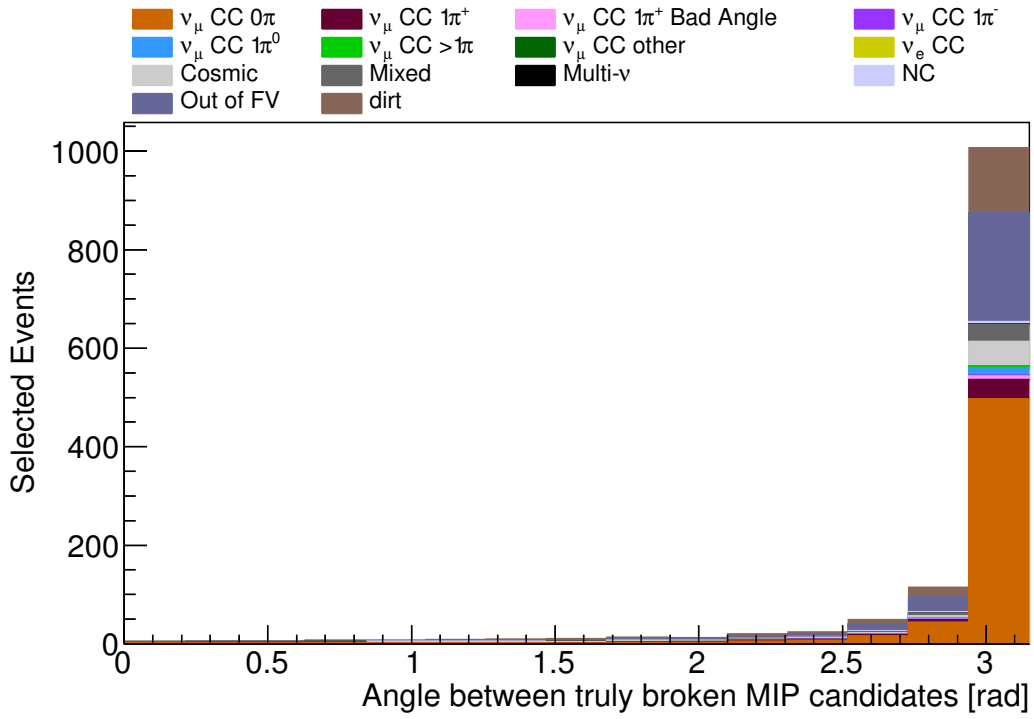


(a) Truly broken

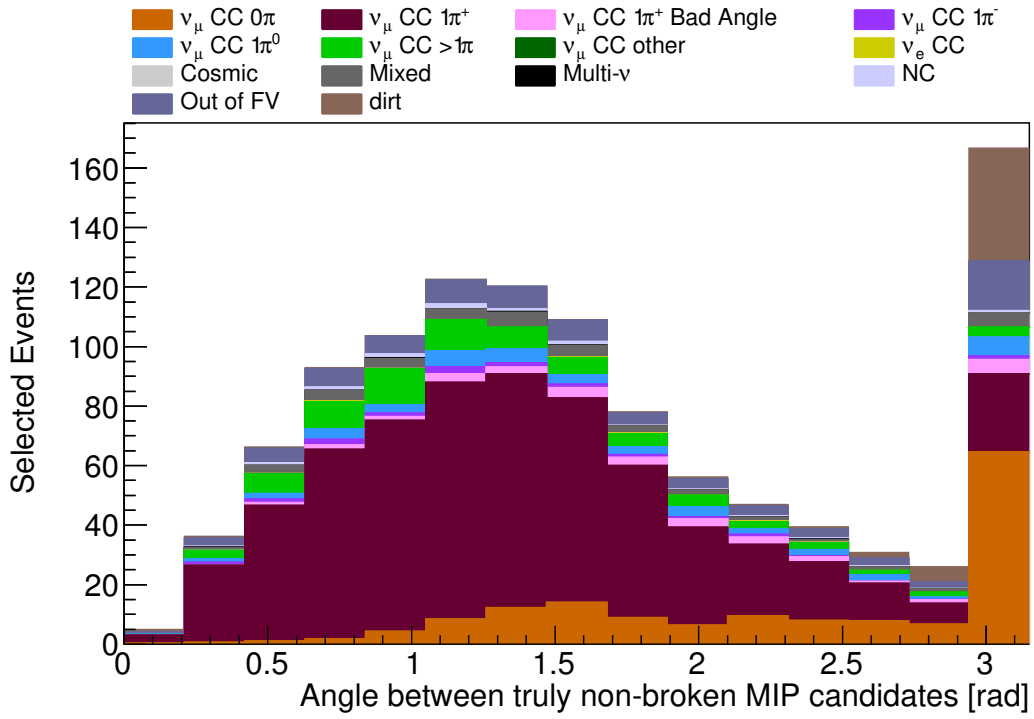


(b) Truly not broken

Figure 5.23: Distribution of angles between simulated MIP candidates that are (a) truly broken and (b) truly not broken. Truly broken tracks, for which the two MIP candidates correspond to the same true particles, are strongly peaked toward $\pi$ radians (back-to-back). Conversely, truly not broken tracks, for which the two MIP candidates correspond to different true particles, are distributed more broadly across the range of angles and peak at a lower angle.

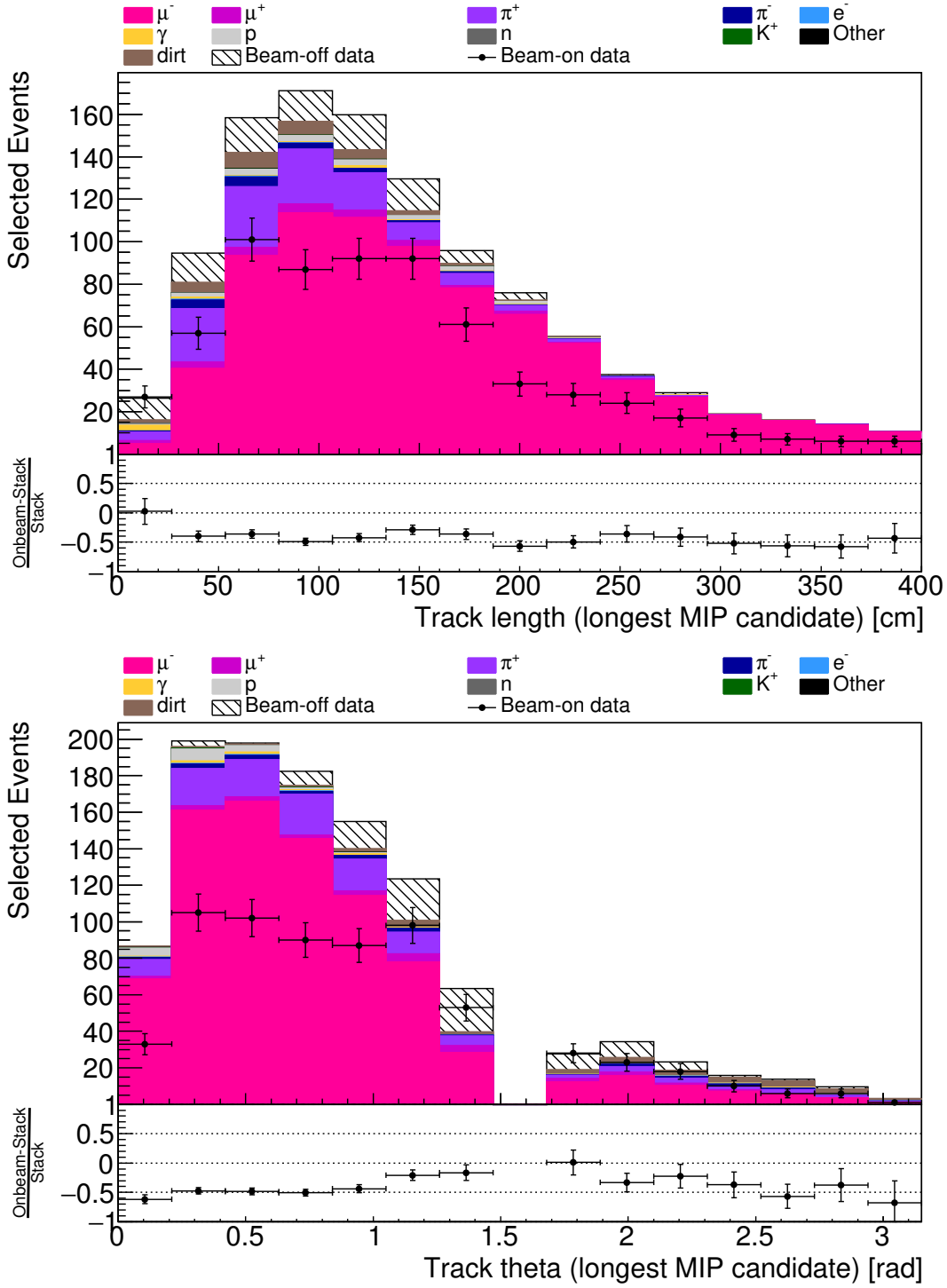


Figure 5.24: The distributions of track length (top) and polar angle $\theta$ (bottom) for the longest MIP candidate in each event, after the cut on opening angle is applied.

This cut is potentially problematic because the opening angle is dependent on physics models that are still an active area of research. Figure 5.25 shows the $\nu_\mu$ CC1$\pi^\pm$ differential cross section as a function of opening angle, as measured by ArgoNeuT and compared with predictions from several generators. Both data and all four generators predict a very low cross section at high opening angles. I therefore decided that even a relatively large difference between my measurement and prediction in this area of phase space would not significantly impact the overall analysis. Additionally, the ArgoNeuT selection employed a similar cut in order to deal with the same issue of track breaking, which set precedence for its use in this selection.

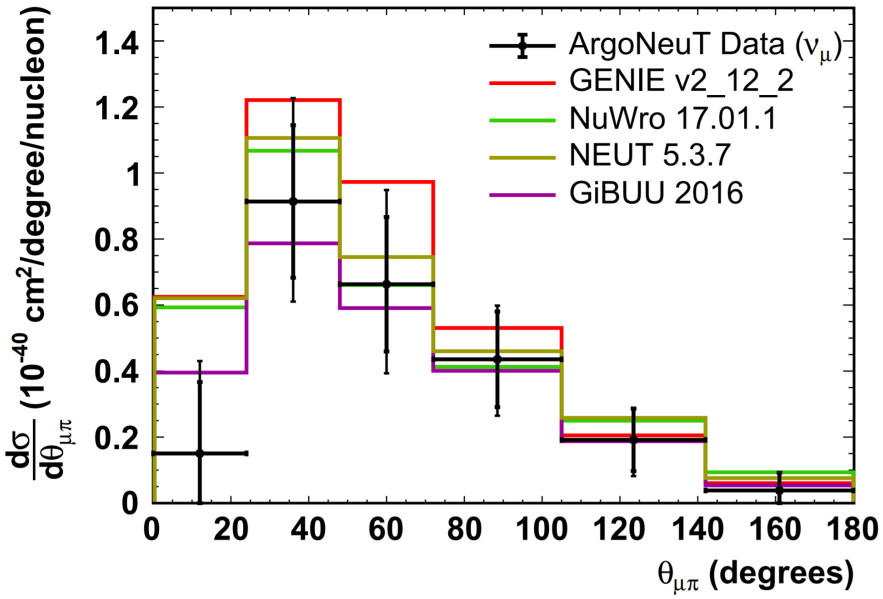


Figure 5.25: $\nu_\mu$ CC1$\pi^\pm$ differential cross section as a function of opening angle. ArgoNeuT measurement is compared with predictions from several generators. Figure from Ref. [34].

Unfortunately, this cut did turn out to be partially responsible for data-MC disagreement in the final selection. The normalisations of the data and MC agree better in some regions of the distribution than others. This leads to unequal amounts of MC and data being removed by this cut, leading to poorer overall normalisation agreement afterwards. Section 7.2 describes further details on the data-MC opening angle disagreement and Section 8.2 provides a proposed path forward for future analyses.

## 5.6 Containment

Although this analysis does not include any differential cross section measurements, they are a clear area of work that MicroBooNE would aim to accomplish in the

future. These measurements would include the cross section as a function of muon momentum and of pion momentum. It is significantly more difficult to measure these properties if the particles are not fully contained. Unfortunately, a significant proportion of CC1$\pi^+$ events are found to not be fully contained in MicroBooNE. This is most often due to the muon exiting. For these cases, MicroBooNE has developed a method of determining muon momentum that does not require containment, based on an improved model of multiple Coulomb scattering [83]. Pions, on the other hand, often undergo additional hadronic interactions, which makes momentum calculations very difficult even without trying to account for uncontained particles. I therefore place a containment requirement on selected events: at least one MIP candidate must be contained. Figure 5.26 shows the distribution of events that do or don't meet this requirement. Figure 5.27 shows the distributions of track length and $\theta$ for the longest MIP candidate in each event, after this cut is applied.

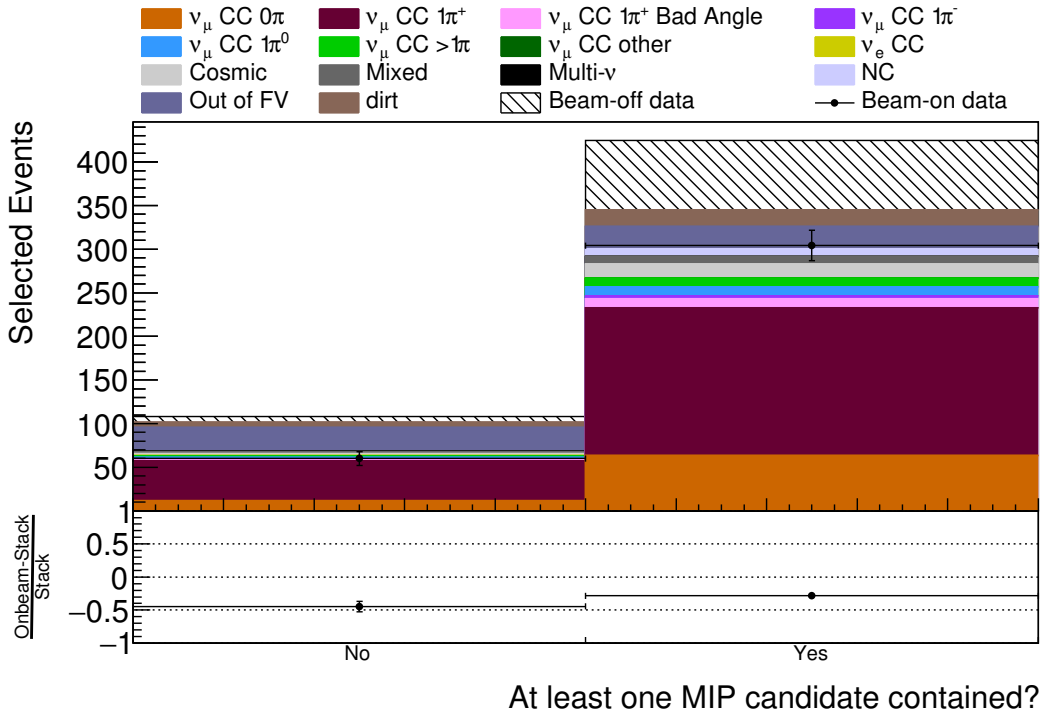


Figure 5.26: Distribution of whether at least one MIP candidate is contained in each event.

## 5.7 Muon-Pion Separation

Categorising the two MIP candidates as a muon candidate and a pion candidate is not strictly necessary for a total cross section measurement. However, as discussed previously, differential cross section measurements in terms of the particles' kinematic variables are a goal of future work. It is therefore useful to look at how well

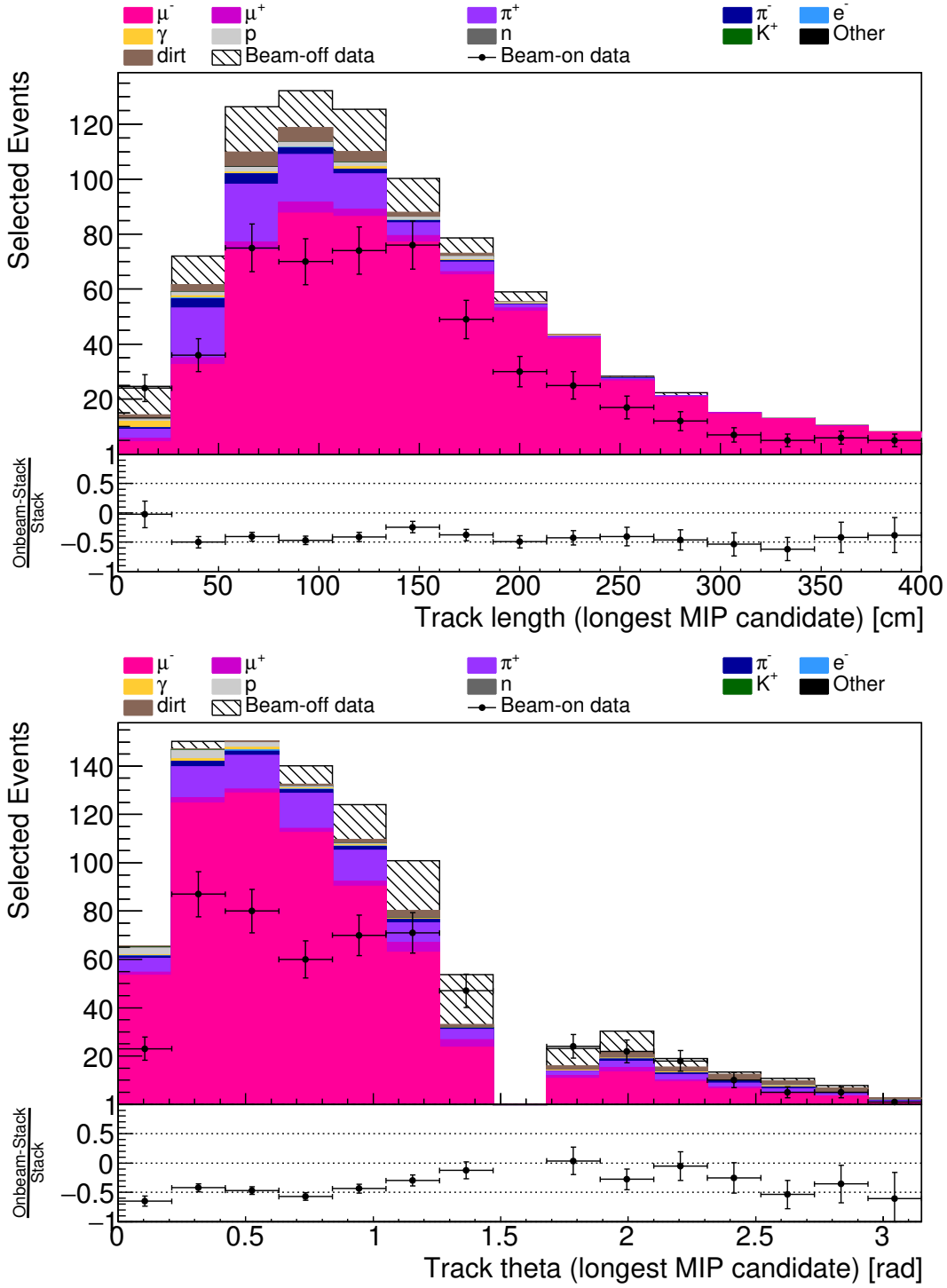


Figure 5.27: The distributions of track length (top) and polar angle $\theta$ (bottom) for the longest MIP candidate in each event, after the containment cut is applied.

the two can be separated right now, using only some simple criteria.

If only one MIP candidate is contained, I designate it as the pion candidate and the uncontained one as the muon candidate. If both MIP candidates are contained, I designate the shorter one as the pion candidate and the longer one as the muon candidate. Figure 5.28 shows, for selected true signal events, the distribution of true particle species for both the muon candidate and pion candidate. This shows that I correctly identify the muon as the muon candidate 87.8% of the time, correctly identify the pion as the pion candidate 87.0% of the time, and correctly identify both at once 86.2% of the time. These metrics are a good starting basis, and additional future work could improve them further. One possible line of inquiry is to use another BDT for the classification of muons versus pions. See Section 8.4 for further discussion.

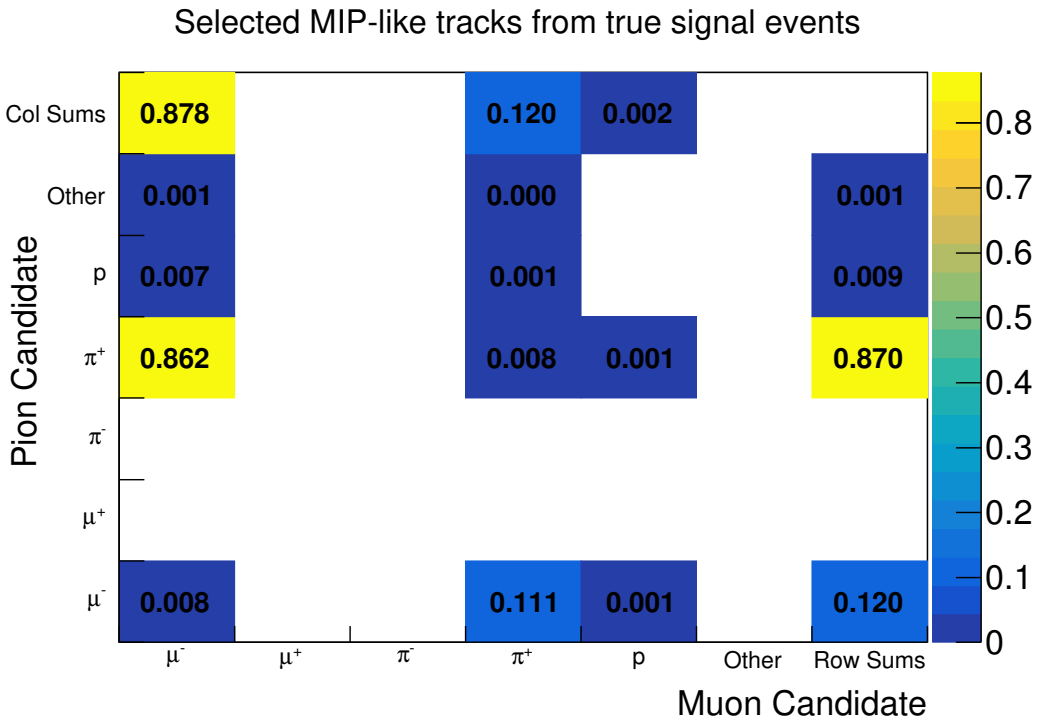


Figure 5.28: 2D distribution of the proportion of selected true signal events with a given true particle species of the muon candidate (x-axis) and of the pion candidate (y-axis). For example, in 86.2% of these events, the muon candidate was truly a muon and the pion candidate was truly a pion.

## 5.8 Results

The performance of the selection can be evaluated by looking at its efficiency

$$\epsilon = \frac{\text{Selected CC1}\pi^+ \text{ signal events}}{\text{Generated CC1}\pi^+ \text{ signal events}} \tag{5.2}$$

and purity

$$\rho = \frac{\text{Selected CC1}\pi^+ \text{ signal events}}{\text{All selected events}}. \tag{5.3}$$

Table 5.1 shows the efficiency and purity at each stage of the selection, as well as the number of passing events (scaled to the beam-on data POT of $1.763 \times 10^{20}$). The final selection has an efficiency of 11.5% and a purity of 58.0%. For comparison, the CC inclusive selection that is used as a pre-selection has an efficiency of 57.2% and a purity of 50.4% (for all CC events). Figure 5.29 shows the CC1$\pi^+$ selection efficiency as a function of the true neutrino energy, true muon momentum, and true pion momentum in true CC1$\pi^+$ signal events. As is expected, efficiency is lower at low energy and momenta. However, once it peaks, the efficiency remains fairly flat across the remainder of the phase space.

| Cut | MC Signal | Full MC | Beam-on Data | Beam-off Data | Efficiency | Purity |
|---|---|---|---|---|---|---|
| CC Inclusive | 2,252.2 | 23,836.9 | 30,154 | 9,777.6 | 56.7% | 9.4% |
| Vtx.-Track Dist. | 938.8 | 11,154.3 | 13,454 | 3,930.0 | 23.6% | 8.4% |
| Polar Angle | 991.8 | 10,310.8 | 11,105 | 2,404.6 | 25.0% | 9.6% |
| BDT | 651.8 | 2,370.7 | 2,255 | 405.7 | 16.4% | 27.5% |
| Opening Angle | 567.0 | 1,017.8 | 660 | 98.4 | 14.3% | 55.7% |
| Containment | 457.9 | 788.9 | 523 | 89.6 | 11.5% | 58.0% |

Table 5.1: Passing event counts, efficiency, and purity at each stage of the event selection. Event counts are scaled to the Beam-on Data POT of $1.763 \times 10^{20}$.

Kinematic distributions for muon and pion candidates in selected events are shown in Figures 5.30 and 5.31, respectively. A clear normalisation difference can be seen between simulation and data. This is primarily due to the lack of DIC effects in the simulation and to issues with the cut on opening angle.

Overall shape agreement is reasonable, though there are some specific regions of more significant disagreement. The muon candidate $\phi$ distribution shows slight shape disagreement, while the pion candidate $\phi$ distribution shows more pronounced shape disagreement. Both of these can be attributed to the lack of DIC effects in the simulation.

The CC inclusive analysis found a shape disagreement in the muon candidate $\theta$ distribution for very forward-going tracks ($\theta$ near 0) [81]. This effect can also be seen in this analysis. Better agreement is seen when using the alternative GENIE model (see Section 2.3.3 for description). The CC inclusive analysers attribute this to the alternative model's use of the local Fermi gas model, and to a lesser extent its inclusion of RPA effects.

The default simulation's lack of DIC effects has a large impact on this analysis. One possible way to address this is to assess it as a systematic uncertainty. However, given the size of the effect, I felt this was not the most appropriate course of action

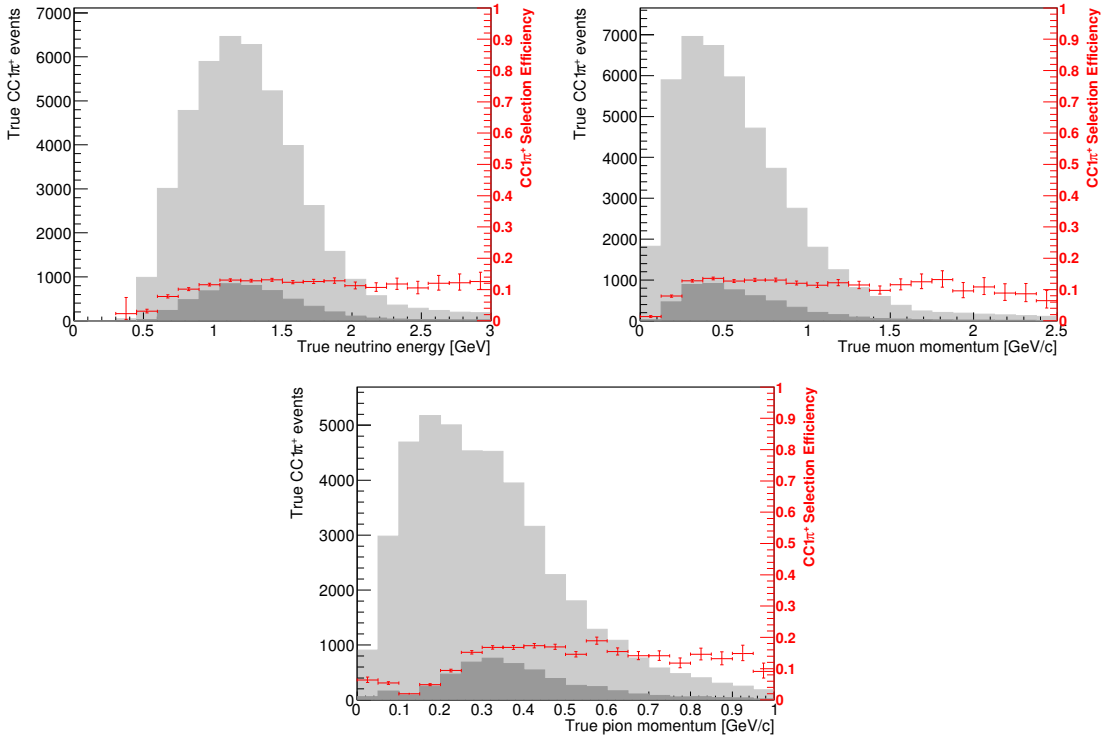


Figure 5.29: CC1$\pi^+$ selection efficiency as a function of true neutrino energy, true muon momentum, and true pion momentum in true CC1$\pi^+$ signal events. The distributions of true signal events before the selection is applied are shown in light grey, while the distributions after the full selection are shown in dark grey. Note that they are not stacked.

in this case. I instead produced a new baseline sample by using a preliminary version of the next generation of the simulation, which includes the DIC effect. Due to both technical and temporal limitations, it is not feasible for this analysis to produce comparable statistics to the default sample, nor to re-tune the selection using it. However, it may still be used to extract the cross section and achieve a more accurate result. This process is described in further detail in Section 7.1.

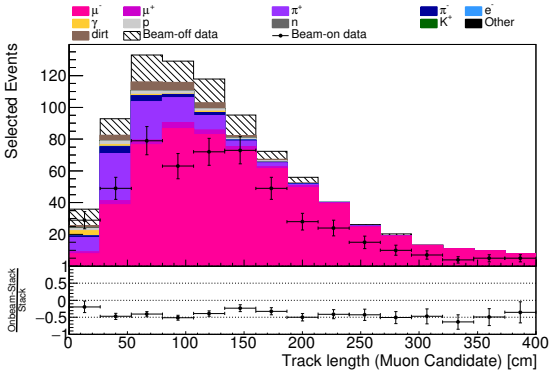


(a) Track length

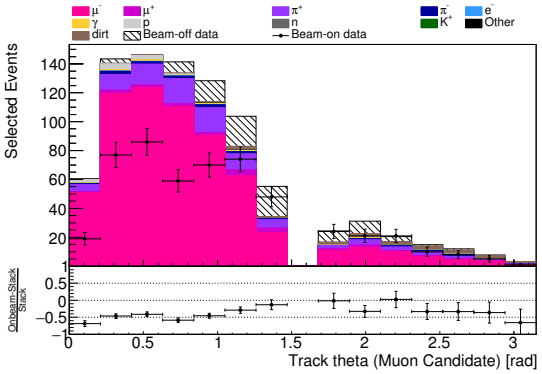


(b) Track $\theta$

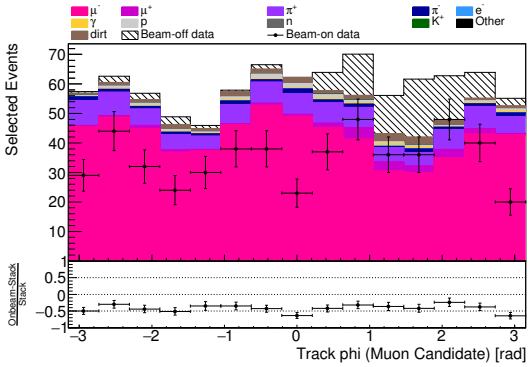


(c) Track $\phi$

Figure 5.30: Kinematic distributions for muon candidate tracks.

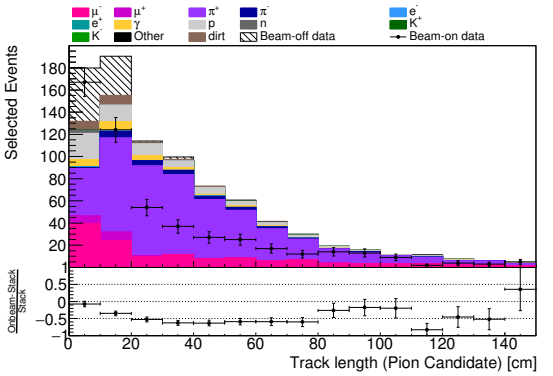


(a) Track length

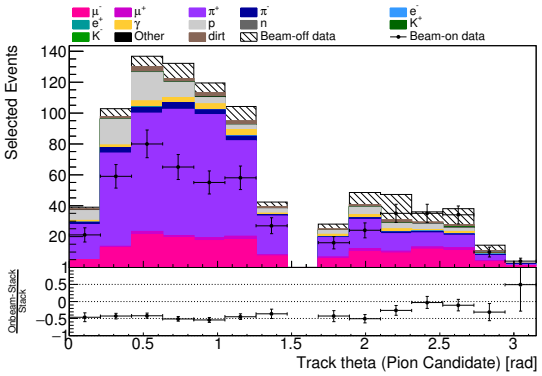


(b) Track $\theta$

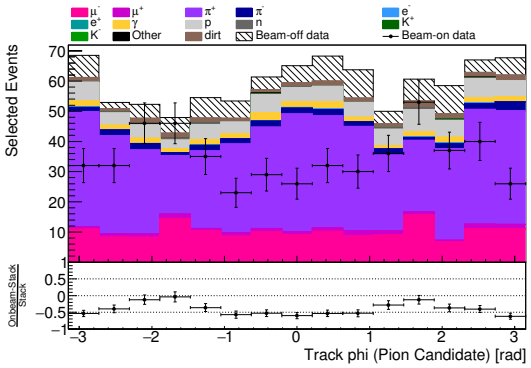


(c) Track $\phi$

Figure 5.31: Kinematic distributions for pion candidate tracks.

# Chapter 6

# Systematic Uncertainties

Most systematic uncertainties in MicroBooNE are evaluated with one of two approaches: "unisims" or "multisims." In the unisim approach, parameters are varied one by one, by a set amount, and a new set of MC events is generated for each. In the multisim approach, all of the model parameters are varied at once. Each parameter is randomly sampled from within its uncertainty, with an assumed Gaussian distribution and with correlations where necessary. This produces a set of weights that can be used to generate new "universes" from the baseline MC, in a process called reweighting.

From these universes one may then construct a covariance matrix

$$C_{i,j} = \frac{1}{N}\sum_{n=1}^{N}(\sigma_i^n - \sigma_i^{CV})(\sigma_j^n - \sigma_j^{CV}), \tag{6.1}$$

where $N$ is the number of universes, $i$ and $j$ are bins in the distribution of a given measured quantity, $\sigma_i^n$ is the cross section in universe $n$ and bin $i$, and $\sigma_i^{CV}$ is the central value cross section in bin $i$. This matrix describes how changes in each bin of the distribution correspond to changes in the other bins. One may also define the fractional covariance matrix

$$F_{i,j} = \frac{C_{i,j}}{\sigma_i^{CV}\sigma_j^{CV}}. \tag{6.2}$$

The fractional uncertainty in each bin of the distribution is then given simply by $\sqrt{F_{i,i}}$. In several places throughout this chapter, the event rate as a function of the track length of the leading MIP candidate is used as an illustration of how changes to the parameters under consideration affect this analysis. The distribution for each universe is shown, along with the corresponding covariance and fractional covariance matrices.

Each section in this chapter describes a source of uncertainty: cross section modelling in Section 6.1, beam flux modelling in Section 6.2, detector modelling in Section 6.3, POT counting in Section 6.4, simulated dirt modelling in Section 6.5,

simulated cosmic modelling in Section 6.6, and number of targets in Section 6.7. Finally, the results are summarised in Section 6.8.

## 6.1 Cross Section Uncertainties

Cross sections encompass a large number of underlying uncertainties, which I assess in three separate groups. The first group is for interaction-related uncertainties, the second for uncertainties that arise out of my choice of models, and the third for uncertainties for hadron reinteractions. These are each described in detail in the following sections.

### 6.1.1 Interaction Uncertainties

I assess interaction-related systematic uncertainties using GENIE's built-in framework for reweighting events [52, 53]. For each physics parameter $P$ with estimated standard deviation $\delta P$, I simulate the effect on the cross section of changing its value by a randomly chosen, Gaussian distributed amount. Table 6.1 provides a list of the parameters used in this analysis. The parameters fall roughly into five groups, as separated in the table. The first group of parameters relates to cross sections for various processes important at MicroBooNE's energy scales. The second is similar, but for deep inelastic scattering (DIS) interactions, which occur at higher energies. The third relates to hadronisation and resonance decays. The fourth describes non-resonant backgrounds of interactions that have final state pions. And the fifth and final group characterises intranuclear hadron transport. Note that the empirical MEC model used in my default tune of GENIE does not have associated uncertainties and so cannot be included within this framework. Section 6.1.3 describes how systematic uncertainties are separately assessed for it.

As this is a large number of parameters, it is worthwhile to highlight some of the more important ones for this analysis. The models considered here (see Section 2.3.3 for description) describe the cross sections for various interaction processes with "form factors" that approximate the structure of the nucleons. These form factors include parameters known as axial masses $M_A$ and vector masses $M_V$, whose values must be obtained through experiment. This analysis is sensitive in particular to the values of $M_A^{CCRES}$, $M_V^{CCRES}$, and $M_A^{CCQE}$ since these processes constitute the majority of selected events.

I utilise a multisim approach to these interaction uncertainties, with all of the parameters being reweighted at the same time. 100 universes were generated and the distribution of their cross sections is shown in Figure 6.1, along with the distribution of event rates as a function of the track length of the leading MIP candidate and the

| Parameter $P$ | Description of $P$ | Value | $\delta P/P$ |
|---|---|---|---|
| $M_A^{NCEL}$ | Axial mass for NC elastic | 0.990 GeV | ±25% |
| $\eta^{NCEL}$ | Strange axial form factor $\eta$ for NC elastic | 0.120 GeV | ±30% |
| $M_A^{CCQE}$ | Axial mass for CC QE | 0.990 GeV | $-15\% + 25\%$ |
| $M_A^{CCRES}$ | Axial mass for CC resonance neutrino production | 1.120 GeV | ±20% |
| $M_V^{CCRES}$ | Vector mass for CC resonance neutrino production | 0.840 GeV | ±10% |
| $M_A^{NCRES}$ | Axial mass for NC resonance neutrino production | 1.120 GeV | ±20% |
| $M_V^{NCRES}$ | Vector mass for NC resonance neutrino production | 0.840 GeV | ±10% |
| $M_A^{COH\pi}$ | Axial mass for CC and NC coherent pion production | 1.000 GeV | ±50% |
| $R_0^{COH\pi}$ | Nuclear size param. controlling $\pi$ absorption in RS model | 1.000 fm | ±10% |
| CCQE-PauliSup ($p$) | CCQE Pauli suppression (via changes in Fermi level $k_F$) | 0.242 GeV | ±35% |
| CCQE-PauliSup ($n$) | CCQE Pauli suppression (via changes in Fermi level $k_F$) | 0.259 GeV | ±35% |
| $A_{HT}^{BY}$ | $A_{HT}$ higher-twist param. in BY model scaling variable $\xi_w$ | 0.538 | ±25% |
| $B_{HT}^{BY}$ | $B_{HT}$ higher-twist param. in BY model scaling variable $\xi_w$ | 0.305 | ±25% |
| $C_{V1u}^{BY}$ | $C_{V1u}$ u valence GRV98 PDF correction param in BY model | 0.291 | ±30% |
| $C_{V2u}^{BY}$ | $C_{V2u}$ u valence GRV98 PDF correction param in BY model | 0.291 | ±30% |
| FZ (pion) | Hadron formation zone | 0.342 fm | ±50% |
| FZ (nucleon) | Hadron formation zone | 2.300 fm | ±50% |
| BR($\gamma$) | Branching ratio for radiative resonance decays | - | ±50% |
| BR($\eta$) | Branching ratio for single-$\eta$ resonance decays | - | ±50% |
| $R_{\nu p}^{CC1\pi}$ | Non-resonance bkg in $\nu p$ CC1$\pi$ reactions | - | ±50% |
| $R_{\nu p}^{CC2\pi}$ | Non-resonance bkg in $\nu p$ CC2$\pi$ reactions | - | ±50% |
| $R_{\nu n}^{CC1\pi}$ | Non-resonance bkg in $\nu n$ CC1$\pi$ reactions | - | ±50% |
| $R_{\nu n}^{CC2\pi}$ | Non-resonance bkg in $\nu n$ CC2$\pi$ reactions | - | ±50% |
| $R_{\nu p}^{NC1\pi}$ | Non-resonance bkg in $\nu p$ NC1$\pi$ reactions | - | ±50% |
| $R_{\nu p}^{NC2\pi}$ | Non-resonance bkg in $\nu p$ NC2$\pi$ reactions | - | ±50% |
| $R_{\nu n}^{NC1\pi}$ | Non-resonance bkg in $\nu n$ NC1$\pi$ reactions | - | ±50% |
| $R_{\nu n}^{NC2\pi}$ | Non-resonance bkg in $\nu n$ NC2$\pi$ reactions | - | ±50% |
| $x_{mfp}^N$ | Nucleon mean free path (total rescattering probability) | - | ±20% |
| $x_{cex}^N$ | Nucleon charge exchange probability | - | ±50% |
| $x_{el}^N$ | Nucleon elastic reaction probability | - | ±30% |
| $x_{inel}^N$ | Nucleon inelastic reaction probability | - | ±40% |
| $x_{abs}^N$ | Nucleon absorption probability | - | ±20% |
| $x_{\pi}^N$ | Nucleon $\pi$-production probability | - | ±20% |
| $x_{mfp}^{\pi}$ | $\pi$ mean free path (total rescattering probability) | - | ±20% |
| $x_{cex}^{\pi}$ | $\pi$ charge exchange probability | - | ±50% |
| $x_{el}^{\pi}$ | $\pi$ elastic reaction probability | - | ±10% |
| $x_{inel}^{\pi}$ | $\pi$ inelastic reaction probability | - | ±40% |
| $x_{abs}^{\pi}$ | $\pi$ absorption probability | - | ±20% |
| $x_{\pi}^{\pi}$ | $\pi$ $\pi$-production probability | - | ±20% |

Table 6.1: List of physics parameters used to assess interaction-related systematic uncertainties in this analysis, including the default value (where available) and prior estimated standard deviation of each. Information reproduced from Ref. [53] for ease of reference.

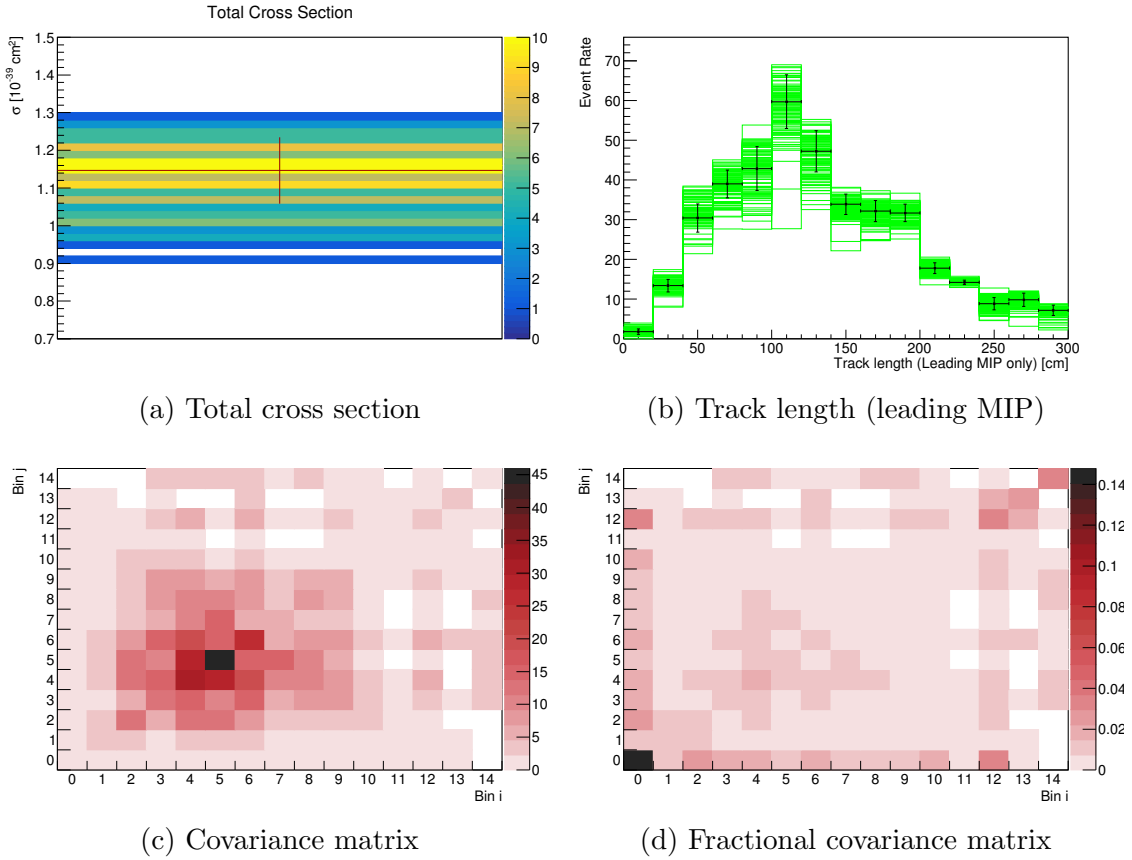


(a) Total cross section

(b) Track length (leading MIP)

(c) Covariance matrix

(d) Fractional covariance matrix

Figure 6.1: Utilising a multisim approach, 100 universes were generated to assess the interaction-related systematic uncertainties. (a): The distributions of their cross sections (CV in red). Error bar shows the total interaction-related systematic uncertainty. (b): The distribution of event rates as a function of the track length of the leading MIP candidate (CV in black). (c) and (d): Covariance and fractional covariance matrices, respectively.

corresponding covariance and fractional covariance matrices. In total, interaction-related uncertainties account for a systematic uncertainty of 7.68%.

### 6.1.2 Interaction Uncertainty Unisims

In addition to the multisim analysis described in the previous section, each interaction parameter is individually assessed with a unisim approach. This is used purely as a cross-check, allowing me to more easily see whether there are issues with the implementation of any individual parameters. Table 6.2 provides a summary of the results, which are consistent with expectations.

### 6.1.3 QE and MEC Cross Section Uncertainties

This section describes how I evaluate the systematic effect of my choice of models. In my default tune of GENIE, the QE cross section model does not take into account

| Parameter $P$ | Total Cross Section Relative Uncertainty | |
|---|---|---|
| | $+1\sigma$ | $-1\sigma$ |
| $M_A^{NCEL}$ | 0.34% | 0.36% |
| $\eta^{NCEL}$ | 0.01% | 0.01% |
| $M_A^{CCQE}$ | 6.26% | 3.48% |
| $M_A^{CCRES}$ | 5.14% | 5.38% |
| $M_V^{CCRES}$ | 2.96% | 2.76% |
| $M_A^{NCRES}$ | 0.82% | 0.85% |
| $M_V^{NCRES}$ | 0.26% | 0.25% |
| $M_A^{COH\pi}$ | 0.21% | 0.21% |
| $R_0^{COH\pi}$ | 0.21% | 0.21% |
| CCQE-PauliSup | 0.72% | 0.56% |
| $A_{HT}^{BY}$ | 0.05% | 0.05% |
| $B_{HT}^{BY}$ | 0.08% | 0.09% |
| $C_{V1u}^{BY}$ | 0.04% | 0.04% |
| $C_{V2u}^{BY}$ | 0.03% | 0.03% |
| FZ | 1.83% | 2.29% |
| BR($\gamma$) | 0.03% | 0.03% |
| BR($\eta$) | 0.38% | 0.38% |
| $R_{\nu p}^{1\pi}$ | 0.92% | 0.92% |
| $R_{\nu p}^{2\pi}$ | 1.74% | 1.74% |
| $R_{\nu n}^{1\pi}$ | 2.68% | 2.68% |
| $R_{\nu n}^{2\pi}$ | 1.53% | 1.53% |
| $x_{mfp}^{N}$ | 0.52% | 0.54% |
| $x_{cex}^{N}$ | 0.70% | 0.71% |
| $x_{el}^{N}$ | 0.66% | 0.51% |
| $x_{inel}^{N}$ | 0.29% | 0.18% |
| $x_{abs}^{N}$ | 0.30% | 0.27% |
| $x_{\pi}^{N}$ | 0.31% | 0.31% |
| $x_{mfp}^{\pi}$ | 0.98% | 0.42% |
| $x_{cex}^{\pi}$ | 0.51% | 0.52% |
| $x_{el}^{\pi}$ | 0.00% | 0.01% |
| $x_{inel}^{\pi}$ | 3.27% | 3.25% |
| $x_{abs}^{\pi}$ | 3.46% | 3.50% |
| $x_{\pi}^{\pi}$ | 0.19% | 0.19% |

Table 6.2: The systematic uncertainty on the total cross section due to each interaction parameter, assessed using a unisim approach. Descriptions of the parameters and variations are given in Table 6.1. For technical reasons, some closely related parameters are combined here.

Random Phase Approximation (RPA) effects. Additionally, the empirical MEC model does not have associated uncertainties. I therefore compare the default tune to an alternative tune of GENIE. Section 2.3.3 describes the models used in each of the two tunes. Of note, the alternative tune uses the Nieves model for QE and MEC interactions [55, 56], which does take into account RPA effects and does have associated uncertainties.

This systematic uncertainty is assessed using a multisim approach. The default tune is moved toward the alternative tune by a randomly chosen, one-sided Gaussian distributed amount across 1000 generated universes. Specifically, for each event type (QE or MEC), the ratio of the total cross sections for each tune (shown in Figure 6.2a-b) are treated as normalisation uncertainties, while the ratio of the area-normalised $q^0$ versus $q^3$ distributions (shown in Figure 6.2c-f) are treated as shape uncertainties.

The distribution of the cross sections of the universes is shown in Figure 6.3, along with the distribution of event rates as a function of the track length of the leading MIP candidate and the corresponding covariance and fractional covariance matrices. Note that all of the universe cross sections are lower than the CV cross section because moving the default tune (used in the CV) toward the alternative tune (used in the universes) is essentially a uni-directional effect, as opposed to most other systematics where parameters are both increased and decreased. In total, my choice of models accounts for a systematic uncertainty of 6.27%.

### 6.1.4 Reinteraction Uncertainties

As hadrons propagate through the TPC, they may undergo additional scattering processes with the liquid argon nuclei. Simulation of this is handled by GEANT4 rather than GENIE as in the previous sections, although GENIE is still used to assess the systematic uncertainties. I assess the systematic uncertainties on the hadronic interaction cross section model using a multisim approach, with 100 generated universes.

The reweighting process is described in detail in Ref. [53], but I give an overview here for completeness. At a given energy $E$, the interaction length $\lambda$ of a hadron is given by:

$$\lambda(E) = \frac{1}{\sigma(E) \cdot \rho}, \tag{6.3}$$

where $\sigma(E)$ is the interaction cross section and $\rho$ is the particle density. As a particle travels a small length $\Delta L$ and has a small change in energy $\Delta E$, the chance that the particle "survives" – that is, does not interact – is given by:

$$P_{\text{surv}}(E, E + \Delta E) = e^{-\Delta L/\lambda(E)}. \tag{6.4}$$

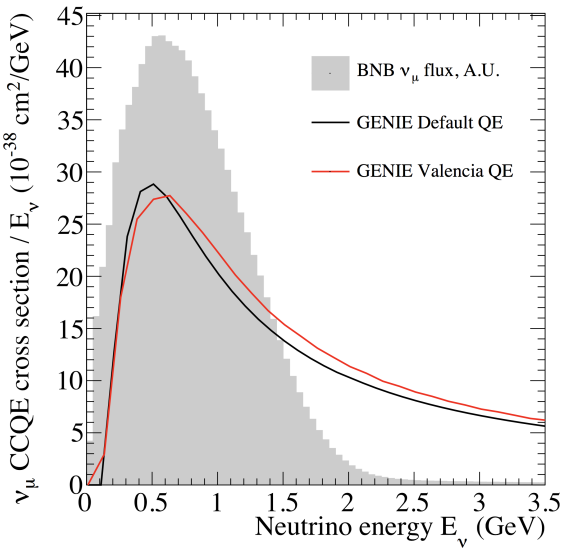


(a) CCQE cross sections

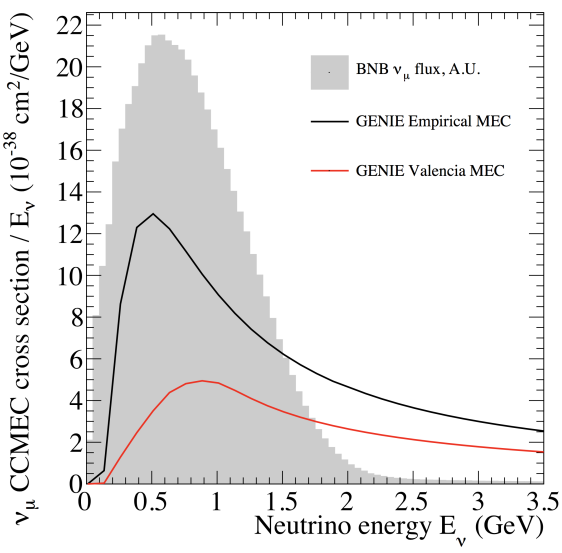


(b) CCMEC cross sections

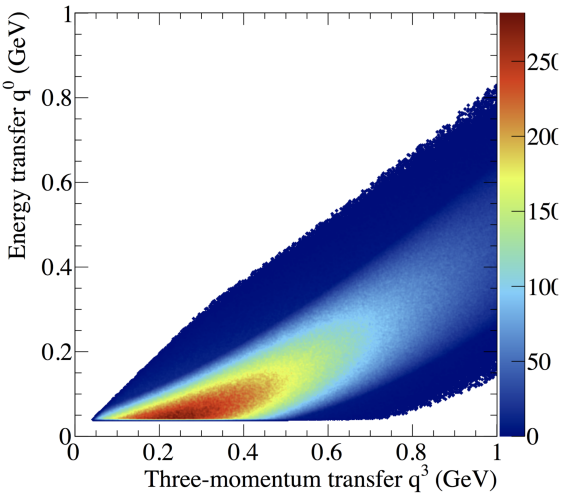


(c) Default tune CCQE kinematics

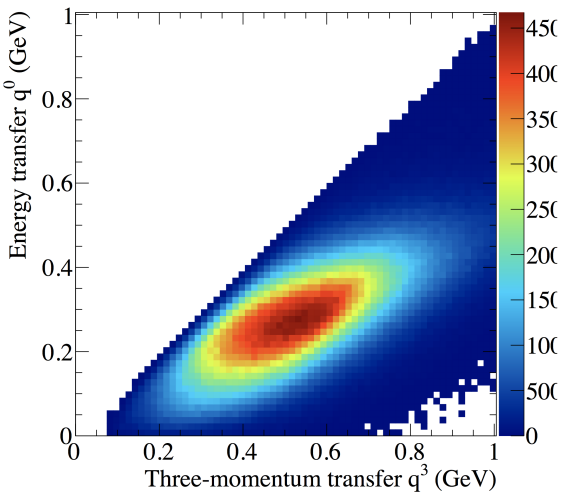


(d) Default tune CCMEC kinematics

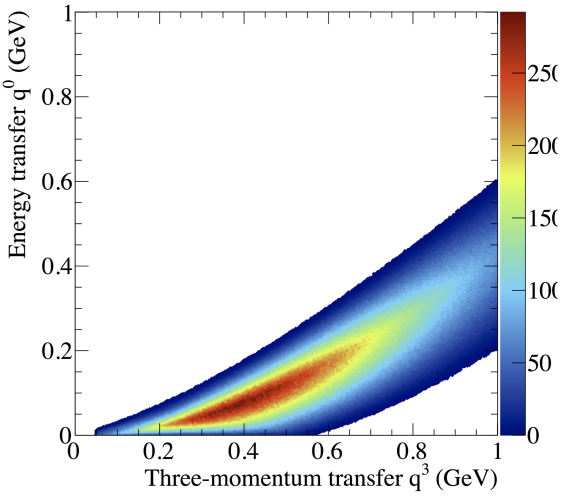


(e) Alternative tune CCQE kinematics

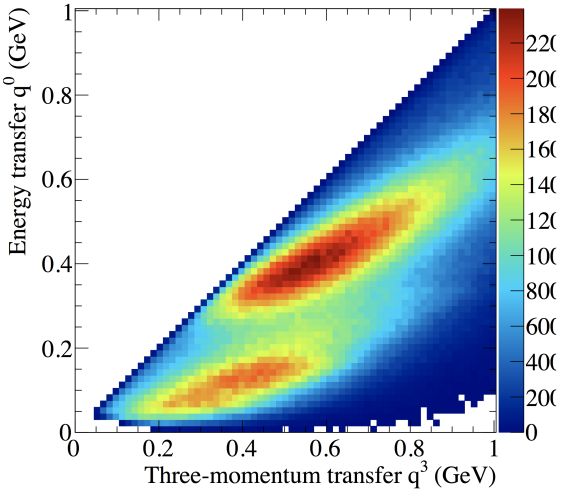


(f) Alternative tune CCMEC kinematics

Figure 6.2: Cross sections and kinematic distributions for CCQE and CCMEC interactions in the default and alternative tunes of GENIE. Figures from Ref. [76].

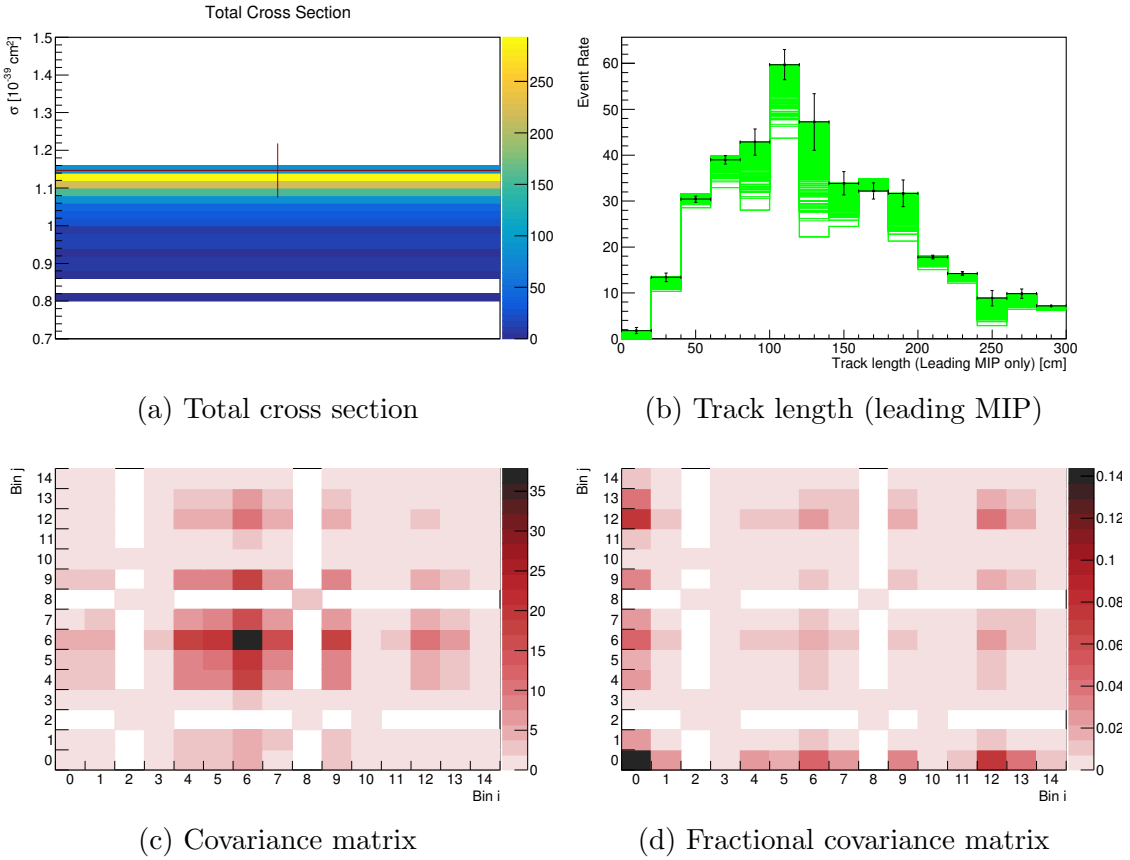


(a) Total cross section

(b) Track length (leading MIP)

(c) Covariance matrix

(d) Fractional covariance matrix

Figure 6.3: Utilising a multisim approach, 1000 universes were generated to assess the choice of model systematic uncertainties. (a): The distributions of their cross sections (CV in red). Error bar shows the total model-related systematic uncertainty. (b): The distribution of event rates as a function of the track length of the leading MIP candidate (CV in black). (c) and (d): Covariance and fractional covariance matrices, respectively.

The total survival probability $P_{\text{surv}}(E_{\text{init}})$ can then be found by multiplying the chances of survival after each distance step. Varying the interaction cross section will give a new universe with $P'_{\text{surv}}(E_{\text{init}})$. Hadrons that do not interact are assigned a weight of

$$w = \frac{P'_{\text{surv}}(E_{\text{init}})}{P_{\text{surv}}(E_{\text{init}})} \tag{6.5}$$

and those that do interact are assigned a weight of

$$w = \frac{1 - P'_{\text{surv}}(E_{\text{init}})}{1 - P_{\text{surv}}(E_{\text{init}})}. \tag{6.6}$$

The distribution of the cross sections of the universes is shown in Figure 6.4, along with the distribution of event rates as a function of the track length of the leading MIP candidate and the corresponding covariance and fractional covariance matrices. In total, hadron reinteractions account for a systematic uncertainty of 1.18%.

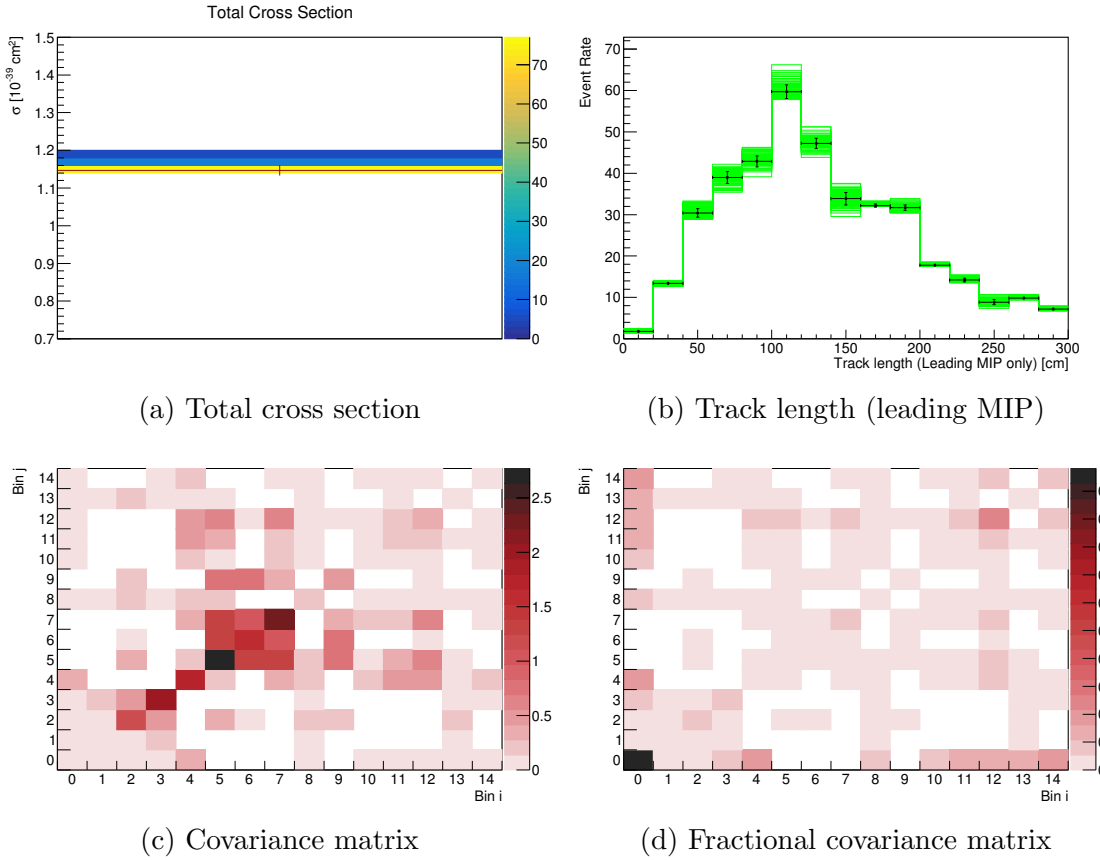


(a) Total cross section

(b) Track length (leading MIP)

(c) Covariance matrix

(d) Fractional covariance matrix

Figure 6.4: Utilising a multisim approach, 100 universes were generated to assess the hadron reinteraction systematic uncertainties. (a): The distributions of their cross sections (CV in red). Error bar shows the total hadron reinteraction-related systematic uncertainty. (b): The distribution of event rates as a function of the track length of the leading MIP candidate (CV in black). (c) and (d): Covariance and fractional covariance matrices, respectively.

## 6.2 Beam Flux Uncertainties

This section describes how I evaluate the uncertainties related to aspects of the beam flux. The parameters I assess fall into two groups: hadron production cross sections, and non-hadron effects. The latter includes the focusing horn current, the focusing horn current depth ("skin effect"), and pion and proton secondary interaction cross sections on aluminium and beryllium. I utilise a multisim approach, varying all of the parameters for 1000 universes. The relative uncertainties on the total cross section for all of the flux systematic parameters are given in Table 6.3.

The distribution of the cross sections of the universes is shown in Figure 6.5, along with the distribution of event rates as a function of the track length of the leading MIP candidate and the corresponding covariance and fractional covariance matrices. In total, beam flux uncertainties account for a systematic uncertainty of 6.10%.

| Flux Parameter | Total Cross Section Relative Uncertainty |
|---|---|
| Non-hadron | 4.73% |
| $K^-$ production cross section | 0.00% |
| $K^+$ production cross section | 0.51% |
| $K^0$ production cross section | 0.00% |
| $\pi^-$ production cross section | 0.22% |
| $\pi^+$ production cross section | 3.44% |
| Total | 6.10% |

Table 6.3: The systematic uncertainty on the total cross section due to each flux parameter, as well as the combined total systematic uncertainty.

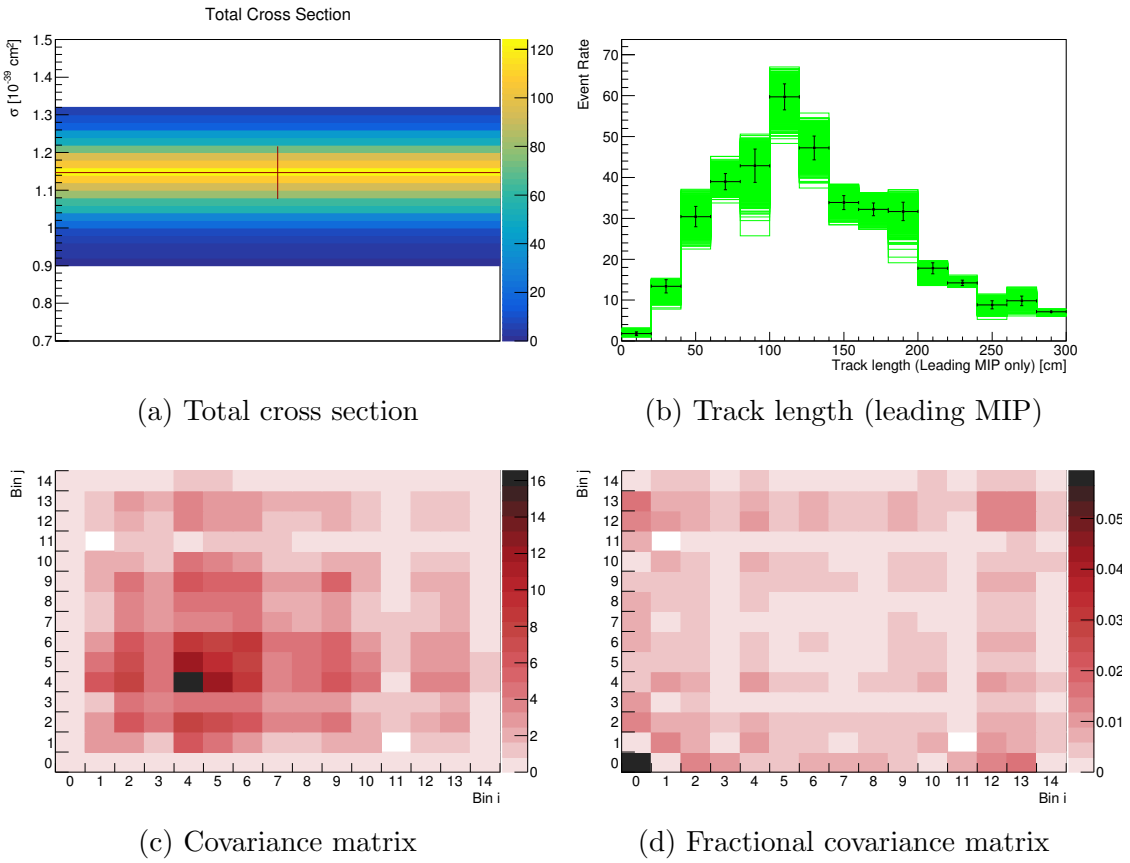


(a) Total cross section

(b) Track length (leading MIP)

(c) Covariance matrix

(d) Fractional covariance matrix

Figure 6.5: Utilising a multisim approach, 1000 universes were generated to assess the beam flux systematic uncertainties. (a): The distributions of their cross sections (CV in red). Error bar shows the total beam flux-related systematic uncertainty. (b): The distribution of event rates as a function of the track length of the leading MIP candidate (CV in black). (c) and (d): Covariance and fractional covariance matrices, respectively.

## 6.3 Detector Uncertainties

This section describes how I evaluate the systematic uncertainties related to aspects of the detector. Here I utilise a unisim approach, wherein each parameter is varied by a set amount and only one parameter is varied at a time. The same generated events are considered for each variation, so as not to introduce additional statistical uncertainty; only the effect of varying each parameter is seen.

For some parameters, a standard deviation is assessed, and I look at both the $\pm 1\sigma$ variations. For the purposes of calculating the total uncertainty, I consider only the larger of the two results. For other parameters, an alternate model or configuration is used, necessitating only one variation. Table 6.4 shows the systematic uncertainty on the total cross section due to each parameter. Figure 6.6 shows the distribution of event rates as a function of the track length of the leading MIP candidate for each parameter. The total systematic uncertainty on the total cross section due to all of the detector effects is 28.42%.

A brief description of each of the parameters considered follows:

**Space Charge Effect** As described in Section 2.3.4, SCE refers to a build-up of slow-moving, positively charged ions in the detector. In this variation I

| Detector Parameter | Total Cross Section Relative Uncertainty |
|---|---|
| Space Charge Effect | 6.29% |
| Light Yield | 9.11% |
| Longitudinal Diffusion (up) | 1.71% |
| Longitudinal Diffusion (down) | 2.54% |
| Transverse Diffusion (up) | 5.29% |
| Transverse Diffusion (down) | 0.91% |
| Wire Noise (up) | 6.63% |
| Wire Noise (down) | 7.71% |
| PMT Noise (up) | 12.69% |
| PMT Noise (down) | 6.94% |
| Wire Response Function | 2.23% |
| Removing misconfigured channels | 3.90% |
| Removing saturated channels | 10.31% |
| Electron Lifetime (up) | 7.08% |
| Electron Lifetime (down) | 11.06% |
| Recombination | 10.98% |
| Light outside TPC | 7.84% |
| Total | 28.42% |

Table 6.4: The systematic uncertainty on the total cross section due to each detector effect, as well as the combined total systematic uncertainty due to all of the detector effects. In the case of up/down variations, only the larger of the two is considered when calculating the total uncertainty.

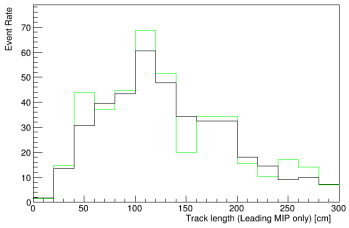


(a) SCE

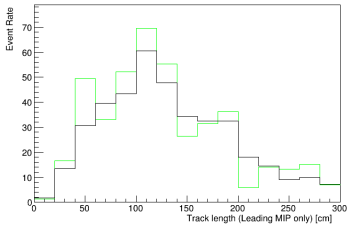


(b) Light Yield

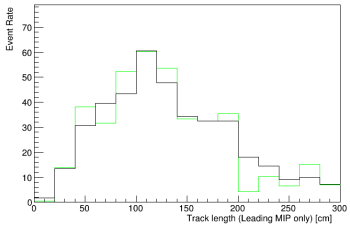


(c) Long. Diffusion (up)

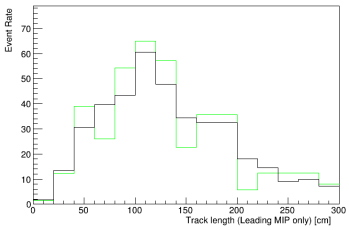


(d) Long. Diffusion (down)

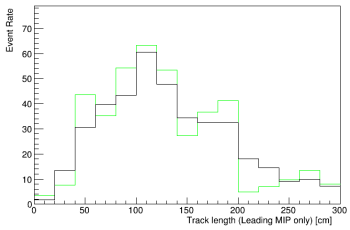


(e) Trans. Diffusion (up)

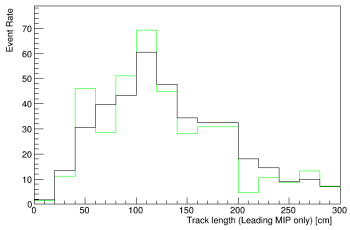


(f) Trans. Diffusion (down)

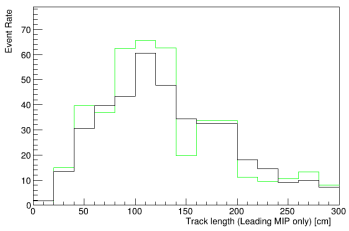


(g) Wire Noise (up)

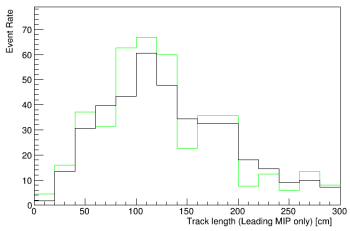


(h) Wire Noise (down)

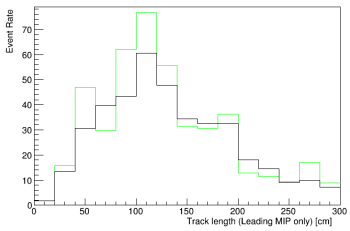


(i) PMT Noise (up)

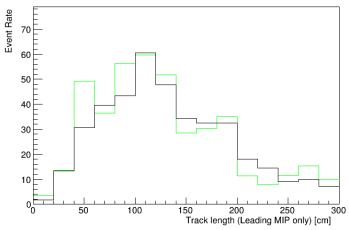


(j) PMT Noise (down)

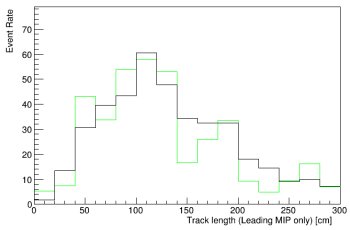


(k) Wire Response Function

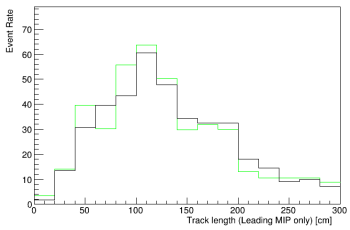


(l) Remove misc. channels

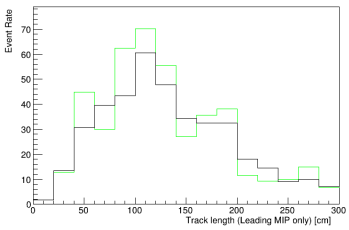


(m) Remove sat. channels

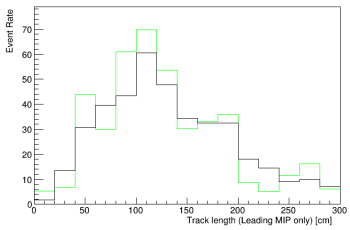


(n) Electron LT (up)

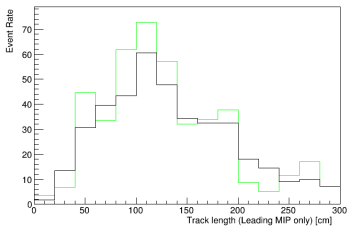


(o) Electron LT (down)

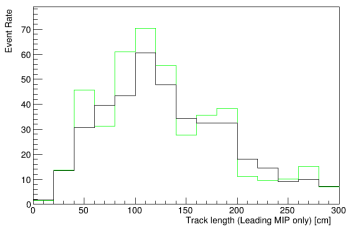


(p) Recombination

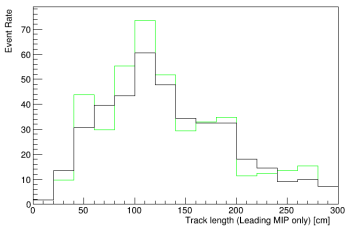


(q) Light outside TPC

Figure 6.6: For each of the detector-related uncertainty parameters, the distribution of event rates as a function of the track length of the leading MIP candidate (green), with the CV (black) for comparison.

apply a data-driven correction to the central value simulation in order to better replicate what is measured [66]. This involves reducing the strength of the electric field distortions to 70% of the nominal value, as well as applying a scale factor (dependent on the position along the drift direction) to the extent of the spatial charge migration.

**Light Yield** A number of bugs were found in the model of scintillation light production used in the central value simulation. The primary bug is that all particle types are treated as electrons when determining the number of photons produced per unit energy deposited. In this variation I use an updated version of the simulation where these bugs have been fixed.

**Longitudinal and Transverse Diffusion** Ionisation electrons diffuse as they drift toward the wire planes. This occurs both longitudinally (parallel to the TPC electric field) and transversely (perpendicular to it). In these variations I vary the strength of these effects based on Refs. [84–86].

**Wire Noise** The amplitude of the simulated noise on the TPC wires is varied, based on MicroBooNE's measurement detailed in Ref. [69].

**PMT Noise** The rate of simulated noise from single photoelectrons on the PMTs is varied based on MicroBooNE data.

**Wire Response Function** Charge induction on the TPC wires is simulated by a set of response functions, as described in Ref. [68]. In this variation these functions are "squeezed" by 20%, meaning the time extent of the responses is reduced by 20% while keeping the peak time unchanged.

**Removing misconfigured channels** Channels that are associated with misconfigured application-specific integrated circuits (ASICs) are removed. This exaggerates the size of this effect, providing an upper bound.

**Removing saturated channels** Channels that are prone to saturation are removed. This exaggerates the size of this effect, providing an upper bound.

**Electron Lifetime** Due to small impurities in the LAr, drift electrons may sometimes interact before reaching the sense wires, leading to an attenuation of the signal. The half life of these electrons is referred to as electron lifetime. The simulated electron lifetime in the central value sample is a constant 10 ms. In this variation I instead vary the lifetime based on MicroBooNE data.

**Recombination** The central value simulation uses the modified box model of electron-ion recombination, with parameters tuned to ArgoNeuT data. This variation instead uses the Birks model, with parameters tuned to ICARUS data.

**Light outside TPC** Light production outside the TPC may not be well-modelled. In this variation I increase the amount of light produced outside the TPC by 50%.

One known effect not considered here is known as dynamic induced charge (DIC). As described in Section 2.3.4, this refers to ionisation electrons inducing charge on multiple sense wires to either side of them, rather than on only the closest wires as is assumed by the nominal simulation. This effect has a large impact on this analysis, and I therefore do not think it makes sense to treat it as a systematic uncertainty. Instead, I use a preliminary version of the next generation of the simulation, which includes the DIC effect, to produce a new baseline simulation. All systematic uncertainties are then applied to it to produce my final cross section result. This process is described in further detail in Section 7.1.

## 6.4 POT Counting Uncertainty

The primary proton beam's intensity is measured using two toroids. Measurements done by MiniBooNE show that the flux measured by the toroids agrees to within 2% of each other [47]. I treat this as an uncorrelated normalisation uncertainty on the total cross section.

## 6.5 Simulated Dirt Uncertainty

It is possible for an interaction that starts outside of the cryostat to enter it and for the event to then be selected. These are known as dirt events, and they are included in the simulation and my analysis. However, this background depends strongly on the makeup of the materials surrounding MicroBooNE and on GENIE's ability to simulate interactions with them. I therefore conservatively assign a 100% normalisation uncertainty to these events. This amounts to a systematic uncertainty on the total cross section of 5.39%.

## 6.6 Simulated Cosmic Uncertainty

The simulated in-time cosmic background may be different from the true one. Unfortunately, the CORSIKA simulation used for this does not have associated uncertainties. I therefore currently take a conservative 100% normalisation uncertainty on these events. This amounts to a 11.01% systematic uncertainty on the total cross section due to these events.

A different approach to assessing uncertainties on these events is a topic of future work (see Section 8.3). It has been proposed that out of time cosmic events from data may be overlaid on top of simulated BNB neutrino events, which would remove the need to simulate cosmic events at all. To stress, this approach has not been used in this analysis.

## 6.7 Number of Target Nucleons Uncertainty

The number of target nucleons in the fiducial volume is given by:

$$T = \frac{\rho_{\mathrm{Ar}} \cdot V \cdot N_A \cdot N_{\mathrm{nucl}}}{m_{\mathrm{mol}}} \tag{6.7}$$

where $\rho_{\mathrm{Ar}}$ is the density of liquid argon, $V$ is the fiducial volume, $N_A$ is Avogadro's number, $N_{\mathrm{nucl}}$ is the number of nucleons per argon nucleus, and $m_{\mathrm{mol}}$ is the molar mass of argon. Their values are as follows:

$$\begin{aligned}
\rho_{\mathrm{Ar}}^{\mathrm{data}} &= 1.3836 \text{ g/cm}^3 \\
\rho_{\mathrm{Ar}}^{\mathrm{MC}} &= 1.3954 \text{ g/cm}^3 \\
V &= 3.131346 \times 10^7 \text{ cm}^3 \\
N_A &= 6.02214076 \times 10^{23} \text{ particles/mol} \\
N_{\mathrm{nucl}} &= 40 \\
m_{\mathrm{mol}} &= 39.95 \text{ g/mol},
\end{aligned} \tag{6.8}$$

which leads to results of:

$$\begin{aligned}
T_{\mathrm{data}} &= 2.6124 \times 10^{31} \\
T_{\mathrm{MC}} &= 2.6347 \times 10^{31}.
\end{aligned} \tag{6.9}$$

Comparing these two values yields a systematic uncertainty of 0.85% due to the different values of the density used in the simulation and later measured in data.

$\rho_{\mathrm{Ar}}$ was measured in data using sensors that monitored the temperature and pressure of the detector. The precision of the sensors and slight changes in the pressure over time result in a relative uncertainty on $\rho_{\mathrm{Ar}}^{\mathrm{data}}$ of 0.14%.

These two uncertainties are uncorrelated, so I add them in quadrature and find the total relative systematic uncertainty on the cross section, due to estimating the number of targets, to be 0.86%.

## 6.8 Summary

This chapter has described the sources of systematic uncertainty that affect this analysis and the ways in which I estimate them. A multisim approach, wherein all parameters are reweighted at the same time to produce a set a universes, is used for the cross section modelling, QE and MEC model choice, hadronic reinteraction, and beam flux uncertainties. The detector response uncertainty is instead assessed with a unisim approach, wherein each parameter is individually reweighted. Additional sources of uncertainty include POT counting, simulated dirt background, simulated

cosmic background, and the number of target nucleons. The results for each are summarised in Table 6.5. I consider all of these uncertainties to be uncorrelated, and may therefore sum them in quadrature to find that the total relative systematic uncertainty on the cross section is 33.16%.

| Uncertainty Source | Total Cross Section Relative Uncertainty |
|---|---|
| Cross Section Modelling | 7.68% |
| QE/MEC Model Choice | 6.27% |
| Hadronic Reinteraction | 1.18% |
| Beam Flux | 6.10% |
| Detector Response | 28.42% |
| POT Counting | 2% |
| Simulated Dirt Background | 5.39% |
| Simulated Cosmic Background | 11.01% |
| Number of Target Nucleons | 0.86% |
| Total | 33.16% |

Table 6.5: The relative systematic uncertainty on the total cross section due to each source of uncertainty, as well as the combined total relative systematic uncertainty due to all sources.

# Chapter 7

# Cross Section Analysis

This chapter describes the final cross section analysis. Section 7.1 outlines how I handle the DIC effect in the calculation of the cross section. Section 7.2 presents the main result itself and compares it to the prediction from GENIE.

## 7.1 Dynamic Induced Charge

As described previously in Section 2.3.4, there exists a known detector effect in MicroBooNE called dynamic induced charge (DIC). When ionisation electrons pass by the wire planes, they induce charge on multiple sense wires to either side: $\pm 10$ on the first induction plane and $\pm 2$ on the second induction plane and on the collection plane [67]. The nominal version of the simulation used in this analysis does not simulate this, instead assuming that charge is only induced on the closest wire. The main result of this effect is to broaden the distribution of dE/dx.

As mentioned in Section 6.3, one way to account for this would be to assess it as a systematic uncertainty. However, this analysis is strongly impacted by the difference, and so I felt this was not the best solution. Instead, I use a preliminary version of the next generation of the simulation, which does include DIC, to produce a new baseline sample. I then use this new sample for my estimates of the number of selected background events and of selection efficiency and purity when extracting the cross section.

Systematic uncertainties are assessed using variations from the nominal simulation, as described in Chapter 6. Both DIC and all of the effects considered there are independent of one another. I am therefore able to keep the relative systematic uncertainties and apply them to the cross section extracted with the DIC sample.

## 7.2 Results

The total, flux-integrated cross section $\sigma$ is given by:

$$\sigma = \frac{N - B}{\epsilon \cdot \Phi_{\nu_\mu} \cdot T} \tag{7.1}$$

where $N$ is the total number of selected events, $B$ is the number of selected background events, $\epsilon$ is the signal selection efficiency, $\Phi_{\nu_\mu}$ is the integrated BNB muon neutrino flux, and $T$ is the number of target nucleons. Since the number of background events in data is not known, it must be estimated from MC. However, as noted in Section 5.8, there is a clear normalisation difference between the two in this analysis, with MC being higher. Using this equation would thus effectively be making an over-estimate of the number of background events in data and would lead to a clearly incorrect result. I therefore instead use the form:

$$\sigma = \frac{N \cdot \rho}{\epsilon \cdot \Phi_{\nu_\mu} \cdot T} \tag{7.2}$$

where $\rho$ is the purity of the event selection. Here the background is estimated as a proportion of the total number of selected events instead of as an absolute event count, thus eliminating the reliance on normalisation agreement. Note that if the two normalisations did agree, these equations would be equivalent.

In order to apply this in a consistent manner, $N$ and $\rho$ must be calculated carefully. The MC is split into two samples: the main MC sample, which contains on-beam events inside the TPC, plus a secondary sample used to estimate the dirt background. The data is also split into two samples: on-beam and off-beam. The comparable event rates in MC and data are thus:

$$N^{\mathrm{MC}} = N^{\mathrm{MC}}_{\mathrm{main}} + B^{\mathrm{MC}}_{\mathrm{dirt}} \tag{7.3}$$

and

$$N^{\mathrm{data}} = N^{\mathrm{data}}_{\text{on-beam}} - N^{\mathrm{data}}_{\text{off-beam}} \tag{7.4}$$

where $N^{\mathrm{MC}}$ and $N^{\mathrm{data}}$ are the comparable total number of selected events in MC and data respectively, $N^{\mathrm{MC}}_{\mathrm{main}}$ is the number of selected events in the main MC sample, $B^{\mathrm{MC}}_{\mathrm{dirt}}$ is the number of selected events in the dirt background MC sample, $N^{\mathrm{data}}_{\text{on-beam}}$ is the number of selected events in the on-beam data sample, and $N^{\mathrm{data}}_{\text{off-beam}}$ is the number of selected events in the off-beam data sample. The purity is then given by:

$$\rho = \frac{N^{\mathrm{MC}} - \left(B^{\mathrm{MC}}_{\mathrm{main}} + B^{\mathrm{MC}}_{\mathrm{dirt}}\right)}{N^{\mathrm{MC}}} \tag{7.5}$$

where $B^{\text{MC}}_{\text{main}}$ is the number of selected background events in the main MC sample. Table 7.1 gives the number of selected events for each of these samples, including a breakdown of the backgrounds in the main MC sample, while Table 7.2 lists the values of the other parameters used to calculate the cross section.

| Name | Variable | Events |
|---|---|---|
| Total selected on-beam data | $N^{\text{data}}_{\text{on-beam}}$ | $523 \pm 23$ |
| Total selected off-beam data | $N^{\text{data}}_{\text{off-beam}}$ | $89.6 \pm 6.8$ |
| Total selected MC | $N^{\text{MC}}$ | $647.4 \pm 23.7$ |
| Signal | - | $342.2 \pm 17.5$ |
| Main backgrounds | $B^{\text{MC}}_{\text{main}}$ | $282.1 \pm 15.9$ |
| Cosmic | - | $15.7 \pm 3.8$ |
| Mixed | - | $31.4 \pm 5.3$ |
| Out of FV | - | $34.2 \pm 5.5$ |
| Multi-$\nu$ | - | $0.0 \pm 0.0$ |
| $\nu_\mu$ CC0$\pi$ | - | $113.8 \pm 10.1$ |
| $\nu_\mu$ CC1$\pi^+$ Bad Angle | - | $12.0 \pm 3.3$ |
| $\nu_\mu$ CC1$\pi^-$ | - | $5.5 \pm 2.2$ |
| $\nu_\mu$ CC1$\pi^0$ | - | $20.3 \pm 4.3$ |
| $\nu_\mu$ CC $>1\pi$ | - | $33.3 \pm 5.5$ |
| $\nu_\mu$ CC Other | - | $0.0 \pm 0.0$ |
| $\nu_e$ CC | - | $0.9 \pm 0.9$ |
| NC | - | $14.8 \pm 3.6$ |
| Dirt background | $B^{\text{MC}}_{\text{dirt}}$ | $23.1 \pm 1.2$ |

Table 7.1: Number of selected events, used to calculate the total cross section. All values are scaled to the on-beam data POT of $1.763 \times 10^{20}$. Uncertainties are statistical only.

| Name | Variable | Value |
|---|---|---|
| Efficiency | $\epsilon$ | $0.0836 \pm 0.0045$ |
| Purity | $\rho$ | $0.5286 \pm 0.0333$ |
| BNB $\nu_\mu$ flux | $\Phi_{\nu_\mu}$ | $1.331 \times 10^{11}$ cm$^{-2}$ |
| Number of targets (data) | $T^{\text{data}}$ | $2.6124 \times 10^{31}$ |
| Number of targets (MC) | $T^{\text{MC}}$ | $2.6347 \times 10^{31}$ |

Table 7.2: Parameters used to calculate the total cross section. The flux corresponds to $1.763 \times 10^{20}$ POT. Uncertainties are statistical only. The flux and number of targets are taken to have negligible statistical uncertainties.

Using these values with Equation 7.2, I find that the total, flux-integrated CC1$\pi^+$ cross section on argon per nucleon is:

$$\sigma_{\mathrm{CC1}\pi^+} = 0.788 \pm 0.079\ (\mathrm{stat.}) \pm 0.261\ (\mathrm{syst.}) \times 10^{-39}\ \mathrm{cm}^2.$$

Figure 7.1 shows a comparison of this value with the MC prediction, from GENIE. The prediction is about 1.4 standard deviations higher than the measured value. The main cause of the disagreement is found to be the selection cut on the opening angle of the muon and pion candidates, as described in Section 5.5. This cut was motivated by a desire to reduce the number of selected background events wherein a single true particle is misreconstructed as two tracks that are close to back-to-back.

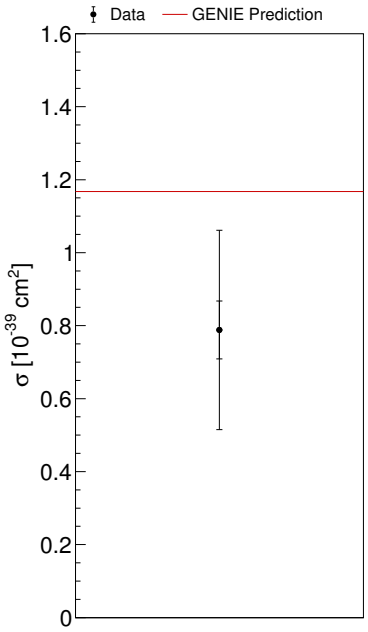


Figure 7.1: The measured total, flux-integrated CC1$\pi^+$ cross section on argon per nucleon (black point), compared with the prediction from GENIE MC (red line). The inner bars show the statistical uncertainty, while the outer bars show the sum of the statistical and systematic uncertainties.

This cut was justified in three ways. First, a truth study was performed that showed that the vast majority of high opening angle tracks are indeed due to track breaking in reconstruction. Second, ArgoNeuT measurement and generator predictions of the cross section as a function of opening angle [34] (see Figure 5.25) showed that there was a low cross section in the region I intended to cut, which suggested that even a large deviation between these values and MicroBooNE data in this area of phase space would not significantly affect the analysis as a whole. Third, the ArgoNeuT analysis had the same issue with track breaking misreconstructions and employed a similar cut to ameliorate it. Specifically, events with the largest angle between the muon track and any other track above 170 degrees ($\approx$ 2.97 rad) were

cut. The main difference between this and the cut I would eventually use is that they were able to cut more tightly (2.6 rad $\approx$ 149 degrees is used in my analysis).

Unfortunately, this reasoning did not prove to be sufficient. Figure 7.2 shows the distribution of opening angles for selected events, at the point in the selection right before and then after the cut on it is applied. MC and data are actually found to agree well in overall normalisation beforehand. However, these events are distributed toward higher opening angles in data. A cut on this variable thus leads to much worse normalisation agreement, as more events are cut from data than MC.

To clarify a point, while Equation 7.2 has been used due to the normalisation difference, it does not completely mitigate it. Fewer events are selected in data, and consequently the cross section is also lower for data, as one would expect. The purity correction serves only to ensure that the estimate of the number of background events that have been selected is more accurate.

There are, broadly speaking, two main possible reasons for the disagreement in opening angle distribution. The simplest explanation is that some feature of the data that differs from simulation leads to more broken track misreconstructions. However, it is also possible that it is due to a real physics effect. Nuclear effects and final state interactions (FSI) are a significant factor in interactions like these that involve heavy nuclei, and our understanding of them is very much an area of active research. Looking at this result in the context of other similar measurements (see Section 1.2), it is notable that GENIE over-predicted the normalisation for the T2K and ArgoNeuT results as well. Specifically, the GENIE prediction for the total CC1$\pi^+$ cross section was $2\sigma$ higher than T2K's measurement on water [32] and $3.3\sigma$ higher than ArgoNeuT's measurement on argon [34]. This serves as evidence of true disagreement between the physics and GENIE's implementation of it. Future versions of this analysis should aim to investigate this, as further discussed in Section 8.2.

While it is tempting to remove or modify the opening angle cut to achieve better data-MC agreement, it cannot be said for certain at this point which of the two effects is the cause. For the time being, I feel that it is better science to present the result as-is, rather than assume a particular answer.

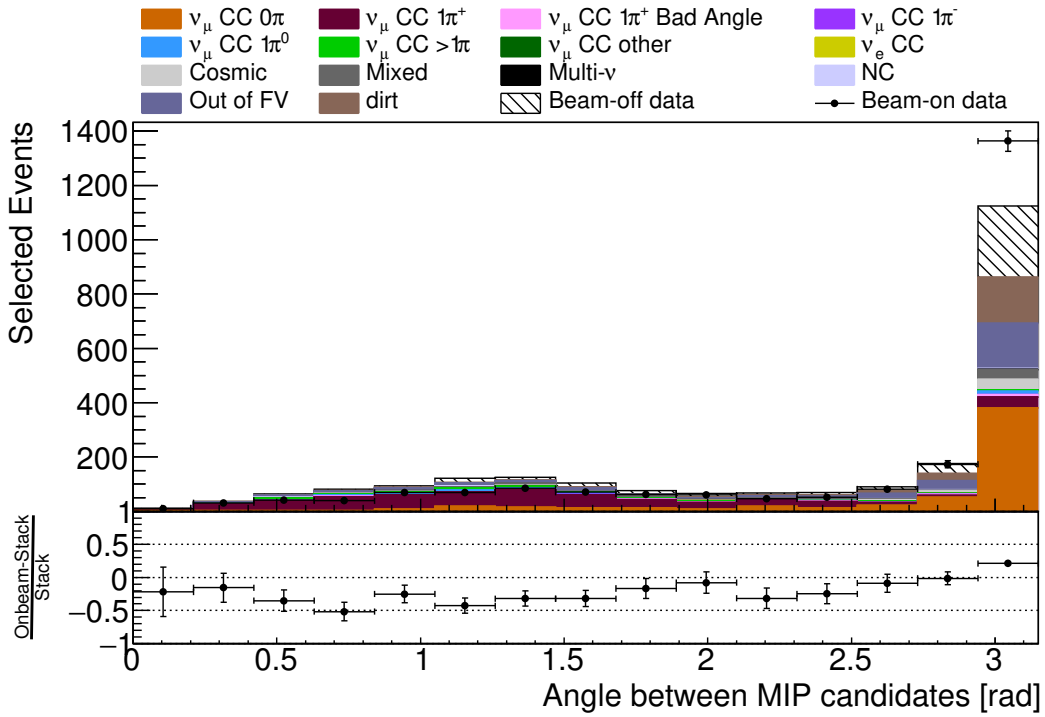


(a) Before cut.

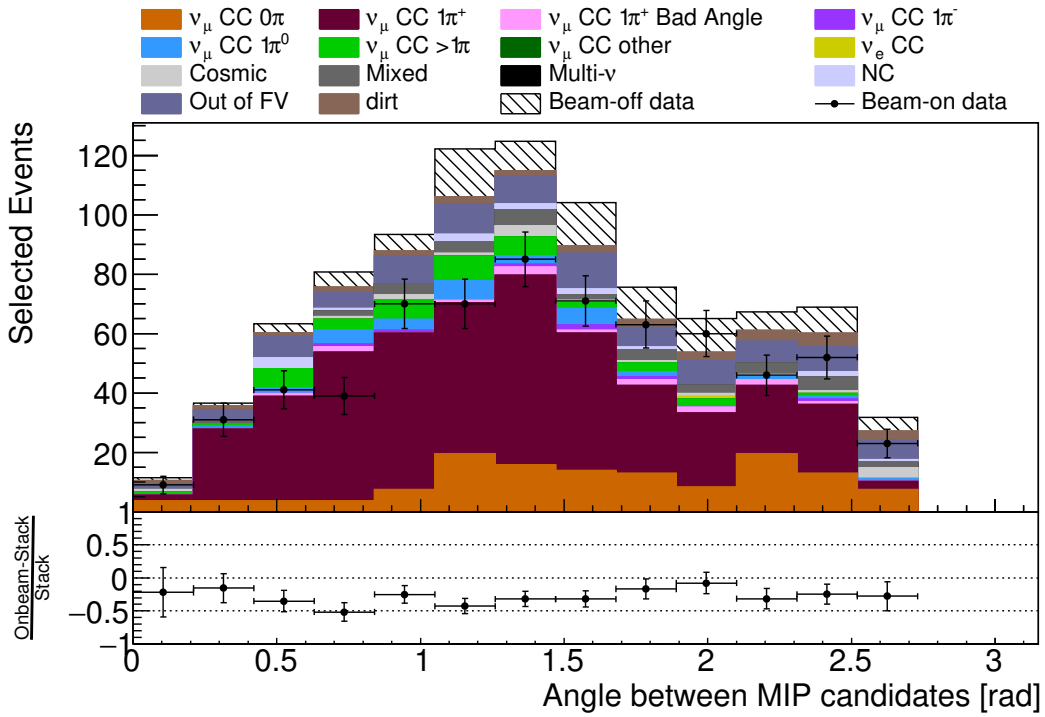


(b) After cut.

Figure 7.2: Distribution of opening angles, i.e. the angle between the two MIP candidates, (a) before and (b) after applying a cut at 2.6 radians. The MC sample used here includes simulation of the DIC effect.

# Chapter 8

# Future Work and Improvements

In science, no work is ever perfect or complete, and this analysis is no different. This chapter goes over several specific areas where I expect to see this analysis improved or expanded upon. Section 8.1 describes improvements related to the simulation of the DIC effect, Section 8.2 discusses the opening angle selection cut and how it may be further investigated in future analyses, Section 8.3 outlines a novel technique for estimating certain cosmic backgrounds, and Section 8.4 puts forward some possible methods of separating muons and pions, for the purposes of future differential cross section measurements.

## 8.1 Dynamic Induced Charge Simulation

As described in Section 2.3.4, dynamic induced charge (DIC) is a detector effect in MicroBooNE, wherein ionisation electrons induce charge on a number of wires to either side of them as they pass by the wire planes. This effect is not currently simulated, and instead it is assumed that charge is only induced on the closest wire. The main result of the effect is to broaden dE/dx distributions. This has a large impact on this analysis in particular. As described in Section 7.1, a preliminary version of the next generation of the simulation, which does include DIC, was used for the cross section extraction.

Broadly speaking, future analyses will be improved because the simulation will be more accurate. There are two main ways in which this will manifest. First, they will be able to use the final version of the next generation of the simulation. More improvements will be included and more rigorous testing will have been done to ensure intended behaviour. Second, the selection used in this analysis was developed by looking at events and distributions that did not include DIC. It is likely that the cut values and BDT training used here could be better optimised with the new events. It is also possible that the selection may be changed more significantly if different variables are now found to be suitable.

## 8.2 Opening Angle Selection Cut

As described in Section 5.5, one stage of the selection involves cutting on the opening angle between the muon and pion candidates. This cut was motivated by a desire to reduce the number of selected background events wherein a single true particle is misreconstructed as two tracks that are close to back-to-back.

Section 7.2 includes a discussion of the justification for the cut, why it led to data-MC disagreement, and why the cut remains in this analysis. In brief, the justifications included a truth study showing that the vast majority of high opening angle events are due to misconstruction; the fact that ArgoNeuT measured the cross section in the cut region to be low; and the fact that the ArgoNeuT selection used a similar cut for the same issue [34]. Unfortunately, the distribution of opening angles in data and MC wound up differing, with data peaked toward higher angles. This meant that the total normalisation agreement, which was good before the cut, was significantly worse after it. This is most likely due, at least in part, to there being some feature of data that differs from the simulation and leads to more misreconstructions. However, it is also possible that the disagreement is due to the true physics, especially in light of the fact that nuclear effects and final state interactions (FSI) significantly affect CC1$\pi^+$ interactions, but our understanding of them is incomplete and an active area of research. As the extent to which these two factors were the cause is not known, I chose to keep this cut in place for this analysis.

Future analyses, however, will work to better understand this disagreement. There are several ways in which the handling of this variable could be improved:

The reconstruction may be improved so that fewer tracks are improperly broken. This would lessen the need for a cut on opening angle, or perhaps allow for a tighter cut value to be used.

Only a small sample of data was made available during the development of this selection, in order to avoid bias. A much larger sample of data events that were removed by this cut may now be investigated. This will allow for a better understanding of whether these events are mostly misreconstructed, as in MC. It will also enable analysers to determine what characteristics of these events (if any) differ between data and MC and may be leading to a difference in their prevalence.

As described in the previous section, the DIC simulation used here is preliminary, as the final implementation was not yet available. This, as well as other changes in the next generation of the simulation, may lead to better agreement with data.

Overall, future analyses will be able to better understand the differences in this distribution. Differences that are due to reconstruction or simulation issues can be reduced or eliminated. Any disagreement that remains can then be said more

confidently to likely be due to real physics.

## 8.3 Cosmic Ray Simulation

As described in Section 2.3.2, an important background for all MicroBooNE analyses comes from cosmic rays (CRs). Data can be recorded with the neutrino beam off in order to measure the rate of them, which can then be subtracted. However, there also exist events with both neutrinos and CRs present, where it is possible to select the CR interaction instead of the neutrino interaction, or a combination of both due to reconstruction confusion. These backgrounds must be simulated, for which this analysis uses the CORSIKA generator. Unfortunately, it does not provide associated uncertainties, and I am forced to use a conservative over-estimate, which contributes significantly to the total systematic uncertainty (see Section 6.6).

Future analyses plan to use a different, first of its kind approach. MicroBooNE has collected a large sample (over $10^{21}$ POT equivalent) of beam-off CR data. Rather than relying on CR simulation for the determination of the CR+neutrino event backgrounds, this sample may be leveraged to construct events with simulated beam neutrino interactions and real CRs from data [87]. These combined events are referred to as "overlays." An example is shown in Figure 8.1.

This approach is not without its complications, such as how to calibrate the

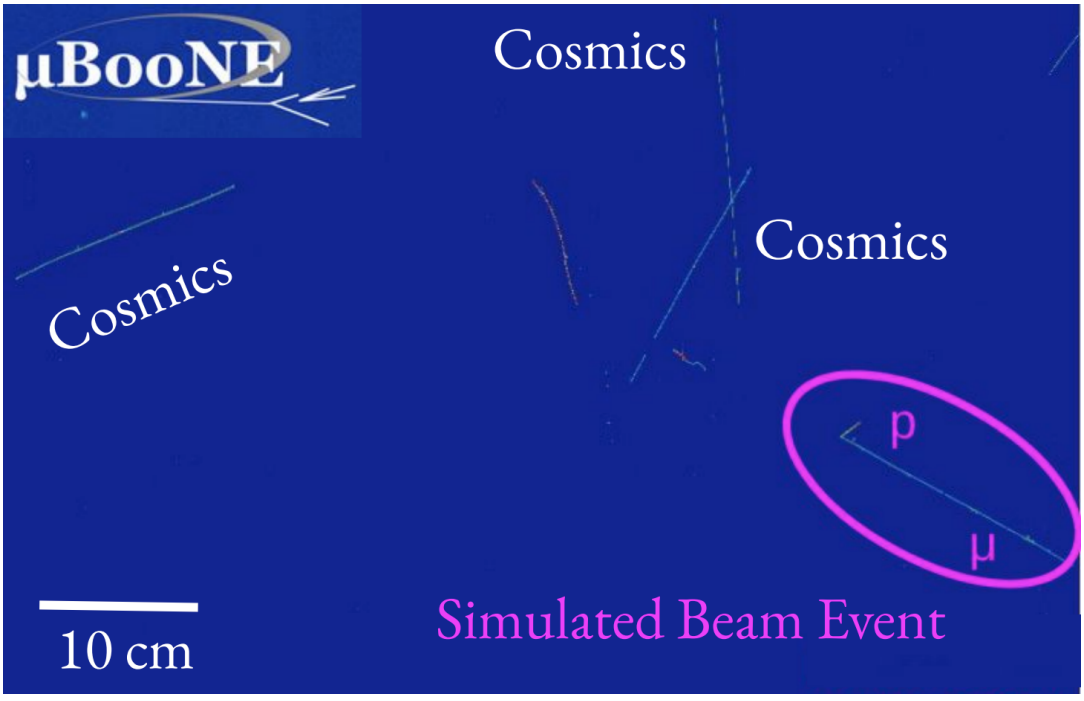


Figure 8.1: An event display showing an example of an overlay event. Cosmic tracks from real off-beam data have been overlaid with a simulated beam event, circled in magenta. Figure from Ref. [88].

energy depositions, as this is currently done separately for MC and data. However, it will offer a number of advantages. First, these backgrounds will of course be closer to real data. A few specific ways that this is true include: the overlay sample will include CRs with energy below 100 MeV, which are not simulated; the overlay noise estimation is closer to that observed in data; and the CR background close to the edges of the detector is bettered matched by overlays. The other main advantage is that overlays will allow for a better evaluation of the systematic uncertainty of the estimation of these backgrounds. In this analysis, these backgrounds are the second highest contributor to the total systematic uncertainty, which can potentially be reduced significantly with overlays.

## 8.4 Muon-Pion Separation

This analysis includes only a total cross section measurement, and as such it is not strictly necessary that the MIP candidates be further separated into a muon candidate and a pion candidate. However, differential cross sections as a function of muon and pion kinematics are an obvious next step for future analyses. Muons and pions have nearly identical dE/dx profiles, which makes them difficult to separate in MicroBooNE since it lacks a magnet to separate them by charge. Section 5.7 gives a benchmark of how well I am able to separate them right now, using only some simple criteria. I find that in 86.2% of true signal events, I am able to label both the true muon and true pion correctly. This is a good starting point, but can be improved.

One possible avenue is to use a second BDT classifier. As the available one-dimensional distributions are very similar, it is difficult to achieve a high level of precision with simple box cuts. BDTs are a useful tool in situations like this, since they can effectively make cuts in the multidimensional phase space.

Another option involves exploiting the fact that pions are much more likely to re-interact in the detector than muons are. These hadronic interactions result in a change in direction, seen as a "kinked" track. MiniBooNE successfully employed this strategy by developing a kinked pion fitter [28]. In addition to providing muon-pion separation, this had the added benefit of improving the measurement of pion kinematics.

# Chapter 9

# Conclusions

There are many open questions about the properties of neutrinos and their interactions. Excitingly, the current and next generation of oscillation experiments intend to be able to provide some of the answers, such as what the mass hierarchy is, and the extent to which there is CP violation in the lepton sector. One of the larger remaining stumbling blocks to this goal is an incomplete understanding of neutrino interactions with heavy nuclei. Nuclear effects and final state interactions clearly play a significant role, but their modelling is an ongoing effort. Additional neutrino cross section measurements are a necessary input to further inform them. MicroBooNE is making significant contributions, with the measurement of neutrino-argon cross sections being one of its primary objectives.

MicroBooNE is also the first large liquid argon time projection chamber (LArTPC) to gather high statistics neutrino data, having done so from 2015-2021. Many future experiments, including SBND, ICARUS, and DUNE, also plan to use this technology. MicroBooNE has provided invaluable experience for these experiments and has shown the high precision imagining capabilities of LArTPCs.

This thesis has presented the first measurement of single charged pion production in MicroBooNE. Using data corresponding to $1.763 \times 10^{20}$ POT, I find that the total flux-integrated CC1$\pi^+$ cross section on argon per nucleon is $0.788 \pm 0.090$ (stat.) $\pm$ $0.261$ (syst.) $\times 10^{-39}$ cm$^2$. This is somewhat lower than the prediction from Genie, which is consistent with the findings of T2K and ArgoNeuT for this channel.

Future analyses will be able to build upon this work in several ways. The source of the disagreement can be investigated in further detail. Improvements to the simulation and reconstruction will result in better agreement with data, in particular by fully simulating the DIC effect. Systematic uncertainties may be reduced by using a different method to estimate in-time cosmic backgrounds. And finally, methods of better separating muons and pions may be developed, allowing for the measurement of kinematic differential cross sections.

# Bibliography

[1] A. A. Aguilar-Arevalo et al. "Significant Excess of ElectronLike Events in the MiniBooNE Short-Baseline Neutrino Experiment". In: *Phys. Rev. Lett.* 121.22 (2018), p. 221801. DOI: 10.1103/PhysRevLett.121.221801. arXiv: 1805.12028 [hep-ex].

[2] Georges Aad et al. "Observation of a new particle in the search for the Standard Model Higgs boson with the ATLAS detector at the LHC". In: *Phys. Lett. B* 716 (2012), pp. 1–29. DOI: 10.1016/j.physletb.2012.08.020. arXiv: 1207.7214 [hep-ex].

[3] Serguei Chatrchyan et al. "Observation of a New Boson at a Mass of 125 GeV with the CMS Experiment at the LHC". In: *Phys. Lett. B* 716 (2012), pp. 30–61. DOI: 10.1016/j.physletb.2012.08.021. arXiv: 1207.7235 [hep-ex].

[4] Y. Fukuda et al. "Evidence for oscillation of atmospheric neutrinos". In: *Phys. Rev. Lett.* 81 (1998), pp. 1562–1567. DOI: 10.1103/PhysRevLett.81.1562. arXiv: hep-ex/9807003.

[5] Q. R. Ahmad et al. "Direct evidence for neutrino flavor transformation from neutral current interactions in the Sudbury Neutrino Observatory". In: *Phys. Rev. Lett.* 89 (2002), p. 011301. DOI: 10.1103/PhysRevLett.89.011301. arXiv: nucl-ex/0204008.

[6] C. Anderson et al. "The ArgoNeuT Detector in the NuMI Low-Energy beam line at Fermilab". In: *JINST* 7 (2012), P10019. DOI: 10.1088/1748-0221/7/10/P10019. arXiv: 1205.6747 [physics.ins-det].

[7] R. Acciarri et al. "Design and Construction of the MicroBooNE Detector". In: *JINST* 12.02 (2017), P02017. DOI: 10.1088/1748-0221/12/02/P02017. arXiv: 1612.05824 [physics.ins-det].

[8] S. Amerio et al. "Design, construction and tests of the ICARUS T600 detector". In: *Nucl. Instrum. Meth. A* 527 (2004), pp. 329–410. DOI: 10.1016/j.nima.2004.02.044.

[9] M. Antonello et al. "A Proposal for a Three Detector Short-Baseline Neutrino Oscillation Program in the Fermilab Booster Neutrino Beam". In: (Mar. 2015). arXiv: 1503.01520 [physics.ins-det].

[10] A. Abed Abud et al. "Design, construction and operation of the ProtoDUNE-SP Liquid Argon TPC". In: *JINST* 17.01 (2022), P01005. DOI: 10.1088/1748-0221/17/01/P01005. arXiv: 2108.01902 [physics.ins-det].

[11] Babak Abi et al. "Deep Underground Neutrino Experiment (DUNE), Far Detector Technical Design Report, Volume I Introduction to DUNE". In: *JINST* 15.08 (2020), T08008. DOI: 10.1088/1748-0221/15/08/T08008. arXiv: 2002.02967 [physics.ins-det].

[12] D. Casper. "The Nuance neutrino physics simulation, and the future". In: *Nucl. Phys. B Proc. Suppl.* 112 (2002). Ed. by J. G. Morfin, M. Sakuda, and Y. Suzuki, pp. 161–170. DOI: 10.1016/S0920-5632(02)01756-5. arXiv: hep-ph/0208030.

[13] J. A. Formaggio and G. P. Zeller. "From eV to EeV: Neutrino Cross Sections Across Energy Scales". In: *Rev. Mod. Phys.* 84 (2012), pp. 1307–1341. DOI: 10.1103/RevModPhys.84.1307. arXiv: 1305.7513 [hep-ex].

[14] Tomasz Golan. "Modeling nuclear effects in NuWro Monte Carlo neutrino event generator". PhD thesis. U. of Wroclaw, 2014.

[15] Antonio Riotto. "Theories of baryogenesis". In: *ICTP Summer School in High-Energy Physics and Cosmology*. July 1998, pp. 326–436. arXiv: hep-ph/9807454.

[16] Ivan Esteban et al. "The fate of hints: updated global analysis of three-flavor neutrino oscillations". In: *JHEP* 09 (2020), p. 178. DOI: 10.1007/JHEP09(2020)178. arXiv: 2007.14792 [hep-ph].

[17] K. Abe et al. "The T2K Experiment". In: *Nucl. Instrum. Meth. A* 659 (2011), pp. 106–135. DOI: 10.1016/j.nima.2011.06.067. arXiv: 1106.1238 [physics.ins-det].

[18] D. S. Ayres et al. "NOvA: Proposal to Build a 30 Kiloton Off-Axis Detector to Study $\nu_\mu \to \nu_e$ Oscillations in the NuMI Beamline". In: (Mar. 2004). arXiv: hep-ex/0503053.

[19] K. H. Ackermann et al. "The GERDA experiment for the search of $0\nu\beta\beta$ decay in $^{76}$Ge". In: *Eur. Phys. J. C* 73.3 (2013), p. 2330. DOI: 10.1140/epjc/s10052-013-2330-0. arXiv: 1212.4067 [physics.ins-det].

[20] M. Auger et al. "Search for Neutrinoless Double-Beta Decay in $^{136}$Xe with EXO-200". In: *Phys. Rev. Lett.* 109 (2012), p. 032505. DOI: 10.1103/PhysRevLett.109.032505. arXiv: 1205.5608 [hep-ex].

[21] P. Finnerty et al. "The MAJORANA DEMONSTRATOR: Progress towards showing the feasibility of a tonne–scale $^{76}Ge$ neutrinoless double–beta decay experiment". In: *J. Phys. Conf. Ser.* 485 (2014). Ed. by Myriam Mondragón et al., p. 012042. DOI: 10.1088/1742-6596/485/1/012042. arXiv: 1210.2678 [nucl-ex].

[22] C. Arnaboldi et al. "CUORE: A Cryogenic underground observatory for rare events". In: *Nucl. Instrum. Meth. A* 518 (2004), pp. 775–798. DOI: 10.1016/j.nima.2003.07.067. arXiv: hep-ex/0212053.

[23] V. Albanese et al. "The SNO+ experiment". In: *JINST* 16.08 (2021), P08059. DOI: 10.1088/1748-0221/16/08/P08059. arXiv: 2104.11687 [physics.ins-det].

[24] A. A. Aguilar-Arevalo et al. "A Search for Electron Neutrino Appearance at the $\Delta m^2 \sim 1eV^2$ Scale". In: *Phys. Rev. Lett.* 98 (2007), p. 231801. DOI: 10.1103/PhysRevLett.98.231801. arXiv: 0704.1500 [hep-ex].

[25] P. Abratenko et al. "First constraints on light sterile neutrino oscillations from combined appearance and disappearance searches with the MicroBooNE detector". In: (Oct. 2022). arXiv: 2210.10216 [hep-ex].

[26] A. Rodriguez et al. "Measurement of single charged pion production in the charged-current interactions of neutrinos in a 1.3-GeV wide band beam". In: *Phys. Rev. D* 78 (2008), p. 032003. DOI: 10.1103/PhysRevD.78.032003. arXiv: 0805.0186 [hep-ex].

[27] A. A. Aguilar-Arevalo et al. "Measurement of the $\nu_\mu$ charged current $\pi^+$ to quasi-elastic cross section ratio on mineral oil in a 0.8-GeV neutrino beam". In: *Phys. Rev. Lett.* 103 (2009), p. 081801. DOI: 10.1103/PhysRevLett.103.081801. arXiv: 0904.3159 [hep-ex].

[28] A. A. Aguilar-Arevalo et al. "Measurement of Neutrino-Induced Charged-Current Charged Pion Production Cross Sections on Mineral Oil at $E_\nu \sim$ 1 GeV". In: *Phys. Rev. D* 83 (2011), p. 052007. DOI: 10.1103/PhysRevD.83.052007. arXiv: 1011.3572 [hep-ex].

[29] B. Eberly et al. "Charged Pion Production in $\nu_\mu$ Interactions on Hydrocarbon at $\langle E_\nu \rangle = 4.0$ GeV". In: *Phys. Rev. D* 92.9 (2015), p. 092008. DOI: 10.1103/PhysRevD.92.092008. arXiv: 1406.6415 [hep-ex].

[30] C. L. McGivern et al. "Cross sections for $\nu_\mu$ and $\bar{\nu}_\mu$ induced pion production on hydrocarbon in the few-GeV region using MINERvA". In: *Phys. Rev. D* 94.5 (2016), p. 052005. DOI: 10.1103/PhysRevD.94.052005. arXiv: 1606.07127 [hep-ex].

[31] T. Le et al. "Measurement of $\bar{\nu}_\mu$ Charged-Current Single $\pi^-$ Production on Hydrocarbon in the Few-GeV Region using MINERvA". In: *Phys. Rev. D* 100.5 (2019), p. 052008. DOI: 10.1103/PhysRevD.100.052008. arXiv: 1906.08300 [hep-ex].

[32] K. Abe et al. "First measurement of the muon neutrino charged current single pion production cross section on water with the T2K near detector". In: *Phys. Rev. D* 95.1 (2017), p. 012010. DOI: 10.1103/PhysRevD.95.012010. arXiv: 1605.07964 [hep-ex].

[33] K. Abe et al. "Measurement of the muon neutrino charged-current single $\pi^+$ production on hydrocarbon using the T2K off-axis near detector ND280". In: *Phys. Rev. D* 101.1 (2020), p. 012007. DOI: 10.1103/PhysRevD.101.012007. arXiv: 1909.03936 [hep-ex].

[34] R. Acciarri et al. "First measurement of the cross section for $\nu_\mu$ and $\bar{\nu}_\mu$ induced single charged pion production on argon using ArgoNeuT". In: *Phys. Rev. D* 98.5 (2018), p. 052002. DOI: 10.1103/PhysRevD.98.052002. arXiv: 1804.10294 [hep-ex].

[35] G. M. Radecky et al. "Study of Single Pion Production by Weak Charged Currents in Low-energy Neutrino *d* Interactions". In: *Phys. Rev. D* 25 (1982). [Erratum: Phys.Rev.D 26, 3297 (1982)], pp. 1161–1173. DOI: 10.1103/PhysRevD.25.1161.

[36] T. Kitagaki et al. "Charged Current Exclusive Pion Production in Neutrino Deuterium Interactions". In: *Phys. Rev. D* 34 (1986), pp. 2554–2565. DOI: 10.1103/PhysRevD.34.2554.

[37] L. Aliaga et al. "Neutrino Flux Predictions for the NuMI Beam". In: *Phys. Rev. D* 94.9 (2016). [Addendum: Phys.Rev.D 95, 039903 (2017)], p. 092005. DOI: 10.1103/PhysRevD.94.092005. arXiv: 1607.00704 [hep-ex].

[38] MINERvA collaboration. *Pion data release page*. 2017. URL: https://minerva.fnal.gov/pion-data-release-page/.

[39] M. Betancourt et al. "Comparisons and Challenges of Modern Neutrino Scattering Experiments (TENSIONS2016 Report)". In: *Phys. Rept.* 773-774 (2018), pp. 1–28. DOI: 10.1016/j.physrep.2018.08.003. arXiv: 1805.07378 [hep-ex].

[40] Yoshinari Hayato and Luke Pickering. "The NEUT neutrino interaction simulation program library". In: *Eur. Phys. J. ST* 230.24 (2021), pp. 4469–4481. DOI: 10.1140/epjs/s11734-021-00287-7. arXiv: 2106.15809 [hep-ph].

[41] K. Gallmeister, U. Mosel, and J. Weil. "Neutrino-Induced Reactions on Nuclei". In: *Phys. Rev. C* 94.3 (2016), p. 035502. DOI: 10.1103/PhysRevC.94.035502. arXiv: 1605.09391 [nucl-th].

[42] Tomasz Golan, Cezary Juszczak, and Jan T. Sobczyk. "Final State Interactions Effects in Neutrino-Nucleus Interactions". In: *Phys. Rev. C* 86 (2012), p. 015505. DOI: 10.1103/PhysRevC.86.015505. arXiv: 1202.4197 [nucl-th].

[43] M. Buizza Avanzini et al. "Comparisons and challenges of modern neutrino-scattering experiments". In: *Phys. Rev. D* 105.9 (2022), p. 092004. DOI: 10.1103/PhysRevD.105.092004. arXiv: 2112.09194 [hep-ex].

[44] R. Acciarri et al. "Design and Construction of the MicroBooNE Detector". In: *JINST* 12.02 (2017), P02017. DOI: 10.1088/1748-0221/12/02/P02017. arXiv: 1612.05824 [physics.ins-det].

[45] Teppei Katori. "The MicroBooNE light collection system". In: *JINST* 8 (2013). Ed. by Stanley Seibert, p. C10011. DOI: 10.1088/1748-0221/8/10/C10011. arXiv: 1307.5256 [physics.ins-det].

[46] *Fermilab's Accelerator Complex*. 2020. URL: https://www.fnal.gov/pub/science/particle-accelerators/accelerator-complex.html.

[47] A. A. Aguilar-Arevalo et al. "The Neutrino Flux prediction at MiniBooNE". In: *Phys. Rev. D* 79 (2009), p. 072002. DOI: 10.1103/PhysRevD.79.072002. arXiv: 0806.1449 [hep-ex].

[48] S. Agostinelli et al. "Geant4—a simulation toolkit". In: *Nuclear Instruments and Methods in Physics Research Section A: Accelerators, Spectrometers, Detectors and Associated Equipment* 506.3 (2003), pp. 250–303. ISSN: 0168-9002. DOI: https://doi.org/10.1016/S0168-9002(03)01368-8. URL: https://www.sciencedirect.com/science/article/pii/S0168900203013688.

[49] David W. Schmitz. "A Measurement of Hadron Production Cross Sections for the Simulation of Accelerator Neutrino Beams and a Search for $\nu_\mu$ to $\nu_e$ Sscillations in the $\delta m^2$ about equals $1 - eV^2$ Region". PhD thesis. Columbia U., 2008. DOI: 10.2172/935240.

[50] The MicroBooNE Collaboration. *Booster Neutrino Flux Prediction at MicroBooNE*. Tech. rep. MICROBOONE-NOTE-1031-PUB. MicroBooNE, 2018. URL: https://microboone.fnal.gov/public-notes/.

[51] D. Heck et al. "CORSIKA: A Monte Carlo code to simulate extensive air showers". In: (Feb. 1998).

[52] C. Andreopoulos et al. "The GENIE neutrino Monte Carlo generator". In: *Nuclear Instruments and Methods in Physics Research Section A: Accelerators, Spectrometers, Detectors and Associated Equipment* 614.1 (2010), pp. 87–104. ISSN: 0168-9002. DOI: https://doi.org/10.1016/j.nima.2009.12.009. URL: https://www.sciencedirect.com/science/article/pii/S0168900209023043.

[53] C. Andreopoulos et al. "The GENIE Neutrino Monte Carlo Generator: Physics and User Manual". In: (2015). arXiv: 1510.05494 [hep-ph].

[54] A. Bodek and J. L. Ritchie. "Further Studies of Fermi Motion Effects in Lepton Scattering from Nuclear Targets". In: *Phys. Rev. D* 24 (1981), p. 1400. DOI: 10.1103/PhysRevD.24.1400.

[55] J. Nieves et al. "Inclusive charged-current neutrino-nucleus reactions". In: *Phys. Rev. C* 83 (4 Apr. 2011), p. 045501. DOI: 10.1103/PhysRevC.83.045501. URL: https://link.aps.org/doi/10.1103/PhysRevC.83.045501.

[56] R. Gran et al. "Neutrino-nucleus quasi-elastic and 2p2h interactions up to 10 GeV". In: *Phys. Rev. D* 88 (11 Dec. 2013), p. 113007. DOI: 10.1103/PhysRevD.88.113007. URL: https://link.aps.org/doi/10.1103/PhysRevD.88.113007.

[57] C.H. Llewellyn Smith. "Neutrino reactions at accelerator energies". In: *Physics Reports* 3.5 (1972), pp. 261–379. ISSN: 0370-1573. DOI: https://doi.org/10.1016/0370-1573(72)90010-5. URL: https://www.sciencedirect.com/science/article/pii/0370157372900105.

[58] Teppei Katori. "Meson exchange current (MEC) models in neutrino interaction generators". In: *AIP Conference Proceedings* 1663.1 (2015), p. 030001. DOI: 10.1063/1.4919465. eprint: https://aip.scitation.org/doi/pdf/10.1063/1.4919465. URL: https://aip.scitation.org/doi/abs/10.1063/1.4919465.

[59] Dieter Rein and Lalit M. Sehgal. "Neutrino Excitation of Baryon Resonances and Single Pion Production". In: *Annals Phys.* 133 (1981), pp. 79–153. DOI: 10.1016/0003-4916(81)90242-6.

[60] Jaroslaw A. Nowak. "Four Momentum Transfer Discrepancy in the Charged Current $\pi^+$ Production in the MiniBooNE: Data vs. Theory". In: *AIP Conf. Proc.* 1189.1 (2009). Ed. by Federico Sanchez, M. Sorel, and Luis Alvarez-Ruso, pp. 243–248. DOI: 10.1063/1.3274164. arXiv: 0909.3659 [hep-ph].

[61] Konstantin S. Kuzmin, Vladimir V. Lyubushkin, and Vadim A. Naumov. "Lepton polarization in neutrino nucleon interactions". In: *Mod. Phys. Lett. A* 19 (2004). Ed. by A. V. Efremov and O. V. Teryaev, pp. 2815–2829. DOI: 10.1142/S0217732304016172. arXiv: hep-ph/0312107.

[62] Ch. Berger and L. M. Sehgal. "Lepton mass effects in single pion production by neutrinos". In: *Phys. Rev. D* 76 (2007), p. 113004. DOI: 10.1103/PhysRevD.76.113004. arXiv: 0709.4378 [hep-ph].

[63] Krzysztof M. Graczyk and Jan T. Sobczyk. "Form Factors in the Quark Resonance Model". In: *Phys. Rev. D* 77 (2008). [Erratum: Phys.Rev.D 79, 079903 (2009)], p. 053001. DOI: 10.1103/PhysRevD.79.079903. arXiv: 0707.3561 [hep-ph].

[64] N. Metropolis et al. "Monte Carlo Calculations on Intranuclear Cascades. I. Low-Energy Studies". In: *Phys. Rev.* 110.1 (1958), p. 185. DOI: 10.1103/PhysRev.110.185.

[65] The MicroBooNE Collaboration. *Study of Space Charge Effects in MicroBooNE*. Tech. rep. MICROBOONE-NOTE-1018-PUB. MicroBooNE, 2016. URL: https://microboone.fnal.gov/public-notes/.

[66] P. Abratenko et al. "Measurement of space charge effects in the MicroBooNE LArTPC using cosmic muons". In: *JINST* 15.12 (2020), P12037. DOI: 10.1088/1748-0221/15/12/P12037. arXiv: 2008.09765 [physics.ins-det].

[67] C. Adams et al. "Ionization electron signal processing in single phase LArTPCs. Part I. Algorithm Description and quantitative evaluation with MicroBooNE simulation". In: *JINST* 13.07 (2018), P07006. DOI: 10.1088/1748-0221/13/07/P07006. arXiv: 1802.08709 [physics.ins-det].

[68] C. Adams et al. "Ionization electron signal processing in single phase LArTPCs. Part II. Data/simulation comparison and performance in MicroBooNE". In: *JINST* 13.07 (2018), P07007. DOI: 10.1088/1748-0221/13/07/P07007. arXiv: 1804.02583 [physics.ins-det].

[69] R. Acciarri et al. "Noise Characterization and Filtering in the MicroBooNE Liquid Argon TPC". In: *JINST* 12.08 (2017), P08003. DOI: 10.1088/1748-0221/12/08/P08003. arXiv: 1705.07341 [physics.ins-det].

[70] Bruce Baller. "Liquid argon TPC signal formation, signal processing and reconstruction techniques". In: *JINST* 12.07 (2017), P07010. DOI: 10.1088/1748-0221/12/07/P07010. arXiv: 1703.04024 [physics.ins-det].

[71] J. S. Marshall and M. A. Thomson. "The Pandora Software Development Kit for Pattern Recognition". In: *Eur. Phys. J. C* 75.9 (2015), p. 439. DOI: 10.1140/epjc/s10052-015-3659-3. arXiv: 1506.05348 [physics.data-an].

[72] R. Acciarri et al. "The Pandora multi-algorithm approach to automated pattern recognition of cosmic-ray muon and neutrino events in the MicroBooNE detector". In: *Eur. Phys. J. C* 78.1 (2018), p. 82. DOI: 10.1140/epjc/s10052-017-5481-6. arXiv: 1708.03135 [hep-ex].

[73] The MicroBooNE Collaboration. *A Comparison of Monte-Carlo Simulations and Data from MicroBooNE*. Tech. rep. MICROBOONE-NOTE-1014-PUB. MicroBooNE, 2016. URL: https://microboone.fnal.gov/public-notes/.

[74] The MicroBooNE Collaboration. *Selection and kinematic properties of numu charged-current inclusive events in 5E19 POT of MicroBooNE data*. Tech. rep. MICROBOONE-NOTE-1010-PUB. MicroBooNE, 2016. URL: https://microboone.fnal.gov/public-notes/.

[75] A. Devitt and A. Lister. "Measurements of muon neutrino charged-current interactions by the MicroBooNE experiment". In: *J. Phys. Conf. Ser.* 888.1 (2017), p. 012141. DOI: 10.1088/1742-6596/888/1/012141.

[76] Marco Del Tutto. "First Measurements of Inclusive Muon Neutrino Charged Current Differential Cross Sections on Argon at 0.8 GeV Average Neutrino Energy with the MicroBooNE Detector". PhD thesis. Oxford U., 2019. DOI: 10.2172/1515054.

[77] Particle Data Group. *Muons in argon liquid (Ar)*. 2022. URL: https://pdg.lbl.gov/2022/AtomicNuclearProperties/MUE/muE_argon_liquid.pdf.

[78] Virgil L. Highland. "Some practical remarks on multiple scattering". In: *Nuclear Instruments and Methods* 129.2 (1975), pp. 497–499. ISSN: 0029-554X. DOI: https://doi.org/10.1016/0029-554X(75)90743-0. URL: https://www.sciencedirect.com/science/article/pii/0029554X75907430.

[79] Gerald R. Lynch and Orin I. Dahl. "Approximations to multiple Coulomb scattering". In: *Nuclear Instruments and Methods in Physics Research Section B: Beam Interactions with Materials and Atoms* 58.1 (1991), pp. 6–10. ISSN: 0168-583X. DOI: https://doi.org/10.1016/0168-583X(91)95671-Y. URL: https://www.sciencedirect.com/science/article/pii/0168583X9195671Y.

[80] P. Abratenko et al. "Determination of muon momentum in the MicroBooNE LArTPC using an improved model of multiple Coulomb scattering". In: *JINST* 12.10 (2017), P10010. DOI: 10.1088/1748-0221/12/10/P10010. arXiv: 1703.06187 [physics.ins-det].

[81] P. Abratenko et al. "First Measurement of Inclusive Muon Neutrino Charged Current Differential Cross Sections on Argon at $E_\nu$ ∼0.8 GeV with the MicroBooNE Detector". In: *Phys. Rev. Lett.* 123.13 (2019), p. 131801. DOI: 10.1103/PhysRevLett.123.131801. arXiv: 1905.09694 [hep-ex].

[82] Kirsty Duffy and Adam Lister. *Particle Identification in the MicroBooNE Time Projection Chamber*. Tech. rep. MicroBooNE, 2018.

[83] P. Abratenko et al. "Determination of muon momentum in the MicroBooNE LArTPC using an improved model of multiple Coulomb scattering". In: *Journal of Instrumentation* 12.10 (2017), P10010–P10010. DOI: 10.1088/1748-0221/12/10/p10010. URL: https://doi.org/10.1088%5C%2F1748-0221%5C%2F12%5C%2F10%5C%2Fp10010.

[84] Yichen Li et al. "Measurement of Longitudinal Electron Diffusion in Liquid Argon". In: *Nucl. Instrum. Meth. A* 816 (2016), pp. 160–170. DOI: 10.1016/j.nima.2016.01.094. arXiv: 1508.07059 [physics.ins-det].

[85] Eido Shibamura et al. "Ratio of diffusion coefficient to mobility for electrons in liquid argon". In: *Phys. Rev. A* 20.6 (1979), p. 2547. DOI: 10.1103/PhysRevA.20.2547.

[86] S. DeRenzo. *Electron diffusion and positive ion charge retention in liquid-filled high-resolution multistrip ionization-mode chambers*. Tech. rep. Physics Note No. 786. Lawrence Berkeley Laboratory, Group A, 1974.

[87] C. Adams et al. "Rejecting cosmic background for exclusive charged current quasi elastic neutrino interaction studies with Liquid Argon TPCs; a case study with the MicroBooNE detector". In: *Eur. Phys. J. C* 79.8 (2019), p. 673. DOI: 10.1140/epjc/s10052-019-7184-7. arXiv: 1812.05679 [physics.ins-det].

[88] Afroditi Papadopoulou. *Exclusive Quasielastic-like Muon Neutrino Argon Interactions in MicroBooNE and Connections with Electron Scattering*. Oct. 30, 2020. URL: https://microboone.fnal.gov/talks-and-posters/.